



NAVAL POSTGRADUATE SCHOOL

MONTEREY, CALIFORNIA

THESIS

**THE RELATIVE FREQUENCY OF ROSSBY WAVE
TRAIN TRIGGERING MECHANISMS ASSOCIATED
WITH DOWNSTREAM DEVELOPMENT OVER EUROPE**

by

Colin L. Thornton

June 2014

Thesis Advisor:
Second Reader:

Richard W. Moore
Patrick A. Harr

Approved for public release; distribution is unlimited

THIS PAGE INTENTIONALLY LEFT BLANK

REPORT DOCUMENTATION PAGE			<i>Form Approved OMB No. 0704-0188</i>	
Public reporting burden for this collection of information is estimated to average 1 hour per response, including the time for reviewing instruction, searching existing data sources, gathering and maintaining the data needed, and completing and reviewing the collection of information. Send comments regarding this burden estimate or any other aspect of this collection of information, including suggestions for reducing this burden, to Washington headquarters Services, Directorate for Information Operations and Reports, 1215 Jefferson Davis Highway, Suite 1204, Arlington, VA 22202-4302, and to the Office of Management and Budget, Paperwork Reduction Project (0704-0188) Washington DC 20503.				
1. AGENCY USE ONLY (Leave blank)		2. REPORT DATE June 2014	3. REPORT TYPE AND DATES COVERED Master's Thesis	
4. TITLE AND SUBTITLE THE RELATIVE FREQUENCY OF ROSSBY WAVE TRAIN TRIGGERING MECHANISMS ASSOCIATED WITH DOWNSTREAM DEVELOPMENT OVER EUROPE			5. FUNDING NUMBERS	
6. AUTHOR(S) Thornton, Colin L.				
7. PERFORMING ORGANIZATION NAME(S) AND ADDRESS(ES) Naval Postgraduate School Monterey, CA 93943-5000			8. PERFORMING ORGANIZATION REPORT NUMBER	
9. SPONSORING /MONITORING AGENCY NAME(S) AND ADDRESS(ES) N/A			10. SPONSORING/MONITORING AGENCY REPORT NUMBER	
11. SUPPLEMENTARY NOTES The views expressed in this thesis are those of the author and do not reflect the official policy or position of the Department of Defense or the U.S. Government. IRB Protocol number ____N/A____.				
12a. DISTRIBUTION / AVAILABILITY STATEMENT Approved for public release; distribution is unlimited			12b. DISTRIBUTION CODE	
13. ABSTRACT (maximum 200 words) Rossby wave trains (RWTs) are coherent envelopes of baroclinic waves that propagate on the midlatitude waveguide and are capable of producing downstream development. The waveguide is a region of heightened potential vorticity gradient along steeply sloping isentropic surfaces defining the mid-latitude jet stream. The goal of this research is to examine a climatology of objectively identified RWTs that result in downstream development over Europe, and to develop a methodology to subjectively determine the atmospheric phenomena responsible for triggering each. The purpose is to provide insight into the relative frequency of occurrence of RWTs triggered by each of four atmospheric disturbances over the North Atlantic to support future research into improving the predictability of waveguide perturbations and subsequent downstream development. A subset of RWTs is analyzed using dynamic tropopause, upper-level divergent outflow, sea level pressure, and Hovmöller plots. The RWT triggering mechanisms are identified and, when applicable, compared to known occurrences in climatology. Twenty-seven are (71%) are triggered by warm conveyor belts associated with extratropical cyclones, three (8%) by tropopause polar vortices, two (5%) by the extratropical transition of tropical cyclones, and six (16%) by diabatic Rossby vortices.				
14. SUBJECT TERMS Rossby wave train, downstream development, tropopause polar vortex, warm conveyor belt, diabatic Rossby vortex, extratropical cyclone, climatology			15. NUMBER OF PAGES 139	
			16. PRICE CODE	
17. SECURITY CLASSIFICATION OF REPORT Unclassified	18. SECURITY CLASSIFICATION OF THIS PAGE Unclassified	19. SECURITY CLASSIFICATION OF ABSTRACT Unclassified	20. LIMITATION OF ABSTRACT UU	

THIS PAGE INTENTIONALLY LEFT BLANK

Approved for public release; distribution is unlimited

**THE RELATIVE FREQUENCY OF ROSSBY WAVE TRAIN TRIGGERING
MECHANISMS ASSOCIATED WITH DOWNSTREAM DEVELOPMENT OVER
EUROPE**

Colin L. Thornton
Lieutenant, United States Navy
B.S., United States Naval Academy, 2004

Submitted in partial fulfillment of the
requirements for the degree of

**MASTER OF SCIENCE IN METEOROLOGY AND PHYSICAL
OCEANOGRAPHY**

from the

**NAVAL POSTGRADUATE SCHOOL
June 2014**

Author: Colin L. Thornton

Approved by: Richard W. Moore
Thesis Advisor

Patrick A. Harr
Second Reader

Wendell A. Nuss
Chair, Department of Meteorology

THIS PAGE INTENTIONALLY LEFT BLANK

ABSTRACT

Rossby wave trains (RWTs) are coherent envelopes of baroclinic waves that propagate on the midlatitude waveguide and are capable of producing downstream development. The waveguide is a region of heightened potential vorticity gradient along steeply sloping isentropic surfaces defining the mid-latitude jet stream.

The goal of this research is to examine a climatology of objectively identified RWTs that result in downstream development over Europe, and to develop a methodology to subjectively determine the atmospheric phenomena responsible for triggering each. The purpose is to provide insight into the relative frequency of occurrence of RWTs triggered by each of four atmospheric disturbances over the North Atlantic to support future research into improving the predictability of waveguide perturbations and subsequent downstream development.

A subset of RWTs is analyzed using dynamic tropopause, upper-level divergent outflow, sea level pressure, and Hovmöller plots. The RWT triggering mechanisms are identified and, when applicable, compared to known occurrences in climatology. Twenty-seven are (71%) are triggered by warm conveyor belts associated with extratropical cyclones, three (8%) by tropopause polar vortices, two (5%) by the extratropical transition of tropical cyclones, and six (16%) by diabatic Rossby vortices.

THIS PAGE INTENTIONALLY LEFT BLANK

TABLE OF CONTENTS

I.	INTRODUCTION.....	1
A.	DEFINITION OF A ROSSBY WAVE TRAIN.....	1
B.	ROSSBY WAVE TRAIN TRIGGERING MECHANISMS.....	3
1.	Tropopause Polar Vortex.....	5
2.	Warm Conveyor Belt.....	9
3.	Diabatic Rossby Vortex.....	12
4.	Extratropical Transition of a Tropical Cyclone.....	17
C.	MOTIVATION FOR STUDY	21
II.	DATA AND METHODOLOGY	25
A.	ROSSBY WAVE TRAIN CLIMATOLOGY.....	25
B.	DIABATIC ROSSBY VORTEX CLIMATOLOGY	29
C.	METHOD OF SUBJECTIVE ROSSBY WAVE TRAIN ANALYSIS	30
1.	Defining a Subset for Analysis.....	30
2.	Subjective Analysis Methodology.....	32
a.	<i>Tropopause Polar Vortex.....</i>	<i>36</i>
b.	<i>Warm Conveyor Belt.....</i>	<i>41</i>
c.	<i>Diabatic Rossby Vortex.....</i>	<i>46</i>
d.	<i>Extratropical Transition</i>	<i>49</i>
III.	CLIMATOLOGICAL ANALYSIS.....	55
A.	ERA-40 ROSSBY WAVE TRAIN CLIMATOLOGY	55
1.	Frequency Distribution and Lifetime Correlation.....	55
2.	Longitudinal Distribution	57
B.	ERA-INTERIM ROSSBY WAVE TRAIN CLIMATOLOGY	61
1.	Longitudinal Distribution	61
IV.	DETAIL OF ROSSBY WAVE TRAIN LIFE CYCLES.....	65
A.	TROPOPAUSE POLAR VORTEX	65
1.	Triggering Phase	65
2.	Propagation Phase and Downstream Development.....	66
3.	Termination Phase	70
4.	Sensible Weather Impacts.....	72
B.	WARM CONVEYOR BELT	75
1.	Triggering Phase	75
2.	Propagation Phase and Downstream Development.....	77
3.	Termination Phase	79
4.	Sensible Weather Impacts.....	81
C.	DIABATIC ROSSBY VORTEX	84
1.	Triggering Phase	84
2.	Propagation Phase and Downstream Development.....	85
3.	Termination Phase	89
4.	Sensible Weather Impacts.....	91
D.	EXTRATROPICAL TRANSITION	94

1.	Triggering Phase	94
2.	Propagation Phase and Downstream Development.....	95
3.	Termination Phase	97
4.	Sensible Weather Impacts.....	99
V.	STATISTICS OF ROSSBY WAVE TRAIN TRIGGERS	103
A.	TOTAL NUMBERS OF ROSSBY WAVE TRAIN TRIGGERS	103
B.	LONGITUDINAL VARIATIONS AND FREQUENCY OF ROSSBY WAVE TRAIN TRIGGERS	104
VI.	SUMMARY AND CONCLUSIONS	109
	LIST OF REFERENCES	111
	INITIAL DISTRIBUTION LIST	115

LIST OF FIGURES

Figure 1.	Instantaneous isentropic PV gradient on 1800 UTC 24 Dec 1999 (shaded, units 10^{-6} PVU m^{-1}). (a) On the 320-K isentrope, 2-PVU PV contour and wind speed (contours 50, 70, 80, 90 $m\ s^{-1}$) overlaid. (b) South-north cross section at $30^{\circ}W$. Vertical coordinate: θ ; PV isolines [1,2 (bold) 3, 4, 5, 6, 8 PVU]; and 50, 70, 80, 90 $m\ s^{-1}$ isotachs (dashed) overlaid (from Schwierz et al. 2004).	1
Figure 2.	Schematic of the net diabatic PV (shaded) relative to large-amplitude waves on the tropopause (solid line). Positive diabatic PV is shaded lightly and marked with a “+”. Negative diabatic PV is shaded darkly and marked with a “-”. Troughs and ridges are marked sequentially beginning with a “T” and “R”, respectively (after Chagnon, Gray, and Methven 2013).	2
Figure 3.	Schematic vertical cross-sections showing diabatically produced PV anomalies (hatched regions with a plus or minus sign) for the idealized cases of (a) “impulsive diabatic heating”, and (b) “steady condensation” in a frontal zone. Shading indicates the regions of diabatic heating. In (a) the solid lines are isentropes and in (b) the bold lines with arrows refer to air-parcel trajectories. $D\theta$ and DP denote material tendencies of potential temperature and potential vorticity, respectively (from Wernli and Davies 1997).	4
Figure 4.	Time-height sections from a Weather Research and Forecasting (WRF) simulation during 0000 UTC 5 Nov 2005–0000 UTC 10 Nov 2005 of the Ertel PV (EPV) tendency (PVU h^{-1}) due to (a) all diabatic processes, (b) radiation (colors) and cloud water (sum of liquid and ice mixing ratios; contours every 0.004 $g\ kg^{-1}$), (c) latent heating, and (d) the sum of the planetary boundary layer scheme, cumulus scheme, and frictional processes. All fields are averaged within the area encompassed by the 285 K closed tropopause potential temperature contour. The thick black line represents the 2 PVU surface. Labels on the abscissa are days from the start of the simulation. The EPV tendency color interval is 0.0025 PVU h^{-1} (from Cavallo and Hakim 2009).	6
Figure 5.	(a) PV on the 320-K isentrope at 0600 UTC 20 Dec 2000, taken from the ERA-40 dataset. Numerous mesoscale PV structures (see $PV > 7$ PVU) characterize the distribution. Labels S1 and S2 show locations of streamers. Anomalies J1 and J2 are situated alongside the jet. The dynamical tropopause (red shading) is coincident with the jet and separates the stratospheric portion that encompasses the Pole from the surrounding tropospheric portion of the isentropic surface. (b) Vertical distribution of PV (color) and potential temperature (dashed contours) at $150^{\circ}E$. The limits of the meridional cross section are marked by solid black circles in (a). The dynamical tropopause is outlined in thick black. Thin solid contours show positive values of the vertical component of relative vorticity (interval $2.5 \times 10^{-5}\ s^{-1}$) (from Kew et al. 2010).	8

Figure 6.	Winter climatology of PV anomalies identified on 320 K: (a) event density and (b) track density. Densities show 10-yr winter-season totals over circular areas 5° radius centered on each grid point. A minimum lifetime threshold of 1 day is applied. Amplitudes of the included structures attain at least 1 PVU within a lifetime. The mean dynamical tropopause is overlaid (thick black line) (from Kew et al. 2010).	9
Figure 7.	Six-day trajectories starting 1200 UTC 23 Jan 1987, of which the first 2 days were identified as a WCB. (a) The forward trajectories (gray) and 3-day backward trajectories (black) from the starting locations of the forward trajectories. Positions along the forward trajectories are marked every 24 h. Sea level pressure (light gray) contour lines are drawn every 10 hPa for the trajectory starting time (1200 UTC 23 Jan 1987). For clarity, only those WCB trajectories associated with the cyclone over the eastern seaboard of North America are drawn. (b) Vertical projection of the trajectories shown in (a) (from Eckhardt et al. 2004).	10
Figure 8.	Climatological frequency of WCB trajectories in DJF at $t = 0$ h (WCB starting points). Colors represent the relative frequency (in percent) of WCB trajectories at each grid point. The black contour represents a WCB frequency of 1% at $t = 0$ h (after Madonna et al. 2014).	12
Figure 9.	Sea level pressure (contours; hPa) and previous 6-h accumulated precipitation (shading; mm) from ECMWF analysis data beginning (a) 1200 UTC 24 Feb 2006 and every six hours after (b)–(f). Heavy black lines in (b) – (f) represent the location of cross-sections in Figure 10 (after Moore et al. 2008).	14
Figure 10.	Vertical cross-section analysis of PV (shading; PVU; white contour represents the 1.5 PVU surface) and potential temperature (black contours; K) from ECMWF analysis data at (a) 1800 UTC 24 Feb 2006 and every 6 hours after (b)–(e). One grid point on the x axis is roughly equivalent to 50 km, and the white region on the lower boundary represents orography (from Moore et al. 2008).	15
Figure 11.	Monthly number of DRWs [DRVs] during the years 2001–10 in the (a) North Atlantic and (b) North Pacific (from BW13).	16
Figure 12.	Monthly number of “cyclone bombs” (gray bars) during the years 2001–10 in the (a) North Atlantic and (b) North Pacific. Bombs with a DRW [DRV] precursor are indicated by dark gray shading (from BW13).	17
Figure 13.	Tracks of all tropical cyclones that underwent extratropical transition during 1970–99. (a) Western North Pacific. Tracks of tropical cyclones defined to be extratropical in JTWC best-track data. (b) Southwest Pacific [data as in (a)] and southeast Indian Ocean [tracks of tropical cyclones that accelerated toward the southeast under the influence of a midlatitude frontal system and maintained gales into midlatitudes, the so-called captured cyclones in Foley and Hanstrum (1994); best-track data taken from http://www.australiasevereweather.com/cyclones/history.htm]. (c) North Atlantic. Tracks of tropical cyclones defined to be extratropical in National Hurricane Center best-track data (from Jones et al. 2003).	18

Figure 14.	Schematic of the evolution of ET in the western North Pacific based on 30 cases that occurred from 1 Jun through 31 Oct during 1994–98. The times on the abscissa are subsequent to the beginning of the transformation stage. Means \pm standard deviation of SLP are listed for each step of transformation, and for the conclusion of the reintensification stage, with the number of cases observed in each of the three outcomes of reintensification depicted parenthetically (from Klein et al. 2000).	19
Figure 15.	Schematic representation of ridge amplification and jet streak intensification associated with the divergent outflow of a TC impinging upon an upper-tropospheric jet stream/waveguide. Vectors represent the upper-tropospheric irrotational wind (i.e., divergent outflow) associated with the TC. Shading denotes negative PV advection by the irrotational wind (from Archambault et al. 2013).	20
Figure 16.	Monthly total number of tropical cyclones (open bars) in each basin during 1970–99 and the number of tropical cyclones that underwent extratropical transition (shaded bars). Data as in Figure 13 (after Jones et al. 2003).	21
Figure 17.	Schematic of a potential experiment designed to study RWT triggering mechanisms and their interactions with the waveguide. The light blue arrow represents ET and WCBs associated with ETs. The red arrow represents WCBs associated with extratropical cyclones. The green arrow represents TPVs approaching the poleward side of the waveguide (unpublished figure provided by P. Harr).	22
Figure 18.	RWT analysis on the 250 hPa pressure level for 0000 UTC 7 Aug 2002. (a) Meridional wind v [$\pm 10, \pm 20, \pm 30$] m s^{-1} . In the color version warm colors correspond to positive values of v and cold color contours correspond to negative values of v . The solid green line is an isoline of geopotential ($\Phi = 10^5 \text{ m}^2 \text{ s}^{-2}$). (b) Clipped envelope E with the same shading convention as in (a). (c) The field $O(\lambda)$, which is a latitudinal average of E (from Glatt and Wirth 2013).	26
Figure 19.	Dependence of various object properties on the clipping parameter τ^* (stepwidth $\Delta\tau^* = 0.05$): (a) $\Delta\lambda$ and Δt ; (b) \overline{A} , (c) sp, ep; “long” denotes the longitudinal component, “date” the temporal component (from Glatt and Wirth 2013).	27
Figure 20.	Hovmöller diagram of $O(\lambda, t)$ (shading, in m s^{-1}) on the 250 hPa surface for an episode in summer 2002. The straight green line indicates the main inertial axis (after GW13).	28
Figure 21.	Potential temperature (K) and wind barbs (long barb = 10 kts and a flag = 50 kts) on the dynamic tropopause, which is defined as the 1.5 PVU surface. Lower-level relative vorticity averaged over the 925–850 hPa layer is indicated by black contours (every $5 \times 10^{-5} \text{ s}^{-1}$; unpublished figure provided by H. Archambault).	32
Figure 22.	The irrotational wind (IW) figure showing 300–200 hPa averaged IW with vectors (values $\geq 5 \text{ m s}^{-1}$), 250 hPa wind speeds with colored contours (m s^{-1}), 250 hPa potential vorticity with gray contours (every 1 PVU), 250	

	hPa relative humidity with gray shading (%), 600–400 hPa averaged ascent with red contours (every 5×10^{-3} hPa s^{-1} ; unpublished figure provided by H. Archambault).....	33
Figure 23.	Sea level pressure (black contour, hPa) figure where gray shading indicates total column precipitable water (mm), color shading indicates 250 hPa wind speeds ($m s^{-1}$), dashed contours are 1000–500 hPa thickness labeled every 6 dam, and solid contours are SLP every 4 hPa (unpublished figure provided by H. Archambault).....	34
Figure 24.	Hovmöller diagram of the lifecycle of RWT number 6824 using 300 hPa meridional wind anomalies from NCEP Reanalysis data averaged between 25° – 55° N. Wind speeds are indicated by color where warmer colors indicate positive values and cooler colors indicate negative values. The plot begins at 0000 UTC 16 Sep 2006 (top) and ends at 0000 UTC 25 Sep 2006 (bottom) (unpublished figure provided by the National Oceanic and Atmospheric Administration [NOAA]/Earth System Research Laboratory [ESRL] Physical Sciences Division).....	35
Figure 25.	Same as for Figure 21 except 0000 UTC for (a) 20 Oct 2010, (b) 21 Oct 2010, (c) 22 Oct 2010, (d) 23 Oct 2010, (e) 24 Oct 2010, and (f) 25 Oct 2010. The red circle marks the location of the TPV at each time (unpublished figure provided by H. Archambault).....	37
Figure 26.	Same as for Figure 21, except for 0000 UTC 23 Oct 2010 (unpublished figure provided by H. Archambault).....	38
Figure 27.	Same as for Figure 22, except for 0000 UTC 23 Oct 2010 (unpublished figure provided by H. Archambault).....	39
Figure 28.	Same as with Figure 22, except for (a) 0000 UTC 25 Oct 2010, (b) 1200 UTC 25 Oct 2010, (c) 0000 UTC 26 Oct 2010, and (d) 1200 UTC 26 Oct 2010 (unpublished figure provided by H. Archambault).....	40
Figure 29.	Same as for Figure 21, except for (a) 0000 UTC 14 Sep 2006, (b) 0000 UTC 15 Sep 2006, (c) 0000 UTC 16 Sep 2006, and (d) 0000 UTC 17 Sep 2006 (unpublished figure provided by H. Archambault).....	42
Figure 30.	Same as for Figure 21, except for (a) 1200 UTC 17 Sep 2006, (b) 0000 UTC 18 Sep 2006, (c) 1200 UTC 18 Sep 2006, and (d) 0000 UTC 19 Oct 2006 (unpublished figure provided by H. Archambault).....	43
Figure 31.	Same as for Figure 23, except for (a) 1200 UTC 15 Sep 2006 and (c) 1200 UTC 16 Sep 2006. Same as for Figure 22 at (b) 1200 UTC 15 Sep 2006 and (d) 1200 UTC 16 Sep 2006 (unpublished figure provided by H. Archambault).....	44
Figure 32.	Same as for figure 22, except for (a) 0000 UTC 17 Sep 2006, (b) 0000 UTC 18 Sep 2006, (c) 0000 UTC 19 Sep 2006, and (d) 0000 UTC 20 Sep 2006 (unpublished figure provided by H. Archambault).....	45
Figure 33.	Same as for Figure 21, except for 1200 UTC at (a) 22 Sep 2006 and (c) 23 Sep 2006. Same as for Figure 22 at (b) 22 Sep 2006 and (d) 23 Sep 2006 (unpublished figure provided by H. Archambault).....	47

Figure 34.	Same as for Figure 11, except for (a) 1200 UTC 24 Sep 2006, (b) 0000 UTC 25 Sep 2006, (c) 1200 UTC 25 Sep 2006, and (d) 0000 UTC 26 Sep 2006 (unpublished figure provided by H. Archambault).....	49
Figure 35.	Best track positions for Hurricane Igor, 8–21 September 2010. Track during the extratropical stage is based partially on analyses from NOAA Ocean Prediction Center (from Pasch and Kimberlain 2011).	50
Figure 36.	Same as for Figure 21, except for 1200 UTC 19 Sep 2010 (unpublished figure provided by H. Archambault).....	51
Figure 37.	Same as for Figure 22, except for (a) 0000 UTC 20 Sep 2010 and (b) 0600 UTC 20 Sep 2010 (unpublished figure provided by H. Archambault).	52
Figure 38.	Same as for Figure 22, except for (a) 1200 UTC 20 Sep 2010, (b) 0000 UTC 21 Sep 2010, (c) 1200 UTC 21 Sep 2010, and (d) 0000 UTC 22 Sep 2010 (unpublished figure provided by H. Archambault).....	53
Figure 39.	Frequency distribution of RWT lifetime in the ERA-40 data. Each bin has the width of one day. The different shadings refer to the different seasons. The error bars denote \sqrt{N} (where N is the total count in the respective bin), which we take as a measure for the statistical error, divided by the number of considered months and thus scaled to the occurrence of RWTs per months: (a) absolute choice of τ ($\tau = 35 \text{ m s}^{-1}$); (b) relative choice of τ ($\tau^* = 3.5$ (from GW13)).	56
Figure 40.	Scatter-plots showing the correlation between different RWT properties: (a) lifetime plotted against the longitudinal extent; and (b) mean amplitude plotted against the lifetime. The central line (red line) depicts the median of the marginal distribution corresponding to a given bin on the x -axis, and the outer lines (green lines) depict the corresponding 20% and 80% percentile, respectively (from GW13).	57
Figure 41.	Distribution of the longitudes of onset of RWTs with a minimum lifetime of 4 days (dark/black line, left scale) and 9 days (scaled by a factor of 2, pale/red line, right scale), respectively. MAM, spring; JJA, summer; SON, autumn; DJF, winter. The data, which are available with a resolution of 2.5° in longitude, have been smoothed by a 3-point running mean. The lighter shaded area represents the respective estimate for the statistical error; it was obtained from the square root of the count in each bin, suitably calibrated to the number of RWTs per month and using Gaussian error propagation to deal with the running average. The relatively small bin width is associated with large statistical error, but the structure of the distribution manifests more clearly than with a coarser bin resolution (from GW13).	59
Figure 42.	As in Figure 41, except for longitude of decay (from GW13).....	61
Figure 43.	Distribution of RWT initiation longitudes in the ERA-Interim derived climatology. RWTs of a minimum lifetime of four (nine) days are shown using the black (red) line and the left (right) scale. Seasons are denoted by MAM (spring), JJA (summer), SON (fall), and DJF (winter). Longitude bins are 5° wide and are smoothed by a 3-point running mean.	63

Figure 44.	Same as for Figure 43 except for longitudes of RWT decay.....	64
Figure 45.	Same as for Figure 21, except for (a) 0000 UTC 25 Oct 2010, (b) 1200 UTC 25 Oct 2010, (c) 0000 UTC 26 Oct 2010, and (d) 1200 UTC 26 Oct 2010 (unpublished figure provided by H. Archambault).....	66
Figure 46.	Same as for Figure 21, except for (a) 0000 UTC 27 Oct 2010, (b) 0000 UTC 27 Oct 2010, (c) 1200 UTC 27 Oct 2010, and (d) 0000 UTC 28 Oct 2010 (unpublished figure provided by H. Archambault).....	67
Figure 47.	Same as for Figure 21, except for (a) 1200 UTC 28 Oct 2010, (b) 0000 UTC 29 Oct 2010, (c) 0000 UTC 29 Oct 2010, and (d) 1200 UTC 29 Oct 2010 (unpublished figure provided by H. Archambault).....	68
Figure 48.	Same as for Figure 24 except from 0000 UTC 25 Oct 2010 to 0000 UTC 29 Oct 2010. (Image provided by the NOAA/ESRL Physical Sciences Division).	69
Figure 49.	Same as for Figure 21, except for (a) 0000 UTC 30 Oct 2010, (b) 1200 UTC 30 Oct 2010, (c) 0000 UTC 31 Oct 2010, and (d) 1200 UTC 31 Oct 2010 (unpublished figure provided by H. Archambault).....	70
Figure 50.	Same as for Figure 21, except for (a) 0000 UTC 01 Nov 2010, (b) 1200 UTC 01 Nov 2010, (c) 0000 UTC 02 Nov 2010, and (d) 1200 UTC 02 Nov 2010 (unpublished figure provided by H. Archambault).....	71
Figure 51.	Same as for Figure 24 except from 0000 UTC 29 Oct 2010 to 0000 UTC 06 Nov 2010. (Image provided by the NOAA/ESRL Physical Sciences Division).	72
Figure 52.	Same as for Figure 23, except for 0000 UTC 31 Oct 2010 (figure provided by H. Archambault).	73
Figure 53.	A 1-day SLP anomaly (color shading, hPa) from the NCEP operational dataset for 31 Oct 2010. (Image provided by the NOAA/ESRL Physical Sciences Division).	74
Figure 54.	A 1-day 1000 hPa wind anomaly (color shading, m s^{-1}) from the NCEP operational dataset for 31 Oct 2010. (Image provided by the NOAA/ESRL Physical Sciences Division).	74
Figure 55.	Same as for Figure 21, except for (a) 1200 UTC 15 Sep 2006, (b) 0000 UTC 16 Sep 2006, (c) 1200 UTC 16 Sep 2006, and (d) 0000 UTC 17 Sep 2006 (unpublished figure provided by H. Archambault).....	76
Figure 56.	Same as for Figure 21, except for (a) 0000 UTC 17 Sep 2006, (b) 1200 UTC 17 Sep 2006, (c) 0000 UTC 18 Sep 2006, and (d) 1200 UTC 18 Sep 2006 (unpublished figure provided by H. Archambault).....	77
Figure 57.	Same as for Figure 21, except for (a) 0000 UTC 19 Sep 2006, (b) 1200 UTC 19 Sep 2006, (c) 0000 UTC 20 Sep 2006, and (d) 1200 UTC 20 Sep 2006 (unpublished figure provided by H. Archambault).....	78
Figure 58.	Same as for Figure 21, except for (a) 0000 UTC 21 Sep 2006, (b) 1200 UTC 21 Sep 2006, (c) 0000 UTC 22 Sep 2006, and (d) 1200 UTC 22 Sep 2006 (unpublished figure provided by H. Archambault).....	79
Figure 59.	Same as for Figure 21, except for (a) 0000 UTC 23 Sep 2006, (b) 1200 UTC 23 Sep 2006, (c) 0000 UTC 24 Sep 2006, and (d) 1200 UTC 24 Sep 2006 (unpublished figure provided by H. Archambault).....	80

Figure 60.	Same as for Figure 24 except with features of RWT number 6824 labeled. (Image provided by the NOAA/ESRL Physical Sciences Division).	81
Figure 61.	Same as for Figure 23, except for 0000 UTC 23 Sep 2006 (figure provided by H. Archambault).	82
Figure 62.	Same as for Figure 53, except for 23 Sep 2006. (Image provided by the NOAA/ESRL Physical Sciences Division).	83
Figure 63.	Same as for Figure 54 except at the 850 hPa level for 23 Sep 2006. (Image provided by the NOAA/ESRL Physical Sciences Division).	83
Figure 64.	Same as for Figure 21, except for (a) 1200 UTC 23 Sep 2006, (b) 0000 UTC 24 Sep 2006, (c) 1200 UTC 24 Sep 2006, and (d) 0000 UTC 25 Sep 2006 (unpublished figure provided by H. Archambault).	85
Figure 65.	Same as for Figure 21, except for (a) 0000 UTC 25 Sep 2006, (b) 1200 UTC 25 Sep 2006, (c) 0000 UTC 26 Sep 2006, and (d) 1200 UTC 26 Sep 2006 (unpublished figure provided by H. Archambault).	86
Figure 66.	Same as for Figure 21, except for (a) 1200 UTC 26 Sep 2006, (b) 0000 UTC 27 Sep 2006, (c) 1200 UTC 27 Sep 2006, and (d) 0000 UTC 28 Sep 2006 (unpublished figure provided by H. Archambault).	87
Figure 67.	Same as for Figure 21, except for (a) 1200 UTC 28 Sep 2006, (b) 0000 UTC 29 Sep 2006, (c) 1200 UTC 29 Sep 2006, and (d) 0000 UTC 30 Sep 2006 (unpublished figure provided by H. Archambault).	88
Figure 68.	Same as for Figure 21, except for (a) 1200 UTC 30 Sep 2006, (b) 0000 UTC 01 Oct 2006, (c) 1200 UTC 01 Oct 2006, and (d) 0000 UTC 02 Oct 2006 (unpublished figure provided by H. Archambault).	89
Figure 69.	Same as for Figure 21, except for (a) 1200 UTC 02 Oct 2006, (b) 0000 UTC 03 Oct 2006, (c) 1200 UTC 03 Oct 2006, and (d) 0000 UTC 04 Oct 2006 (unpublished figure provided by H. Archambault).	90
Figure 70.	Same as for Figure 24 except anomalies are averaged between 40°–65°N from 0000 UTC 23 Sep 2006 to 0000 UTC 05 Oct 2006. (Image provided by the NOAA/ESRL Physical Sciences Division).	91
Figure 71.	Same as for Figure 23, except for 0000 UTC 03 Oct 2006 (figure provided by H. Archambault).	92
Figure 72.	Same as for Figure 53, except for 03 Oct 2006. (Image provided by the NOAA/ESRL Physical Sciences Division).	93
Figure 73.	Same as for Figure 54, except for 03 Oct 2006. (Image provided by the NOAA/ESRL Physical Sciences Division).	93
Figure 74.	Same as for Figure 21, except for (a) 0000 UTC 19 Sep 2010, (b) 1200 UTC 19 Sep 2010, (c) 0000 UTC 20 Sep 2010, and (d) 1200 UTC 20 Sep 2010 (unpublished figure provided by H. Archambault).	95
Figure 75.	Same as for Figure 21, except for (a) 0000 UTC 21 Sep 2010, (b) 1200 UTC 21 Sep 2010, (c) 0000 UTC 22 Sep 2010, and (d) 1200 UTC 22 Sep 2010 (unpublished figure provided by H. Archambault).	96
Figure 76.	Same as for Figure 21, except for (a) 0000 UTC 23 Sep 2010, (b) 1200 UTC 23 Sep 2010, (c) 0000 UTC 24 Sep 2010, and (d) 1200 UTC 24 Sep 2010 (unpublished figure provided by H. Archambault).	97

Figure 77.	Same as for Figure 21, except for (a) 0000 UTC 25 Sep 2010, (b) 1200 UTC 25 Sep 2010, (c) 0000 UTC 26 Sep 2010, and (d) 1200 UTC 26 Sep 2010 (unpublished figure provided by H. Archambault).....	98
Figure 78.	Same as for Figure 24 except anomalies are averaged between 45°–65°N from 0000 UTC 18 Sep 2010 to 0000 UTC 28 Sep 2010. (Image provided by the NOAA/ESRL Physical Sciences Division).....	99
Figure 79.	Same as for Figure 23, except for 0000 UTC 26 Sep 2010 (figure provided by H. Archambault).	100
Figure 80.	Same as for Figure 53, except for 26 Sep 2010. (Image provided by the NOAA/ESRL Physical Sciences Division).	101
Figure 81.	Same as for Figure 54, except for 26 Sep 2010. (Image provided by the NOAA/ESRL Physical Sciences Division).	101
Figure 82.	Histogram of the number (left axis) and percentage (right axis) of RWTs listed in Table 1 initiated by each of the four triggering mechanisms.....	103
Figure 83.	Longitudinal breakdown of RWT triggers as indicated by RWT starting locations from the Glatt and Wirth climatology.	105
Figure 84.	Number of RWTs initiated by longitude. Longitude bins are 10° wide.	106

LIST OF TABLES

Table 1.	RWTs chosen for further analysis of their triggering mechanisms.	31
Table 2.	Seasonal breakdown of longer-lived RWTs identified in the ERA-40 dataset by GW13.....	58
Table 3.	Same as for Table 2 for the ERA-Interim derived RWT climatology.....	62
Table 4.	Number and percentage of RWTs initiated by each triggering mechanism. .	104

THIS PAGE INTENTIONALLY LEFT BLANK

LIST OF ACRONYMS AND ABBREVIATIONS

APE	available potential energy
DRV	diabatic Rossby vortex
DT	dynamic tropopause
EC	extratropical cyclone
ECMWF	European Center for Medium-Range Weather Forecasts
EDO	experiment design overview
EKE	eddy kinetic energy
ERA-40	ECMWF 40-Year Reanalysis
ESRL	Earth System Research Laboratory
ET	extratropical transition
GFS	Global Forecast System
IW	irrotational wind
LHR	latent heat release
NHC	National Hurricane Center
NOAA	National Oceanic and Atmospheric Administration
NWP	numerical weather prediction
PVA	positive vorticity advection
PV	potential vorticity
PVU	potential vorticity unit
RWT	Rossby wave train
SLP	sea level pressure
TC	tropical cyclone
TPV	tropopause polar vortex
WCB	warm conveyor belt
WRF	Weather Research and Forecasting

THIS PAGE INTENTIONALLY LEFT BLANK

ACKNOWLEDGMENTS

I want to thank my advisor, Rich, for his guidance.

I want to thank the Navy for the opportunities I've been given.

I want to thank my friends and family for their support.

Most of all, I want to thank my wife, who reminds me every day what life is all about.

For Jackson...

THIS PAGE INTENTIONALLY LEFT BLANK

I. INTRODUCTION

A. DEFINITION OF A ROSSBY WAVE TRAIN

The midlatitude jet stream can be defined by a heightened potential vorticity (PV) gradient along steeply sloping isentropic surfaces. This tube-like region of enhanced PV gradient defines the waveguide and provides the mean flow on which atmospheric Rossby waves develop and propagate (Schwierz et al. 2004). Figure 1 depicts the waveguide graphically as presented by Schwierz et al. (2004). Figure 1a shows a polar view of the “instantaneous isentropic PV gradient” on the 320 K isentropes (Schwierz et al. 2004). In Figure 1b, a cross section taken along the heavy black line in Figure 1a highlights the features of the waveguide. The waveguide and the region of greatest winds, as indicated by the dashed isotachs, are collocated with the strongest gradient of PV (i.e. where the constant PV lines are most tightly packed and the PV gradient is shaded darkest).

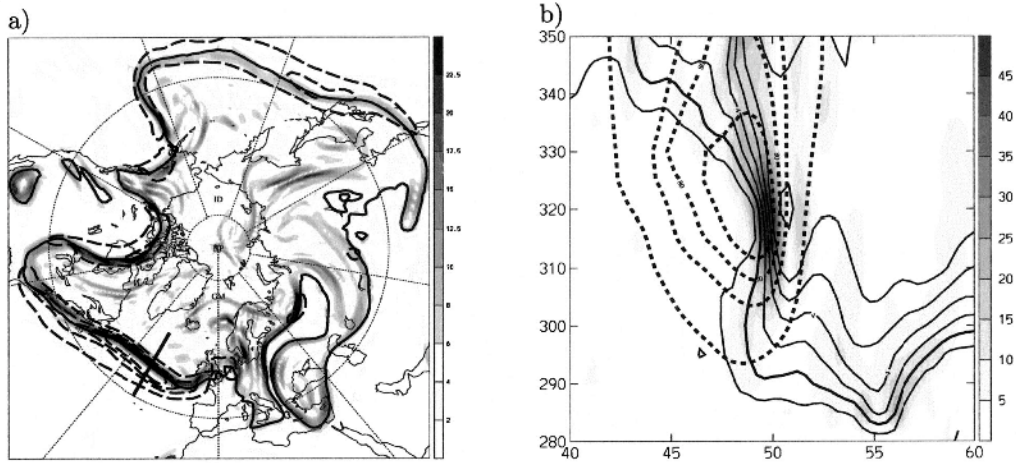


Figure 1. Instantaneous isentropic PV gradient on 1800 UTC 24 Dec 1999 (shaded, units 10^{-6} PVU m^{-1}). (a) On the 320-K isentropes, 2-PVU PV contour and wind speed (contours 50, 70, 80, 90 $m s^{-1}$) overlaid. (b) South-north cross section at 30°W. Vertical coordinate: θ ; PV isolines [1,2 (bold) 3, 4, 5, 6, 8 PVU]; and 50, 70, 80, 90 $m s^{-1}$ isotachs (dashed) overlaid (from Schwierz et al. 2004).

It is necessary to understand the composition of the waveguide on which Rossby waves propagate, as they are a key component of atmospheric dynamics, particularly with regard to extratropical cyclogenesis and its associated weather impacts. This cyclogenesis is conventionally explained through exponentially growing normal modes resulting from baroclinic instability (Glatt and Wirth 2013), but may also be described through upper-level atmospheric forcing over low-level baroclinic zones, which is defined by Type-B cyclogenesis (Petterssen and Smebye 1971). Because Rossby waves are zonally limited in their scale, Lee and Held (1993) describe a “packet of wave activity” propagating on the mean zonal flow. This “packet” is known as a Rossby wave train (RWT) and is a coherent envelope of baroclinic waves (Lee and Held 1993). Figure 2 shows an idealized schematic of a RWT as large-amplitude waves propagating on the tropopause (indicated by the heavy black line). Regions of net negative (positive) PV are shaded dark (light) gray and labeled by a minus (plus) sign. These correspond to the respective ridges and troughs of the RWT.

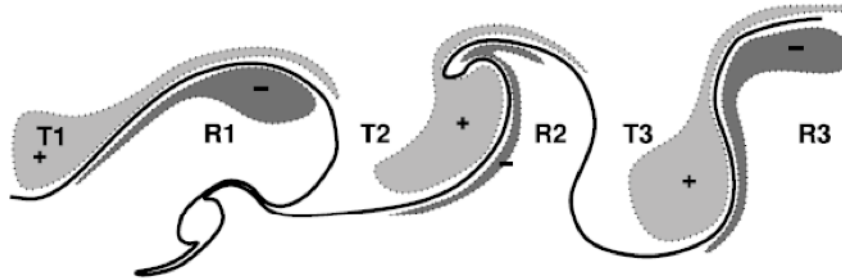


Figure 2. Schematic of the net diabatic PV (shaded) relative to large-amplitude waves on the tropopause (solid line). Positive diabatic PV is shaded lightly and marked with a “+”. Negative diabatic PV is shaded darkly and marked with a “-”. Troughs and ridges are marked sequentially beginning with a “T” and “R”, respectively (after Chagnon, Gray, and Methven 2013).

According to Chang (1993), the initial disturbance that becomes a RWT grows via the conversion of baroclinic available potential energy (APE), but the downstream development of waves is accomplished by radiating fluxes from upstream perturbations. Downstream development is possible because the group velocity of RWTs exceeds the phase velocity of any component wave. Through this mechanism, the RWT can create

upper-level atmospheric forcing far downstream where it would otherwise be absent, thus extending cyclogenesis into less unstable regions (Chang 1993). Nielsen-Gammon (2001) observed high-amplitude RWTs propagating nearly half the extent of the Northern Hemisphere. Lee and Held (1993) demonstrated the presence of RWTs in atmospheric models of varying complexity and showed downstream development due to these baroclinic wave packets is a prominent feature. Chang (1993) examined the downstream development of baroclinic wave packets in terms of their eddy kinetic energy (EKE) budget and the sources and sinks of EKE. Through this energetics analysis, the initial growth of RWTs through conversion of APE over baroclinic regions was confirmed, and it was further shown that ageostrophic fluxes of geopotential height were primarily responsible for wave growth over weakly baroclinic zones (Chang 1993). In these areas, baroclinic and barotropic energy conversions are less significant. For these reasons, Chang (1993) suggested RWTs play a significant role in downstream cyclogenesis over regions of less instability.

The initial perturbation to the waveguide can be triggered by a number of atmospheric phenomena. These include tropopause polar vortices (TPVs), warm conveyor belts (WCBs) associated with extratropical cyclones (ECs), diabatic Rossby vortices (DRVs), and the extratropical transition (ET) of tropical cyclones (TCs). This thesis will examine the dynamics of each potential trigger in detail and further describe the dynamics by which they perturb the waveguide and trigger RWT development. A primary focus is on methods to differentiate between triggering mechanisms.

B. ROSSBY WAVE TRAIN TRIGGERING MECHANISMS

Each of the RWT triggering mechanisms discussed will be examined through the framework of PV. A general form of PV tendency is given in Equation 1.

$$\frac{d(PV)}{dt} = -g \frac{d\dot{\theta}}{dt} (\zeta_0 + f) \quad (1)$$

Here, g is the gravitational force, $d\dot{\theta}/dt$ is the vertical gradient of diabatic heating, and $(\zeta_0 + f)$ is absolute vorticity. Equation 1 illustrates that PV creation or destruction is a

result of the vertical gradient of diabatic heating. With respect to WCBs, DRVs, and ET, as warm moist air rises from the boundary layer, latent heat release (LHR) results in an increase in potential temperature, an upward negative potential temperature, and the creation of PV. This occurs up to the level of maximum heating. Above this level, the sign of the vertical gradient of diabatic heating reverses and a negative PV tendency is created. The resulting low PV anomaly below the tropopause is characteristic of WCBs, DRVs, and ET. Figure 3 shows idealized representations of this process for both (a) “impulsive diabatic heating” and (b) “steady condensation” (Wernli and Davies 1997). In Figure 3, hatched regions depict diabatically produced PV anomalies with signs indicating positive or negative. Solid lines are isentropes in Figure 3a and solid arrows depict parcel trajectories in Figure 3b. Shaded regions indicate the location of diabatic heating. $D\theta$ and DP show “material tendencies of potential temperature and potential vorticity, respectively” (Wernli and Davies 1997). In contrast with the “steady condensation” depicted in Figure 3b, and its positive PV anomaly produced near the level of maximum heating, Figure 3a depicts how the cloud diabatic effects of RWT triggering mechanisms produce a vertical “PV-dipole” (Wernli and Davies 1997).

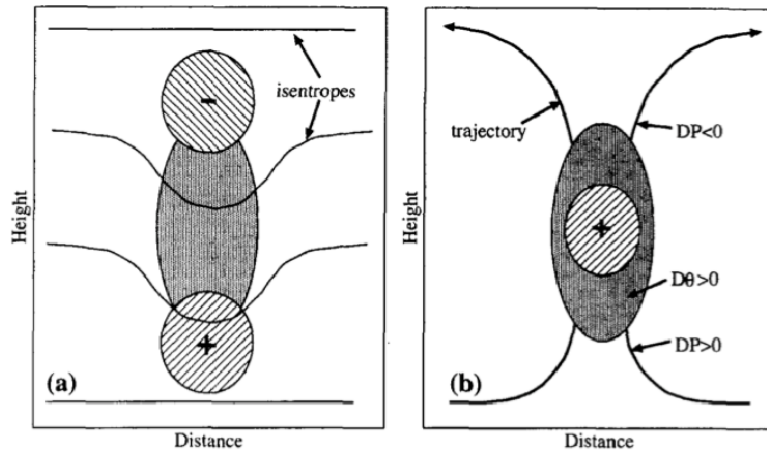


Figure 3. Schematic vertical cross-sections showing diabatically produced PV anomalies (hatched regions with a plus or minus sign) for the idealized cases of (a) “impulsive diabatic heating”, and (b) “steady condensation” in a frontal zone. Shading indicates the regions of diabatic heating. In (a) the solid lines are isentropes and in (b) the bold lines with arrows refer to air-parcel trajectories. $D\theta$ and DP denote material tendencies of potential temperature and potential vorticity, respectively (from Wernli and Davies 1997).

Although TPVs may result in similar destruction of PV above the level of maximum heating, they undergo significant radiational cooling from cloud tops in the upper levels (Cavallo and Hakim 2009). This increase in potential temperature creates an upward gradient of potential temperature and overcomes the PV destruction above the level of maximum heating, resulting in a positive PV anomaly near the tropopause. Thus, all four phenomena can be examined as PV anomalies near the waveguide.

1. Tropopause Polar Vortex

A tropopause polar vortex (TPV) is defined as a positive PV anomaly occurring near the strong vertical PV gradient between the stratosphere and troposphere (Cavallo and Hakim 2009). Tropopause polar vortices are identified by closed contours of potential temperature along the dynamic tropopause (the dynamic tropopause being represented by the two PVU surface). Although TPVs can live longer than one month, owing to the reduced wind shear in the polar regions, Hakim and Canavan (2005) define TPVs as vortices that live at least two days and spend at least 60% of their lifecycle above 65°N. Further characterization of a TPV includes a horizontal length scale of typically less than 2000 km (Cavallo and Hakim 2009).

The PV tendency associated with a numerical simulation of a TPV is presented in Figure 4. The TPV is strengthened and maintained primarily through diabatic processes at the tropopause level (Cavallo and Hakim 2009). Furthermore, radiational cooling from cloud tops generates PV at the dynamic tropopause, and is primarily responsible for the cold core polar cyclone intensification (Figure 4b). While latent heating below will seek to destroy upper-level PV, as Figure 4c shows, this latent heating and negative PV tendency occurs lower in the troposphere in the presence of larger cloud water content and can be offset by cloud-top radiational cooling aloft (Cavallo and Hakim 2009).

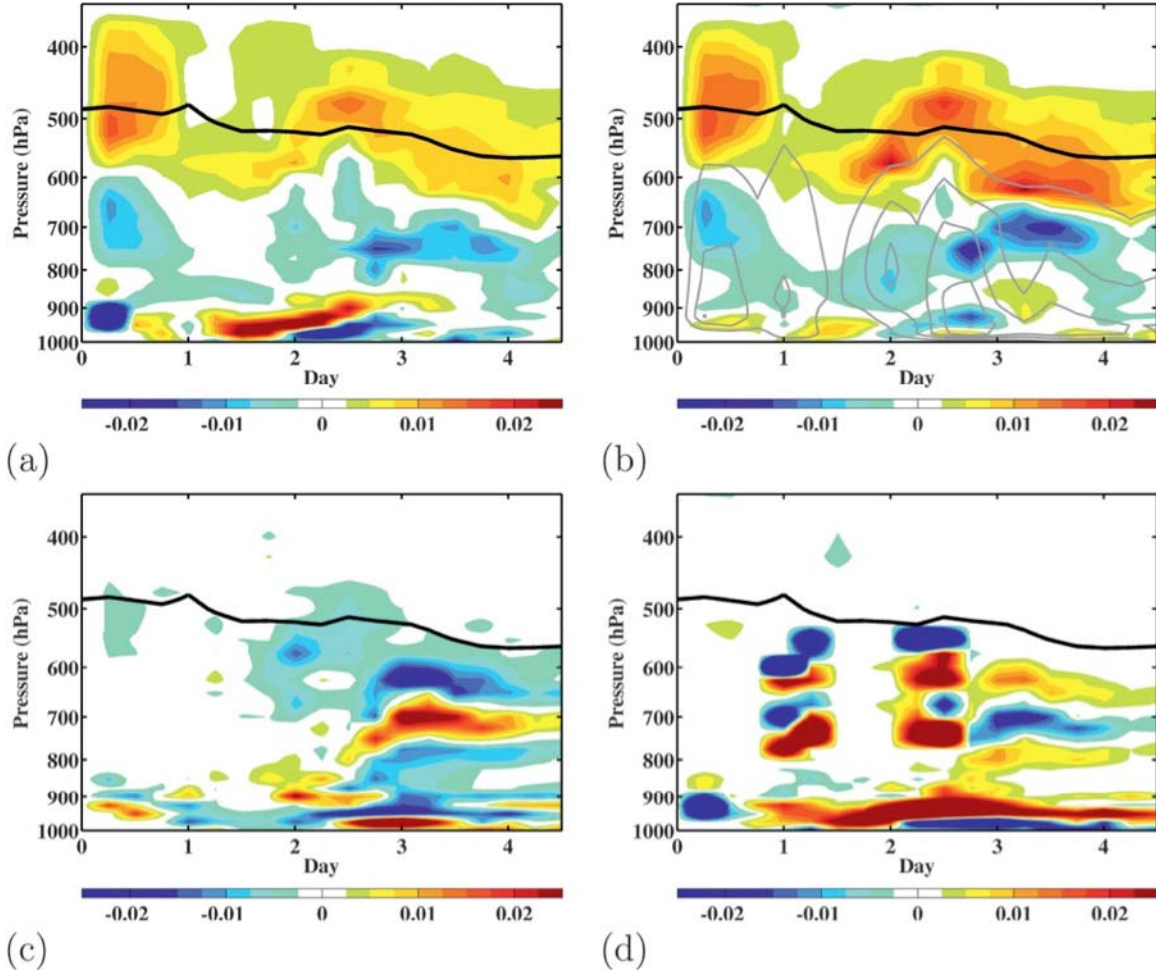


Figure 4. Time-height sections from a Weather Research and Forecasting (WRF) simulation during 0000 UTC 5 Nov 2005–0000 UTC 10 Nov 2005 of the Ertel PV (EPV) tendency (PVU h^{-1}) due to (a) all diabatic processes, (b) radiation (colors) and cloud water (sum of liquid and ice mixing ratios; contours every 0.004 g kg^{-1}), (c) latent heating, and (d) the sum of the planetary boundary layer scheme, cumulus scheme, and frictional processes. All fields are averaged within the area encompassed by the 285 K closed tropopause potential temperature contour. The thick black line represents the 2 PVU surface. Labels on the abscissa are days from the start of the simulation. The EPV tendency color interval is $0.0025 \text{ PVU h}^{-1}$ (from Cavallo and Hakim 2009).

To better understand the frequency and relative locations of TPVs, Kew et al. (2010) created a TPV climatology using ten years (1991–2001) of winter months from the ERA-40 dataset to identify and track TPVs from genesis to lysis. Kew et al. (2010) define TPVs based on the “effective amplitude” of their PV relative to the surrounding atmosphere. These features are then tracked throughout their lifecycle.

In their climatology, Kew et al. (2010) present an example of the isentropic patterns over the North Pole (Figure 5). Of importance to the research in this thesis, are the locations of positive PV anomalies at points J1 and J2 in Figure 5a. The proximity of these TPVs to the dynamic tropopause (indicated by the 2 PVU line, red shading) indicates the potential for interactions where the TPV can perturb the waveguide and initiate RWT formation. The TPV perturbs the waveguide dynamically through vertical and horizontal vorticity and momentum exchanges with the mean zonal flow of the jet. Kew et al. (2010) equate a PV anomaly with a relative vorticity maximum at upper-levels and state it is analogous to an upper-level jet streak or trough and, as such, can play a similar role in Type-B cyclogenesis. The features marked S1 and S2 are remnants of the mature development of a baroclinic wave. They constitute “intrusions of stratospheric air down into the troposphere” (Kew et al. 2010). The cross-section in Figure 5b is referenced by the black line near 150°E on Figure 5a. This image shows the vorticity structure (thin solid lines represent relative vorticity) of a positive PV anomaly located near the Pole. The vorticity signature of this TPV extends below the 500 hPa level. This interaction with the troposphere can serve as a precursor to cyclogenesis (Kew et al. 2010).

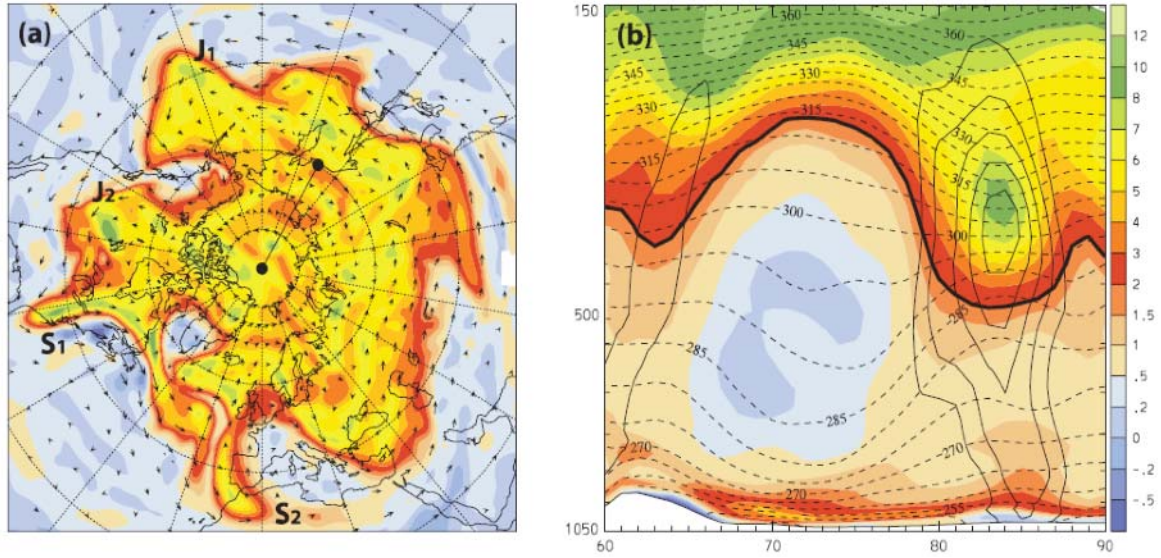


Figure 5. (a) PV on the 320-K isentropic at 0600 UTC 20 Dec 2000, taken from the ERA-40 dataset. Numerous mesoscale PV structures (see $PV > 7$ PVU) characterize the distribution. Labels S1 and S2 show locations of streamers. Anomalies J1 and J2 are situated alongside the jet. The dynamical tropopause (red shading) is coincident with the jet and separates the stratospheric portion that encompasses the Pole from the surrounding tropospheric portion of the isentropic surface. (b) Vertical distribution of PV (color) and potential temperature (dashed contours) at 150°E. The limits of the meridional cross section are marked by solid black circles in (a). The dynamical tropopause is outlined in thick black. Thin solid contours show positive values of the vertical component of relative vorticity (interval $2.5 \times 10^{-5} \text{ s}^{-1}$) (from Kew et al. 2010).

In the results of their TPV climatology, Kew et al. (2010) showed that TPV genesis occurs most often over Northwest Greenland, northernmost Canada, and Alaska. Secondary maxima occur over the eastern edge of the Kamchatka Peninsula and the Sea of Japan, as well as the Norwegian Sea. Kew et al. (2010) further states that, “to a measure,” lysis and genesis regions are coincident. There are dense lysis regions near northern Greenland and west of Baffin Island, with secondary maxima over Alaska and extending from northeast China to the southern tip of the Kamchatka Peninsula.

In addition to understanding regions of genesis and lysis, the frequency of occurrence and mean track of TPVs is also important to the triggering of RWTs. Figure 6 shows the event density (a) and track density (b) of PV anomalies on the 320 K isentropic for the ten years analyzed in this climatology. Kew et al. (2010) notes the high PV

anomaly track densities poleward of the Pacific and Atlantic storm track regions, and suggests a link between these PV anomalies and “the creation of the surface storm tracks.”

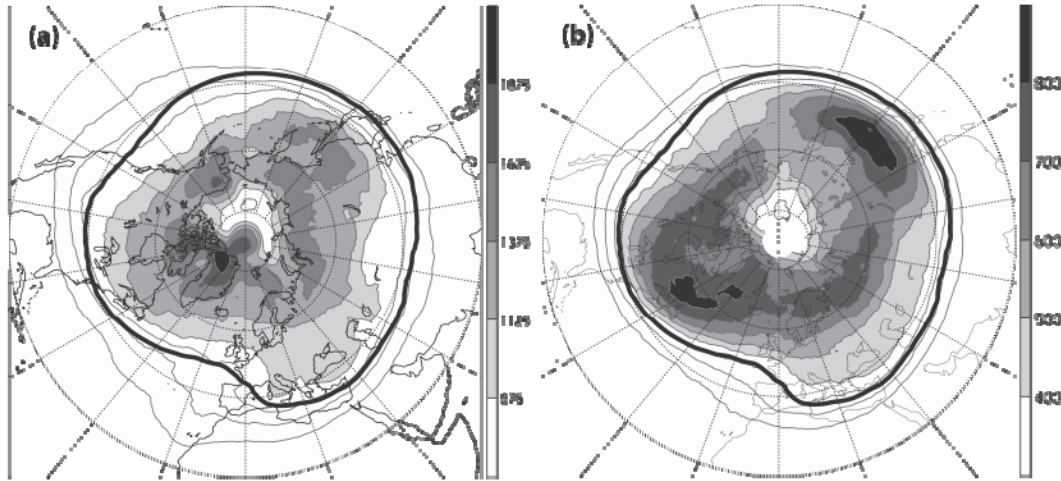


Figure 6. Winter climatology of PV anomalies identified on 320 K: (a) event density and (b) track density. Densities show 10-yr winter-season totals over circular areas 5° radius centered on each grid point. A minimum lifetime threshold of 1 day is applied. Amplitudes of the included structures attain at least 1 PVU within a lifetime. The mean dynamical tropopause is overlaid (thick black line) (from Kew et al. 2010).

2. Warm Conveyor Belt

According to Eckhardt et al. (2004), a warm conveyor belt (WCB) associated with an EC is a region of intensely rising moist air that ascends from near the surface to the upper troposphere on a time scale of roughly two days. Significant poleward movement accompanies this ascension. To illustrate the meridional and vertical movement of the WCB over time, Figure 7 shows plan and cross-section views of air parcel trajectories associated with a WCB in the western North Atlantic. Beginning at 1200 UTC 23 Jan 1987, black circles mark 24-hour positions of the parcels. Within the first 48 hours, the WCB moves poleward from 30°N to near 75°N and vertically from below 1000 m to above 8000 m.

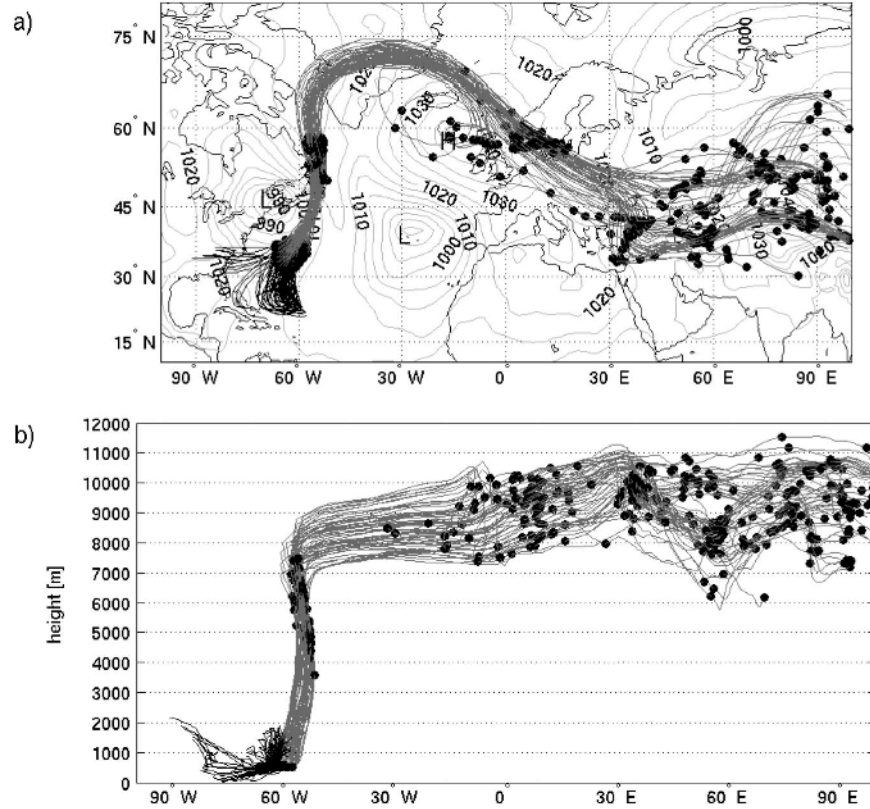


Figure 7. Six-day trajectories starting 1200 UTC 23 Jan 1987, of which the first 2 days were identified as a WCB. (a) The forward trajectories (gray) and 3-day backward trajectories (black) from the starting locations of the forward trajectories. Positions along the forward trajectories are marked every 24 h. Sea level pressure (light gray) contour lines are drawn every 10 hPa for the trajectory starting time (1200 UTC 23 Jan 1987). For clarity, only those WCB trajectories associated with the cyclone over the eastern seaboard of North America are drawn. (b) Vertical projection of the trajectories shown in (a) (from Eckhardt et al. 2004).

WCBs are important for three reasons. First, as the airstream rises, latent heat is released and positive PV is created in the lower and mid-troposphere, furthering development of the EC. Second, WCBs mix the atmospheric boundary layer (ABL) into the upper troposphere and lower stratosphere. Third, WCB divergent outflow regions near the tropopause constitute a negative PV anomaly and have the potential to perturb the waveguide and elicit RWT formation (Eckhardt et al. 2004; Grams et al. 2011). Grams et al. (2011) further state that as air within the WCB ascends, LHR below the level

of maximum heating generates PV, in accordance with Equation 1. Correspondingly, above the level of maximum heating, PV is diabatically consumed, creating a low PV anomaly below the tropopause in the vicinity of the WCB outflow. The impact of this anomaly with the waveguide can advect lower PV air, driving an intensification of the local PV gradient and perturbation of the waveguide, initiating a RWT.

To assess the potential frequency with which WCBs perturb the waveguide, Madonna et al. (2014) provides a WCB climatology created using trajectories calculated from the Interim European Center for Medium-Range Weather Forecasts (ECMWF) Re-analysis (ERA-Interim) dataset from 1979–2010. According to this climatology, and consistent with previous climatologies, WCBs occur more frequently in winter than summer and preferentially form in the western North Atlantic and western North Pacific from 25°–50°N. Increasing baroclinicity with the transition to fall and winter corresponds with the increasing frequency of WCBs. Madonna et al. (2014) further state that, with the onset of winter, WCB initiation regions shift poleward between 2° and 5°. This brings WCBs in closer proximity to the midlatitude waveguide, increasing the opportunity for waveguide perturbation and RWT triggering.

In Figure 8, Madonna et al. (2014) show the climatological frequency of WCB starting points for the Northern Hemisphere winter (DJF). Colors show the percent of 6-hourly time steps in which WCBs ascend from the areas indicated. Regions shaded in red, where nearly 10% of 6-hourly time steps show WCBs ascending, appear over the western North Atlantic and western North Pacific. These conditions are not as prominent in Northern Hemisphere fall, though WCBs occur more frequently in fall than they do during the Northern Hemisphere summer minimum (Madonna et al. 2014). These regions of greater WCB frequency are consistent with climatological RWT genesis regions presented in Chapter III.

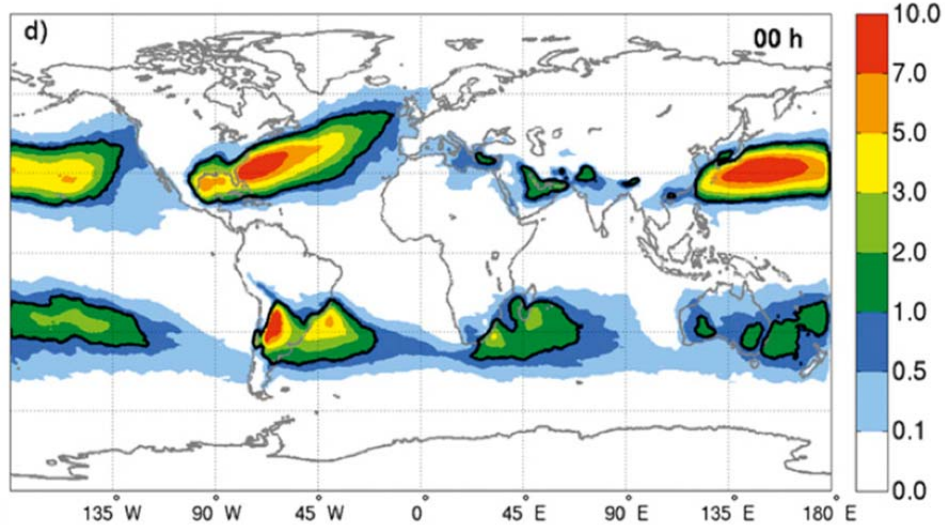


Figure 8. Climatological frequency of WCB trajectories in DJF at $t = 0$ h (WCB starting points). Colors represent the relative frequency (in percent) of WCB trajectories at each grid point. The black contour represents a WCB frequency of 1% at $t = 0$ h (after Madonna et al. 2014).

3. Diabatic Rossby Vortex

Boettcher and Wernli (2013, hereafter BW13) define a diabatic Rossby wave as a lower-tropospheric disturbance of positive PV that forms over baroclinic regions. It intensifies devoid of significant upper-level forcing and is diabatically dominated, that is, its growth is driven through the diabatic generation of positive PV at lower levels rather than the conversion of baroclinic APE. Numerous studies have been conducted on the idealized framework of moist baroclinic systems (Raymond and Jiang 1990; Snyder and Lindzen 1991). Parker and Thorpe (1995) first introduced the terminology diabatic Rossby wave. Highlighting the vortex like attributes of these diabatic Rossby waves, Moore and Montgomery (2004) introduced the term diabatic Rossby vortex (DRV).

Moore et al. (2008) state that the ratio of “diabatic to baroclinic generation of eddy APE” is useful in dynamically distinguishing baroclinic waves from DRVs. This ratio is larger for DRVs, thus they are diabatically dominated. In DRVs, the low-level (LHR), and subsequent positive PV created, elicits a downstream poleward flow of warm moist air. This airstream rises over isentropes to its lifting condensation level where additional low-level positive PV is created via the same mechanism. DRVs propagate

quickly through this creation of low-level positive PV that causes the DRV to reform at the location of the downstream poleward flow (BW13).

As demonstrated by Wernli et al. (2002) in their examination of the winter storm “Lothar” that occurred in December 1999, DRVs are important due to their role in explosive cyclogenesis. Moore and Montgomery (2004) describe the two-stage “process of explosive cyclone development.” Their research shows that the first stage begins with the independent formation of a lower-level region of cyclonic vorticity that intensifies through cloud diabatic processes, while stage two is usually explained through “nonlinear interaction between upper- and lower-level cyclonic disturbances” (Moore and Montgomery 2004). BW13 show that with sufficient intensity, the cyclonic circulation associated with the DRV can penetrate to the tropopause and provoke the creation of a trough, as was the case for the midlatitude cyclone named “Lothar.” Petterssen and Smebye (1971) first described this method of Type-A. Furthermore, Type-A cyclogenesis can also be explosive as defined by Sanders and Gyakum (1980).

Explosive cyclogenesis can also occur when the low-level DRV approaches the midlatitude waveguide and interacts with a previously existing upper-level trough. Further diabatic intensification results in a tropopause fold that merges the upper and lower-level PV anomalies (Wernli et al. 2002). The DRV at this stage supports deepening of the upper-level trough that prompts ridge development downstream and the formation of a RWT.

Several observational studies of DRVs have been conducted (Wernli et al. 2002; Moore et al. 2008; Boettcher and Wernli 2011). In 2008, Moore et al. (2008) conducted an analysis of a DRV that explosively deepened off the East Coast of the U.S., dropping approximately 10–30 cm of snow across the northeastern U.S. Figure 9 shows sea level pressure (SLP) contours of the storm as it developed. Heavy black lines indicate the locations of cross-sections of PV analyses presented in Figure 10. The storm deepens to a central pressure of 984 hPa at 1800 UTC 25 Feb 2005 (Figure 9f). Figure 10 shows the PV evolution of the storm through PV. In Figure 10a the dark shaded area indicates a region of positive PV associated with an approaching upper-level trough. This feature is upstream of a lower-level region of less positive PV that indicates the location of the

DRV. Over the next 24 hours both regions of positive PV intensify and merge, forming a “PV tower” by 1800 UTC 25 Feb 2005 (Moore et al. 2008).

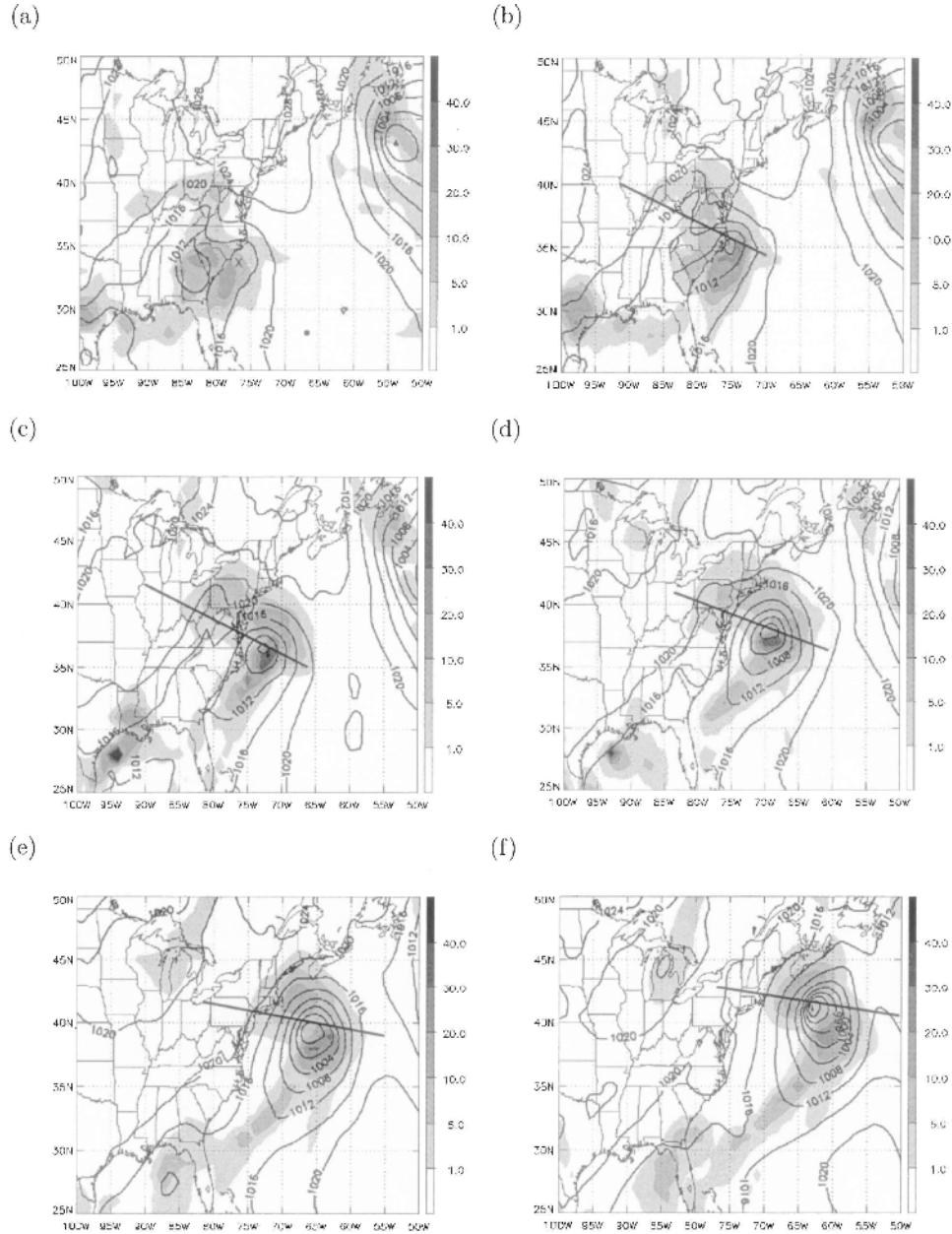


Figure 9. Sea level pressure (contours; hPa) and previous 6-h accumulated precipitation (shading; mm) from ECMWF analysis data beginning (a) 1200 UTC 24 Feb 2006 and every six hours after (b)–(f). Heavy black lines in (b) – (f) represent the location of cross-sections in Figure 10 (after Moore et al. 2008).

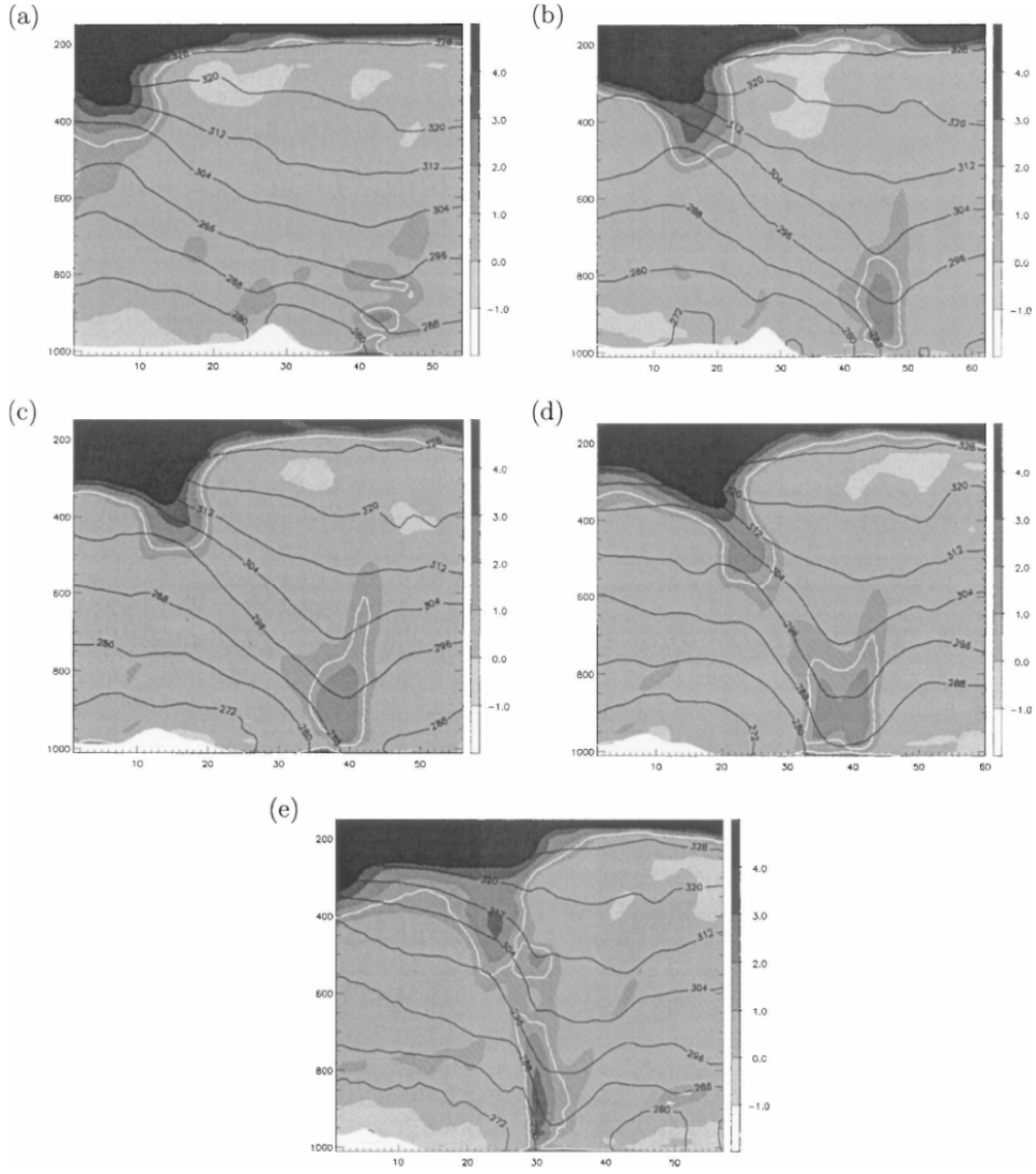


Figure 10. Vertical cross-section analysis of PV (shading; PVU; white contour represents the 1.5 PVU surface) and potential temperature (black contours; K) from ECMWF analysis data at (a) 1800 UTC 24 Feb 2006 and every 6 hours after (b)–(e). One grid point on the x axis is roughly equivalent to 50 km, and the white region on the lower boundary represents orography (from Moore et al. 2008).

BW13 created the first DRV climatology from an operational ECMWF analysis. As it relates to the data and methodology presented in this research, this climatology will be discussed in more detail in Chapter II. In general, however, DRVs tend to form preferentially in summer over the baroclinic regions near the warm western boundary currents of the North Atlantic and western North Pacific, as indicated in Figure 11 where light shaded bars represent the total number of DRVs during the years 2001–2010 and dark shaded bars show the portion of DRVs that intensified explosively, or “bombed,” as defined by Sanders and Gyakum (1980). DRVs occur with greater frequency over the Pacific. Of those that do occur in the Pacific, on average 12 deepen explosively each year, compared to five in the Atlantic. This amounts to 12.5% (14.7%) of the total number of DRVs occurring in the Atlantic (Pacific; BW13).

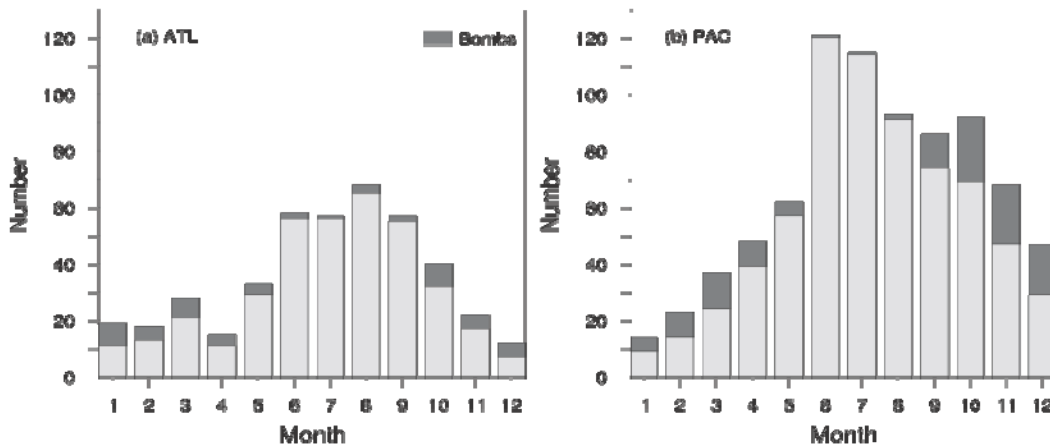


Figure 11. Monthly number of DRVs [DRVs] during the years 2001–10 in the (a) North Atlantic and (b) North Pacific (from BW13).

Most cases of explosive cyclogenesis of DRVs result from “interaction with a preexisting upper-level trough” (BW13). As these systems have the potential to cause severe damage, as evidenced by the winter storm “Lothar,” as well as excite RWT formation and the downstream development of sensible weather impacts, the average number of cases of explosive deepening is not insignificant. Moreover, BW13 go on to show that the percentage of total bombs initiated by DRVs is substantial, showing that DRVs serve as precursors for roughly 15% (20%) of bombs in the Atlantic (Pacific).

Figure 12 shows the number of bombs per month, from 2001–2010 (light gray bars), and the portion that were initiated by DRVs (dark gray bars). BW13 use these results to show that DRVs are statistically significant antecedents for bombs over the North Atlantic and North Pacific.

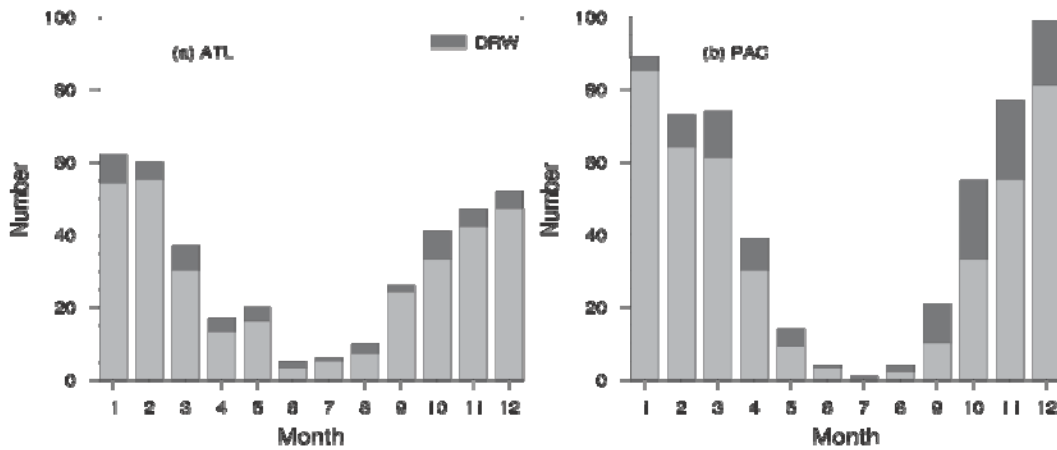


Figure 12. Monthly number of “cyclone bombs” (gray bars) during the years 2001–10 in the (a) North Atlantic and (b) North Pacific. Bombs with a DRV [DRV] precursor are indicated by dark gray shading (from BW13).

4. Extratropical Transition of a Tropical Cyclone

Tropical cyclones (TCs) are characterized by upper-tropospheric anticyclonic divergent outflow. Due to mid-latitude forcing, a TC can begin a poleward trajectory from its typical westward track. This transition into the mid-latitudes can cause changes in both the environment surrounding the TC as well as its own characteristics (Jones et al. 2003). Figure 13c shows the tracks of all TCs that underwent ET in the Atlantic from 1970–1999. Figure 13a,c indicates numerous occurrences of ET in the western North Pacific and Atlantic basins, areas favorable for RWT development. Figure 13b shows ET tracks for TCs in the Southern Hemisphere. As this research is focused on Northern Hemisphere RWTs, Southern Hemisphere triggering mechanisms will not be discussed.

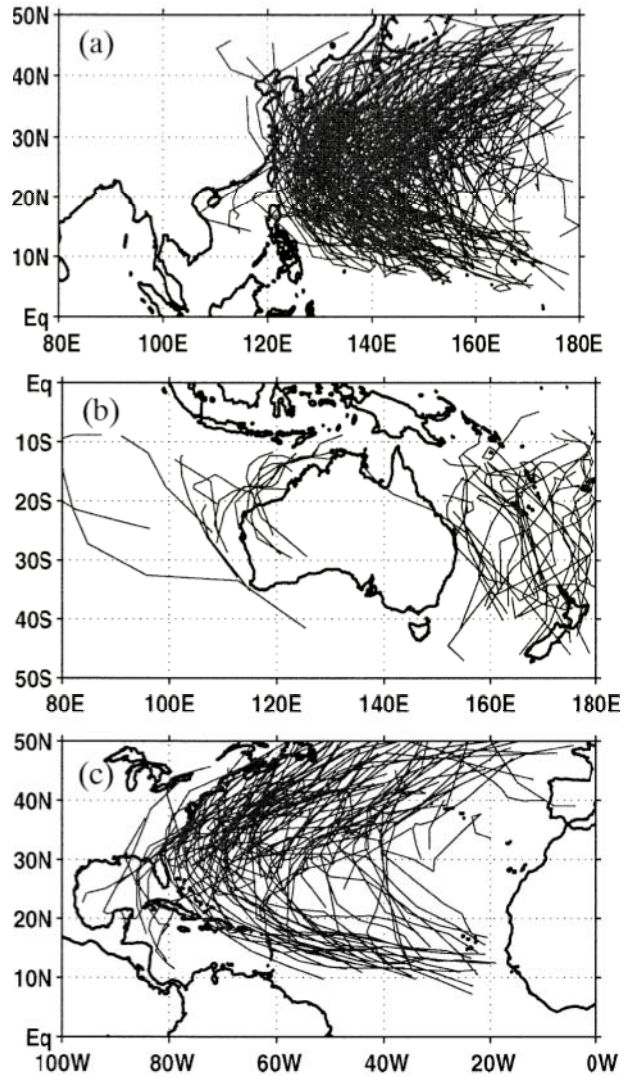


Figure 13. Tracks of all tropical cyclones that underwent extratropical transition during 1970–99. (a) Western North Pacific. Tracks of tropical cyclones defined to be extratropical in JTWC best-track data. (b) Southwest Pacific [data as in (a)] and southeast Indian Ocean [tracks of tropical cyclones that accelerated toward the southeast under the influence of a midlatitude frontal system and maintained gales into midlatitudes, the so-called captured cyclones in Foley and Hanstrum (1994); best-track data taken from <http://www.australiasevereweather.com/cyclones/history.htm>]. (c) North Atlantic. Tracks of tropical cyclones defined to be extratropical in National Hurricane Center best-track data (from Jones et al. 2003).

Klein et al. (2000) describe ET in terms of transformation and reintensification stages. They define the transformation stage of ET as beginning when imagery suggests asymmetries in the storm, particularly “a widespread decrease of deep convection in the western quadrant” of the storm (Klein et al. 2000). This stage is said to be complete when the system develops characteristics similar to a baroclinic cyclone. At this point, the storm can either reintensify as a baroclinic cyclone or decay. Figure 14 shows a schematic of this process for TCs undergoing ET in the western North Pacific from 1 Jun–31 Oct 1994–1998. Beginning with the transformation stage and ending with reintensification, the arrow indicating SLP increases at first, illustrating the weakening of the cyclone, followed by little reintensification (A), moderate reintensification (B), or deep reintensification (C). Transitioning TCs can perturb the midlatitude waveguide during either the transformation or reintensification stage, as well as before being classified as extratropical.

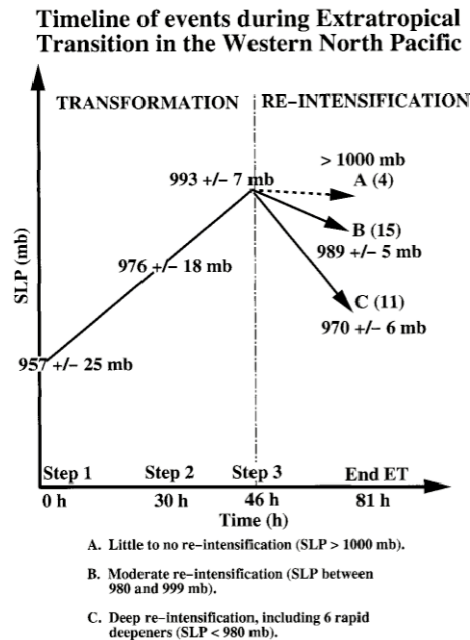


Figure 14. Schematic of the evolution of ET in the western North Pacific based on 30 cases that occurred from 1 Jun through 31 Oct during 1994–98. The times on the abscissa are subsequent to the beginning of the transformation stage. Means \pm standard deviation of SLP are listed for each step of transformation, and for the conclusion of the reintensification stage, with the number of cases observed in each of the three outcomes of reintensification depicted parenthetically (from Klein et al. 2000).

As a TC recurves into the sub-tropics and undergoes ET, its upper-level divergent outflow creates a negative PV anomaly near the tropopause (Riemer et al. 2008). Archambault et al. (2013) state that this divergent outflow impacts the waveguide and can be an indicator of Rossby wave genesis, specifically ridge building and intensification of the sub-tropical jet. This results from advection of low PV air by the divergent outflow and subsequent tightening of the meridional PV gradient. Figure 15 depicts an idealized extratropically transitioning TC interacting with the jet stream. Black lines are constant PV and their spacing indicates the increased PV gradient associated with the waveguide. As the divergent outflow (black vectors) of the transitioning TC impacts the waveguide, it advects lower PV air poleward, increasing the local PV gradient, resulting in the formation of a jet streak. Similar to the low PV anomaly created near the tropopause by a WCB, this advection of low PV air from the divergent outflow perturbs the otherwise zonally oriented waveguide and can trigger RWT formation. Riemer et al. (2008) further suggest that the downstream development characteristic of RWTs is one key way in which the energetics of ET is propagated downstream.

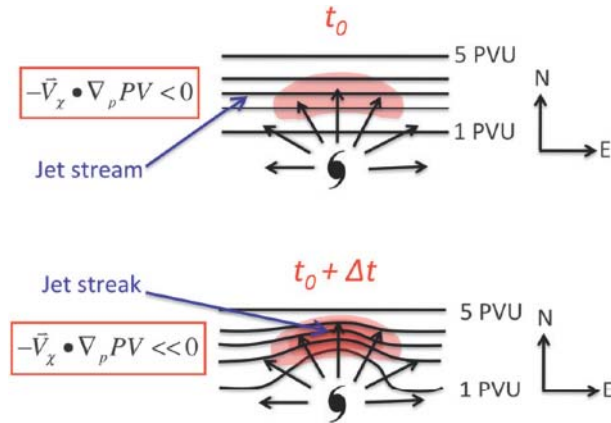


Figure 15. Schematic representation of ridge amplification and jet streak intensification associated with the divergent outflow of a TC impinging upon an upper-tropospheric jet stream/waveguide. Vectors represent the upper-tropospheric irrotational wind (i.e., divergent outflow) associated with the TC. Shading denotes negative PV advection by the irrotational wind (from Archambault et al. 2013).

According to Jones et al. (2003), almost every region of TC occurrence has some rate of ET events. Figure 16 shows the total numbers of tropical cyclones (open bars) and ET events (gray bars) by month from 1970–1999 in the Atlantic basin. A clear peak in both TCs and ET events is evident in September, while a large percentage of TCs undergo ET in October. This characteristic is germane to the motivation for this thesis.

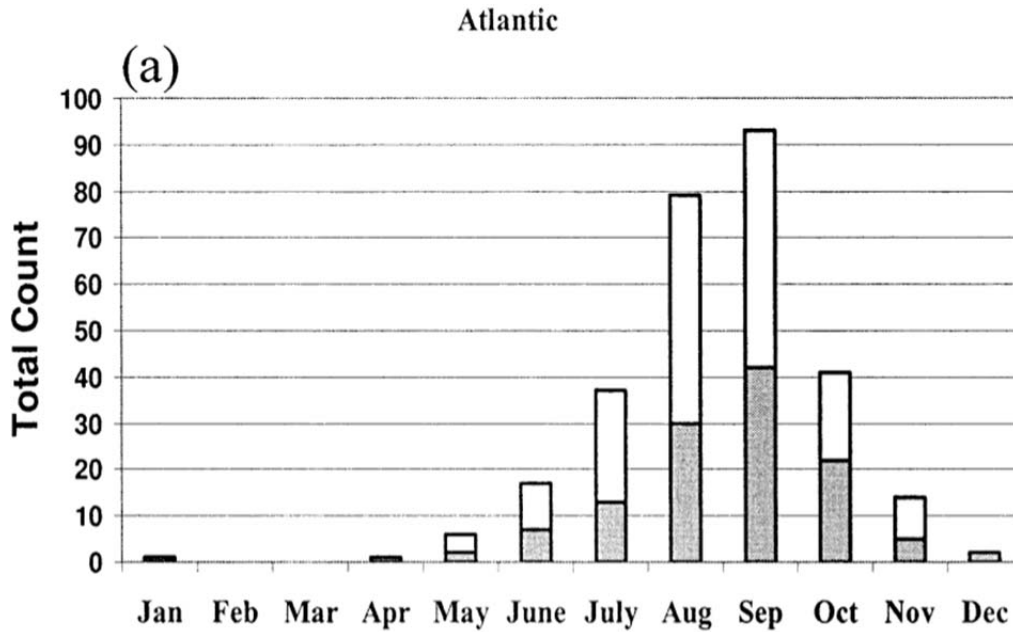


Figure 16. Monthly total number of tropical cyclones (open bars) in each basin during 1970–99 and the number of tropical cyclones that underwent extratropical transition (shaded bars). Data as in Figure 13 (after Jones et al. 2003).

C. MOTIVATION FOR STUDY

A potential experiment to study the interactions of triggering mechanisms and the North Atlantic waveguide is proposed to occur in fall, 2016. From the above, it is clear that RWTs may be triggered by a variety of phenomena (TPV, WCB, DRV, ET). An improved understanding of the triggers of RWTs will increase predictability of the midlatitude waveguide and the eventual downstream influence on weather and forecasts. Figure 17 depicts the area of a proposed experiment area over the North Atlantic, with representations of the general tracks of waveguide perturbations (colored arrows off

interactions between these disturbances and the waveguide is critical to improving NWP models. The goal of this thesis is to offer some insight into the relative frequency of occurrence of RWTs triggered by each type of disturbance, particularly if triggering occurred through perturbation of the North Atlantic waveguide.

THIS PAGE INTENTIONALLY LEFT BLANK

II. DATA AND METHODOLOGY

A. ROSSBY WAVE TRAIN CLIMATOLOGY

Glatt and Wirth (2013), hereafter GW13, developed automated techniques for identifying upper-tropospheric Rossby wave trains and objectively quantified their properties. These techniques were applied to the ECMWF 40 Year Re-analysis (ERA-40) to create a climatology of RWT objects in the Northern Hemisphere. This dataset identified preferential regions for RWT generation and decay. Additionally, significant variability in RWT longevity, as well as great seasonal variability was identified.

To accomplish this, GW13 began with a raw meridional wind field on the 250 hPa pressure level. An example of this is shown in the RWT analysis for 0000 UTC 7 Aug 2002 (Figure 18a). Assuming a standard Rossby wave form of $v(\lambda, t) = \text{Re}[E(\lambda, t)e^{ik\lambda}]$, GW13 extracted the wave envelope $E(\lambda, t)$ by removing the carrier wave ($e^{ik\lambda}$) phase variation. This wave envelope shown in Figure 18a describes the RWT, not its component waves. Because RWTs are a synoptic feature, GW13 also restrict the zonal wave number to the synoptic scale, defined by wavenumbers from five to 15. Next, all values of the envelope below a chosen threshold value are set to zero. This threshold value, τ^* , is chosen relative to the mean envelope and was chosen to be 3.5 m s^{-1} to create Figure 18b. This is done to ensure only “major features of the full envelope” are represented in the next step and produces the clipped RWT envelope seen in Figure 18b (GW13).

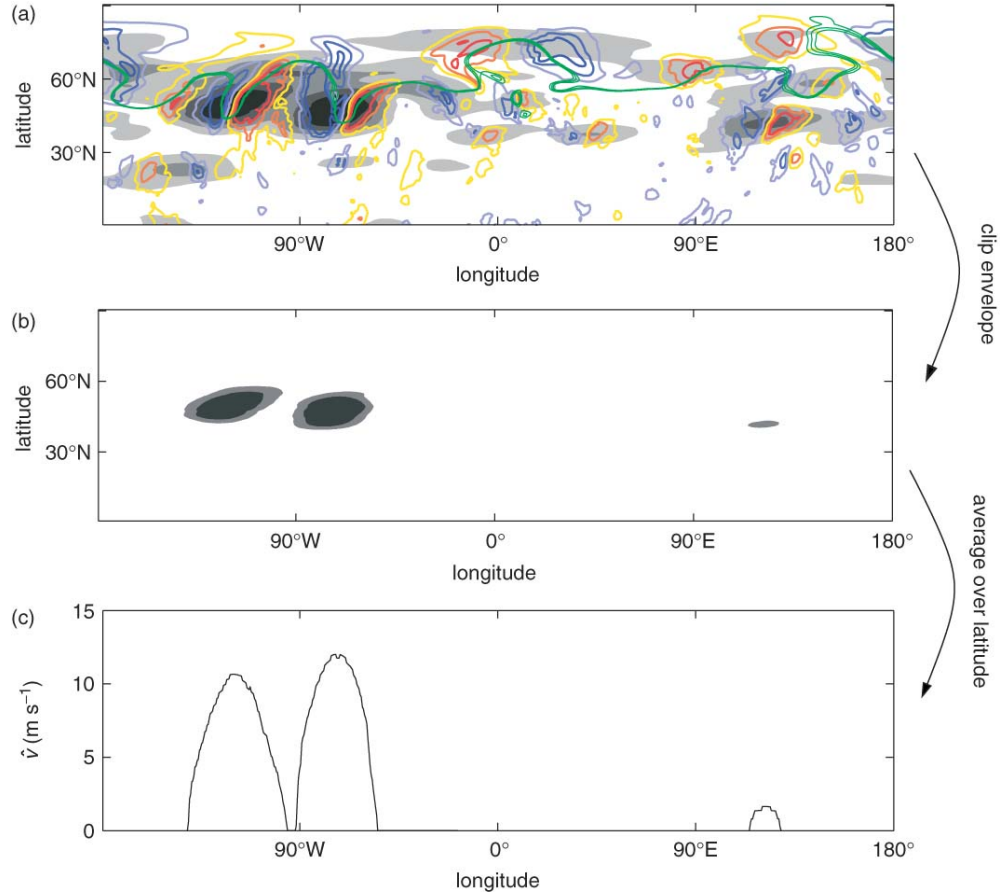


Figure 18. RWT analysis on the 250 hPa pressure level for 0000 UTC 7 Aug 2002. (a) Meridional wind v [$\pm 10, \pm 20, \pm 30$] m s^{-1} . In the color version warm colors correspond to positive values of v and cold color contours correspond to negative values of v . The solid green line is an isoline of geopotential ($\Phi = 10^5 \text{ m}^2 \text{ s}^{-2}$). (b) Clipped envelope E with the same shading convention as in (a). (c) The field $O(\lambda)$, which is a latitudinal average of E (from Glatt and Wirth 2013).

This “clipping parameter” was shown to be critical as its value determined whether or not RWT objects would remain coherent or be broken into individual objects. Once this process is complete and the feature is identified, properties of the RWT, including starting and ending longitudes, lifetime, and mean amplitude, are extracted from the RWT object. These extrapolated properties of the RWT are likewise sensitive to τ^* , as indicated in Figure 19, which shows a sensitivity analysis between the clipping parameter and (a) longitudinal extent and duration, (b) mean amplitude, and (c) RWT starting and ending longitudes (GW13).

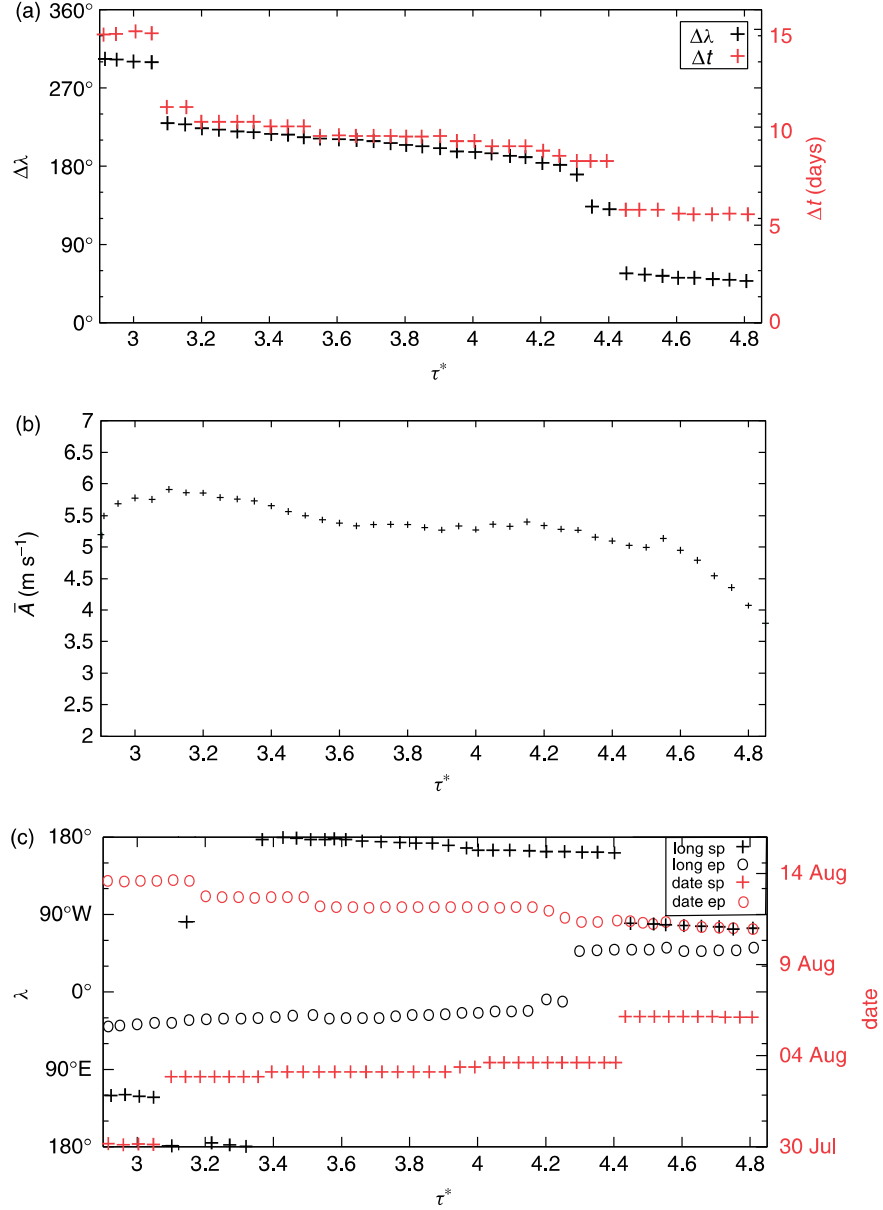


Figure 19. Dependence of various object properties on the clipping parameter τ^* (stepwidth $\Delta\tau^* = 0.05$): (a) $\Delta\lambda$ and Δt ; (b) \bar{A} , (c) sp, ep; “long” denotes the longitudinal component, “date” the temporal component (from Glatt and Wirth 2013).

Clipping was done to highlight the major features of the RWT and ensure these features have a minimal zonal signature in preparation for meridional averaging from 20°N to 80°N. GW13 note that without clipping, a feature that had relatively weak amplitudes, but whose signature was spread over a significant meridional expanse, may

still yield a significant signal once averaged over latitude. This averaging produces a one-dimensional value $O(\lambda)$ that characterizes the meridional wind structure of the RWT. Concatenating several days of this analysis yields $O(\lambda, t)$, which can be displayed as in the Hovmöller diagram in Figure 20 showing an eastward propagating RWT object.

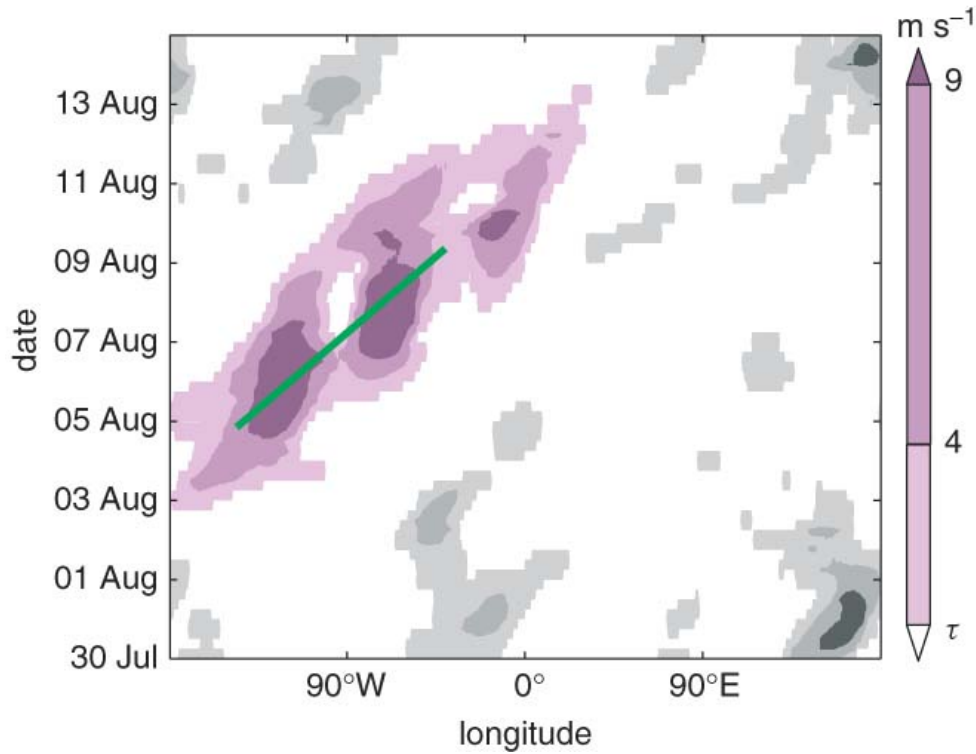


Figure 20. Hovmöller diagram of $O(\lambda, t)$ (shading, in m s^{-1}) on the 250 hPa surface for an episode in summer 2002. The straight green line indicates the main inertial axis (after GW13).

GW13 applied their objective identification method to the ERA-40 dataset from September 1957 through August 2002. They identified 2340 (606) RWTs with a minimum life span of four (nine) days. Subsequent to this, they applied their methodology to the ERA-Interim dataset from Jan 1979 through May 2013. This analysis yielded 2054 (550) RWTs with a minimum life span of four (nine) days. The two climatologies will be examined and compared in more detail in Chapter III.

The longitude of initiation and decay, starting and ending time, and length of duration of each RWT within the ERA-Interim derived climatology are used to conduct

the analysis presented in this thesis. These attributes are used to identify RWTs meeting predetermined criteria, and to conduct a subjective analysis to determine the relative frequency of RWT excitation due to each of the previously described triggers.

B. DIABATIC ROSSBY VORTEX CLIMATOLOGY

In 2013, BW13 created a tracking methodology for DRVs. When applied to an operational ECMWF analysis, they were able to assemble a climatology of DRVs across the Northern Hemisphere. This was done for the period 2001–2010 and showed variability in DRV frequency between the North Atlantic and North Pacific.

The BW13 tracking algorithm identified DRVs using six criteria. First, they identified SLP minima. Next, they ensured each region of minimum SLP had an 850 hPa PV value above an arbitrary threshold of 0.8 PVU. They then used 950 hPa potential temperature values to determine the baroclinicity of regions downstream of each SLP minimum and set a minimum threshold. Fourth, each area of interest had to propagate a minimum of 11.6 m s^{-1} or it was rejected. Next, 850 hPa relative humidity in the area surrounding the SLP minimum was used to exclude members with insufficient moisture. Finally, members with sufficient upper-level forcing that would develop through Type-B cyclogenesis were excluded.

The results of their analysis yielded 431 (809) DRVs over the North Atlantic (North Pacific). The DRV climatology provides latitude and longitude reports of identified DRVs every six hours. It also includes minimum SLP readings at each time step. These positions, along with their corresponding dates, were used to corroborate the existence of DRVs identified as RWT triggers in this study.

The BW13 climatology showed that DRVs form preferentially over the North Atlantic and Pacific during summer months. Our RWT analysis was conducted for September and October, during which a total of roughly 90 (140) DRVs formed over the North Atlantic (North Pacific) ocean during the years 2001–2010 (BW13). Of these DRVs, a larger percentage deepened explosively over the Pacific (BW13). Through the course of the RWT subjective analysis, this climatology is used to support the conclusion of a DRV associated with RWT triggering.

C. METHOD OF SUBJECTIVE ROSSBY WAVE TRAIN ANALYSIS

Given this research is intended to provide some insight into RWT behavior, the researchers sought to identify a subset of RWTs whose triggers would be representative of those likely to be sampled over eastern North America and the western North Atlantic, and that terminate and potentially cause sensible weather impacts over Europe. In addition, longer-lived RWTs triggered elsewhere in the world and terminating over Europe also will be examined.

1. Defining a Subset for Analysis

Due to the large number of RWTs identified in the ERA-Interim dataset, it was necessary to define parameters to truncate the dataset to a size commensurate with the scope of this research. To begin, the variables of interest for each RWT were the starting and ending longitude, initiation date, and duration. To ensure the RWT subset only included meaningful members, we first truncated all RWTs of duration 48 hours or less. Subsequently, RWTs of slightly longer durations that were omitted after initial analysis either did not indicate the presence of a RWT, or did not show an identifiable triggering mechanism.

Second, all RWTs that were not initiated in September or October were removed. This was done because GW13 indicated the greatest number of RWTs terminate over Europe in the fall. The dataset was further trimmed to only include the years 2004 to 2010. This was done because of the limitations of the DRV climatology and data availability. Finally, only RWTs with ending longitudes over Europe were retained. For the purposes of this research this was defined as 15°W to 30°E longitude. The resulting RWT subset contained 59 members with initiation longitudes varying globally and durations between two and 21 days. A further 21 RWTs were excluded from analysis due to factors including insufficient zonal extent, unavailable data, and inconclusive dynamic features. The 38 RWTs included for analysis are listed in Table 1. Each RWT was assigned an index of its original location within the dataset and is listed with its attributes used for analysis.

Index	Start Longitude (°W)	Starting Date	End Longitude (°W)	Ending Date	Duration (h)
6312	-12.48	2004091300	26.235	2004091700	108
6321	128.37	2004091412	11.655	2004092700	312
6330	150.75	2004100600	5.19	2004101600	252
6334	-69.525	2004101700	19.89	2004102500	204
6339	-53.265	2004102500	-7.665	2004110200	204
6556	-41.94	2005090112	-11.655	2005090400	72
6573	-32.04	2005092412	-9.33	2005092612	60
6577	-125.865	2005092712	-2.43	2005100300	144
6586	-30.645	2005101100	-9.345	2005101812	192
6595	-173.145	2005102000	-3.585	2005102800	204
6599	-79.5	2005102900	-2.79	2005110200	108
6812	-53.835	2006090112	12.225	2006090512	108
6819	-48.405	2006091212	-14.58	2006091500	72
6824	-108	2006091700	-9.465	2006092412	192
6826	166.815	2006092500	-12.75	2006100300	204
6836	-172.5	2006100700	-8.4	2006101812	288
6843	-151.44	2006102000	9.315	2006103012	264
6848	-106.44	2006103000	-12.405	2006110312	120
7078	-115.215	2007091300	4.275	2007091800	132
7091	-86.25	2007092800	-10.11	2007100212	120
7095	-39.96	2007100312	9.675	2007100800	120
7099	164.73	2007100300	-10.665	2007101312	264
7304	-39.3	2008090400	7.98	2008090712	96
7310	-18.855	2008091100	-10.11	2008091312	72
7316	-20.565	2008091612	-7.425	2008092112	132
7324	-19.83	2008100200	11.22	2008100400	60
7326	-53.895	2008100400	8.04	2008100600	60
7331	-146.28	2008100912	10.755	2008101700	192
7536	-40.485	2009090700	26.385	2009090900	60
7544	-92.22	2009091712	-7.35	2009092112	108
7557	-33.045	2009101212	7.92	2009101412	60
7567	-83.505	2009102312	11.79	2009102712	108
7571	-135.255	2009102500	9.045	2009110212	216
7783	-74.235	2010092012	-9.54	2010092600	144
7797	-3.75	2010101900	28.47	2010102100	60
7801	-98.085	2010102012	16.815	2010102700	168
7803	-69.345	2010102700	21.555	2010103000	84
7805	123.195	2010102500	8.64	2010110212	216

Table 1. RWTs chosen for further analysis of their triggering mechanisms.

2. Subjective Analysis Methodology

Each of the RWTs in Table 1 was examined systematically using a Global Forecast System (GFS) analysis archive of figures depicting the dynamic tropopause (DT), 250 hPa irrotational wind (IW), and sea level pressure (SLP). All GFS analysis archive plots presented in this research are provided courtesy of Dr. Heather Archambault. RWTs are referred to by their index within the original ERA-Interim derived RWT climatology. Additional descriptions are given of the dynamical information to be gleaned from each type of figure regarding specific RWT triggering mechanism. The example plots presented in Figures 21, 22, and 23 are part of a larger analysis of RWT triggering by the ET of a TC. This example will be examined more fully later in this chapter and in Chapter IV. An example DT plot is presented in Figure 21.

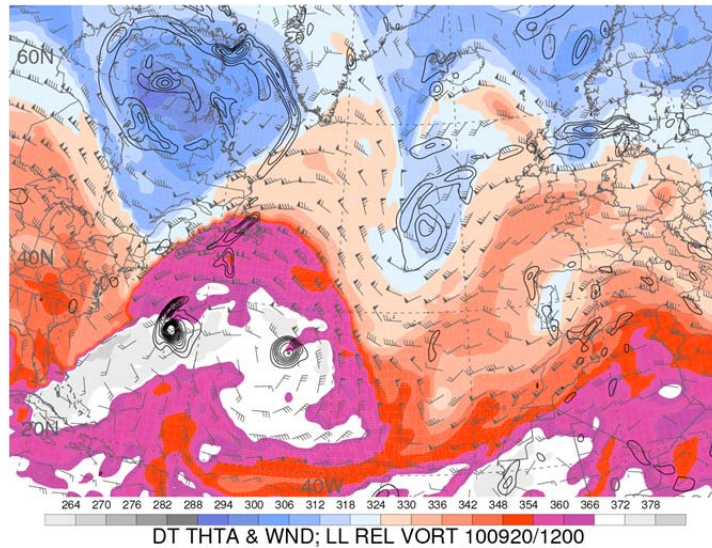


Figure 21. Potential temperature (K) and wind barbs (long barb = 10 kts and a flag = 50 kts) on the dynamic tropopause, which is defined as the 1.5 PVU surface. Lower-level relative vorticity averaged over the 925–850 hPa layer is indicated by black contours (every $5 \times 10^{-5} \text{ s}^{-1}$; unpublished figure provided by H. Archambault).

Each RWT analysis begins with an examination of the DT. Regions of lower (higher) potential temperature indicate upper-level ridges (troughs) and form the basis of identifying the RWT in question. Once identified, the RWT is tracked to an approximate

time of initiation. At this point the surrounding features are analyzed to determine the RWT trigger. Regions of strong lower-level relative vorticity easily identify tropical cyclones. TPVs appear as regions of very low potential temperature (gray shading on the DT map) poleward of the waveguide. The lower-level vorticity signature of DRVs is identifiable and allows for a positional comparison to the BW13 DRV climatology. ECs appear as regions of lower potential temperature with lower-level vorticity, but the diagnosis of an EC must be confirmed on additional plots. Areas of high potential temperature that move rapidly poleward just downstream of ECs evidence WCBs. None of these criteria alone can provide a subjective determination of the RWT trigger, but they assist in guiding further analysis and excluding some mechanisms from consideration. After an initial analysis, IW plots (Figure 22) are used for further dynamical insight into the RWT triggering mechanisms.

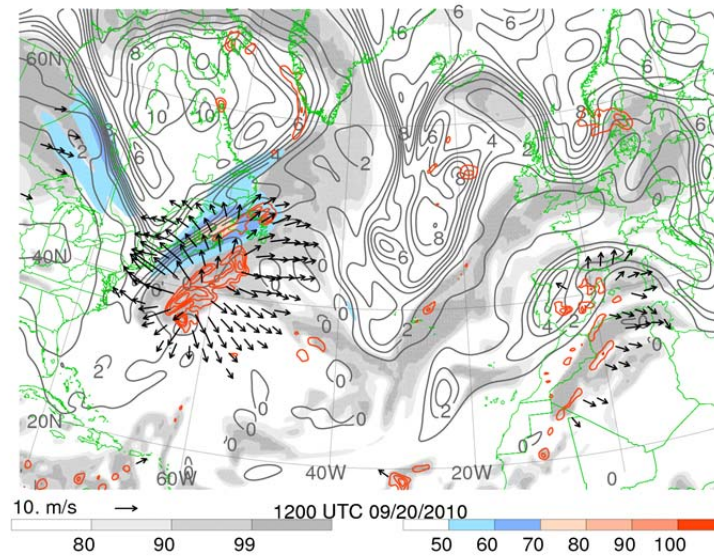


Figure 22. The irrotational wind (IW) figure showing 300–200 hPa averaged IW with vectors (values $\geq 5 \text{ m s}^{-1}$), 250 hPa wind speeds with colored contours (m s^{-1}), 250 hPa potential vorticity with gray contours (every 1 PVU), 250 hPa relative humidity with gray shading (%), 600–400 hPa averaged ascent with red contours (every $5 \times 10^{-3} \text{ hPa s}^{-1}$; unpublished figure provided by H. Archambault).

Following an initial examination of the DT, further analysis of the upper-level IW shows features impinging on the waveguide. Rising motion and upper-level divergent

outflow resulting from WCBs, ET, and DRV appears similar on IW plots once the feature has begun to interact with the waveguide. TPVs and ECs also appear similarly as regions of high PV, although TPVs are not initially accompanied by rising motion or divergent outflow. Plots of IW are useful in excluding those triggers that perturb the waveguide with negative PV anomalies at upper-levels (WCB, DRV, ET) as they can show a lack of upper-level divergent outflow in the presence of RWT triggering. Following examination of the IW, further analysis of surface features is accomplished through the examination of sea level pressure plots similar to the one presented in Figure 23.

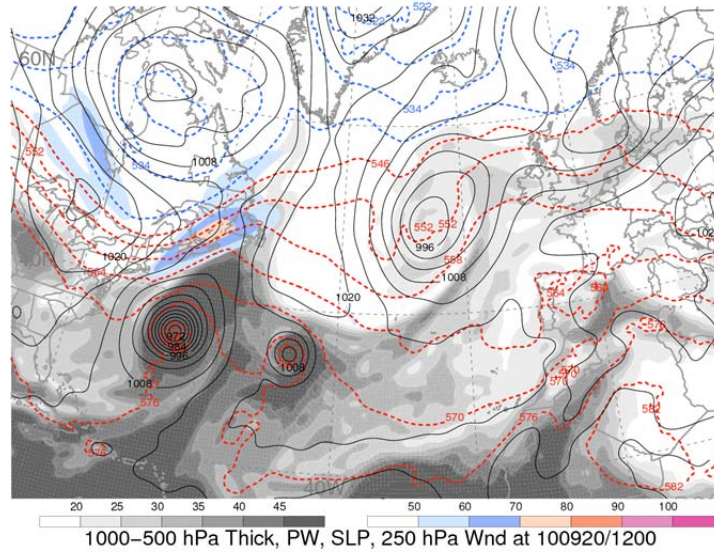


Figure 23. Sea level pressure (black contour, hPa) figure where gray shading indicates total column precipitable water (mm), color shading indicates 250 hPa wind speeds (m s^{-1}), dashed contours are 1000–500 hPa thickness labeled every 6 dam, and solid contours are SLP every 4 hPa (unpublished figure provided by H. Archambault).

To differentiate between TPVs and ECs, analysis of SLP will indicate the presence of an EC with closed contours of surface pressure. TPVs do not show this feature on SLP plots. ETs also appear as a region of closed SLP contours, typically with a lower central pressure. Additionally, SLP plots also indicate regions of high total column precipitable water associated with WCBs, ETs, and DRV.

Secondary to the three primary GFS analysis archive plots, Hovmöller plots are also useful in observing the initiation, downstream development, and termination of RWTs. Figure 24 shows the lifecycle of a RWT (number 6824), and an analysis presented later in this chapter will show this RWT is triggered by a WCB associated with an EC at 1200 UTC 18 Sep 2006. The Hovmöller plot is created with 300 hPa meridional wind anomalies from the National Centers for Environmental Prediction (NCEP) Reanalysis data averaged over a range of latitudes. The range of latitudes varies in order to best capture the features of the RWT. Figure 24 clearly shows the ridge-trough pattern associated with a RWT at 0000 UTC 19 Sep 2006, as indicated by the alternating positive (warmer colors) and negative (cooler colors) meridional wind anomalies. As time increases downward, the eastward propagation of the RWT is evident until decay near 1200 UTC 24 Sep 2006.

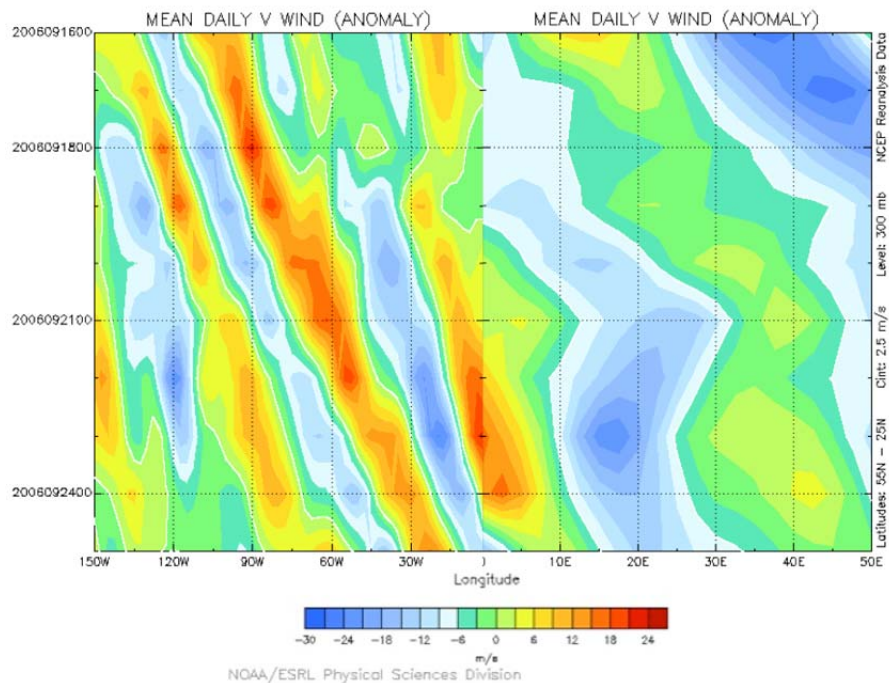


Figure 24. Hovmöller diagram of the lifecycle of RWT number 6824 using 300 hPa meridional wind anomalies from NCEP Reanalysis data averaged between 25°–55°N. Wind speeds are indicated by color where warmer colors indicate positive values and cooler colors indicate negative values. The plot begins at 0000 UTC 16 Sep 2006 (top) and ends at 0000 UTC 25 Sep 2006 (bottom) (unpublished figure provided by the National Oceanic and Atmospheric Administration [NOAA]/Earth System Research Laboratory [ESRL] Physical Sciences Division).

With these figures, and the RWT attributes in Table 1, this research is able to localize and identify the triggering mechanism for each RWT. In addition to RWT triggers, downstream development resulting from upper-level forcing of the RWT is also noted and will be examined in detail with a RWT lifecycle analysis in Chapter IV. Examples of RWTs triggered by each of the four mechanisms (TPV, WCB, DRV, ET) are presented, with emphasis on using the available figures to differentiate between triggers.

a. Tropopause Polar Vortex

On a DT map, TPVs appear as regions of low potential temperature poleward of the waveguide. Their equatorward movement results in a corresponding deformation of the waveguide and the formation of a trough. The high PV associated with TPVs and their lack of upper-level divergent outflow and upper-level relative humidity are clearly evident on IW charts. The SLP maps depict TPVs as regions of anomalous low thickness poleward of the waveguide, but are more useful in excluding WCBs, ET, and DRVs as candidates for RWT triggering by showing the absence of their indicators. For all cases (TPV, WCB, DRV, ET), the BW13 DRV climatology and National Hurricane Center (NHC) tropical cyclone best-track data are consulted to exclude or implicate suspected features in RWT triggering.

RWT number 7805 was initiated near 125°E at 0000 UTC 25 Oct 2010. Figure 25 shows a TPV of interest for five days leading up to the triggering of RWT number 7805. The TPV begins near 75°N 90°E on 20 October 2010 as indicated by the red circle in Figure 25a. This feature can be visually tracked for five days until 0000 UTC 25 Oct 2010 (Figure 25f) when the initial perturbation of the waveguide and RWT initiation takes place. Once the TPV has been identified, the next step in assessing its role in RWT initiation is to examine the waveguide near the TPV before and during the RWT starting time.

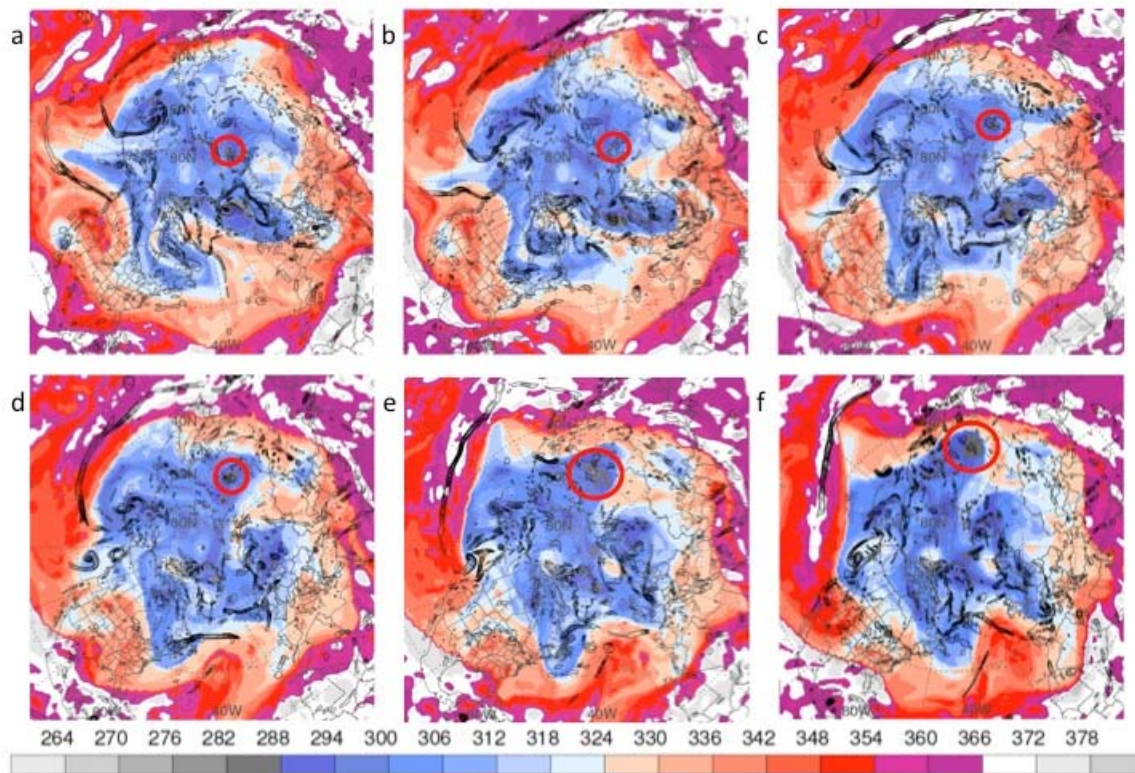


Figure 25. Same as for Figure 21 except 0000 UTC for (a) 20 Oct 2010, (b) 21 Oct 2010, (c) 22 Oct 2010, (d) 23 Oct 2010, (e) 24 Oct 2010, and (f) 25 Oct 2010. The red circle marks the location of the TPV at each time (unpublished figure provided by H. Archambault).

Forty-eight hours prior to RWT initiation, a closer examination of the DT at 0000 UTC 23 Oct 2010 (Figure 26) shows a relatively zonal waveguide (green line) equatorward of the TPV (red circle). At this point, it is necessary to examine the southern side of the waveguide for perturbations associated with the other three types of RWT triggers. Because WCBs, DRVs, and ET events are all associated with negative PV anomalies and high potential temperature below the tropopause, a plot of upper-level PV can confirm the presence of a positive PV anomaly associated with the TPV as well as any negative PV anomalies that may contribute to RWT formation.

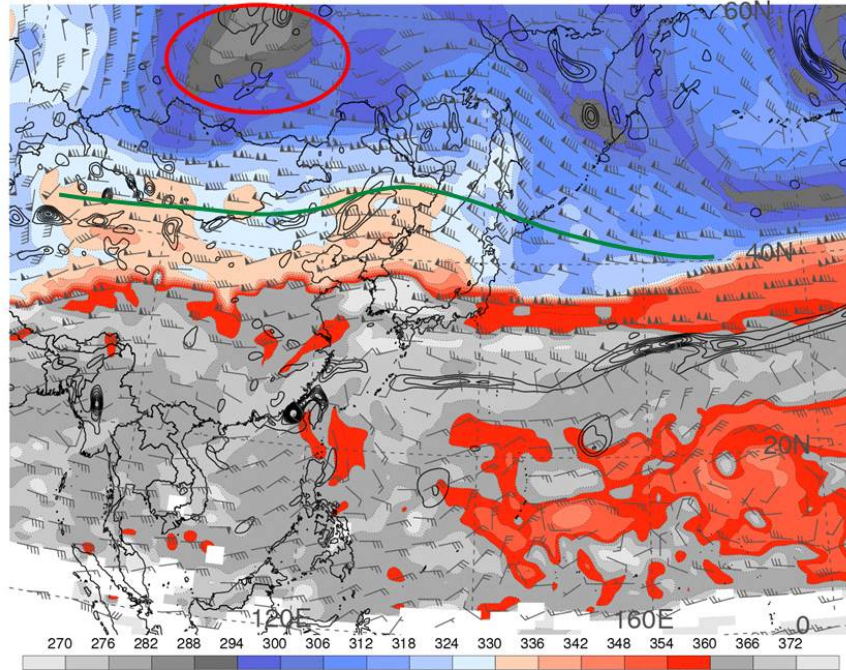


Figure 26. Same as for Figure 21, except for 0000 UTC 23 Oct 2010 (unpublished figure provided by H. Archambault).

Figure 27 shows the upper-level divergent outflow defined by the IW for the same time as Figure 26. The region of high PV associated with the TPV, between 6–8 PVU, is highlighted (red circle). This helps confirm the presence of a TPV impinging on the mostly zonal flow. Near 140°E, there is a discontinuity in the jet as it moves from near 50°N towards 40°N. Although it appears there is a negative PV anomaly on the equatorward side of the jet (green circle) impinging on it, this region is roughly 2 PVU, or the same value as the DT. This region is an area of weak PV gradient, not a PV anomaly impacting the jet.

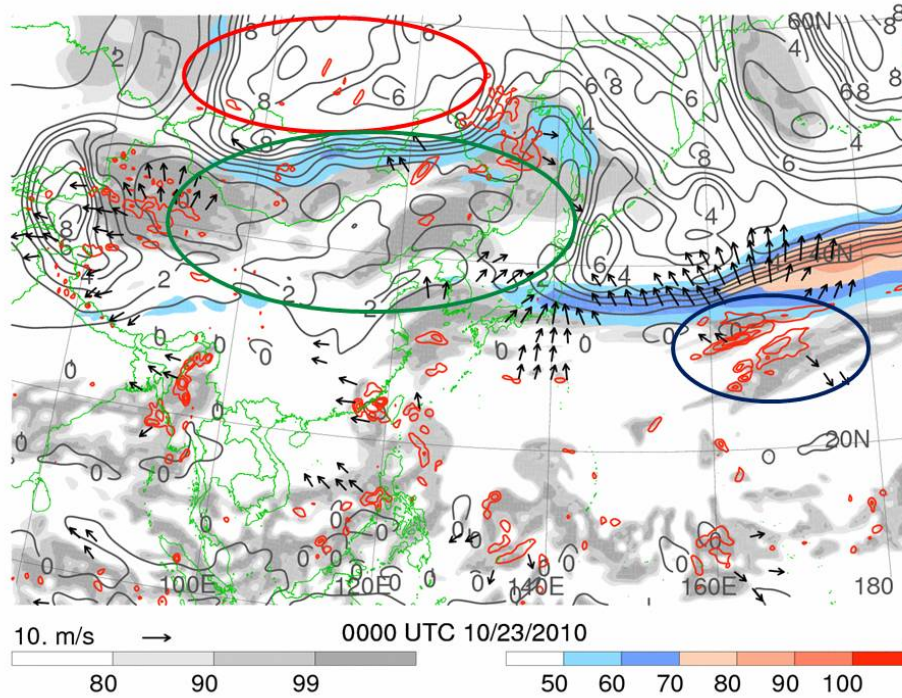


Figure 27. Same as for Figure 22, except for 0000 UTC 23 Oct 2010 (unpublished figure provided by H. Archambault).

The 250 hPa IW is used to identify upper-level divergent outflow. This outflow has the potential to impinge on the zonal flow through the advection of low-PV air as described in Figure 15. In Figure 27 there is an area of upward motion (blue circle) and divergent outflow impacting the jet downstream of the discontinuity previously discussed. This area acts to strengthen the jet similar to the low PV advection described in Figure 15 but is not associated with a significant negative PV anomaly resulting from one of the other three RWT triggers. This region is likely a small diabatically driven area of convection. Additional examination of an SLP plot (not shown) reveals no discernable SLP minimum associated with this feature. Subsequent plots will show, however, that this feature propagates eastward and does not affect the formation of the RWT.

Now that the TPV has been identified on the IW plot, its impact on the waveguide over time can be tracked. Beginning at 0000 UTC 25 Oct 2010 (Figure 28a) the TPV (red circle) has perturbed the waveguide equatorward and formed the beginning of the familiar trough-ridge pattern associated with Rossby waves. The formation of this trough

(black dashed line) lends upper-level support to the region denoted by the blue circle and forces significant diabatic amplification of the ridge (black solid line), further developing the RWT over the next 36 hours (Figure 28 b,c,d). The diabatic contribution to ridge building is indicated by the mid-level rising motion equatorward the ridge. Ridge building is further produced by the advection of upper-level lower PV air indicated by the divergent outflow vectors. After initiation, this RWT lasted until 1200 UTC 02 Nov 2010, or approximately nine days. In that time, the RWT propagated from 123°E to 8°E, or roughly 245° of longitude.

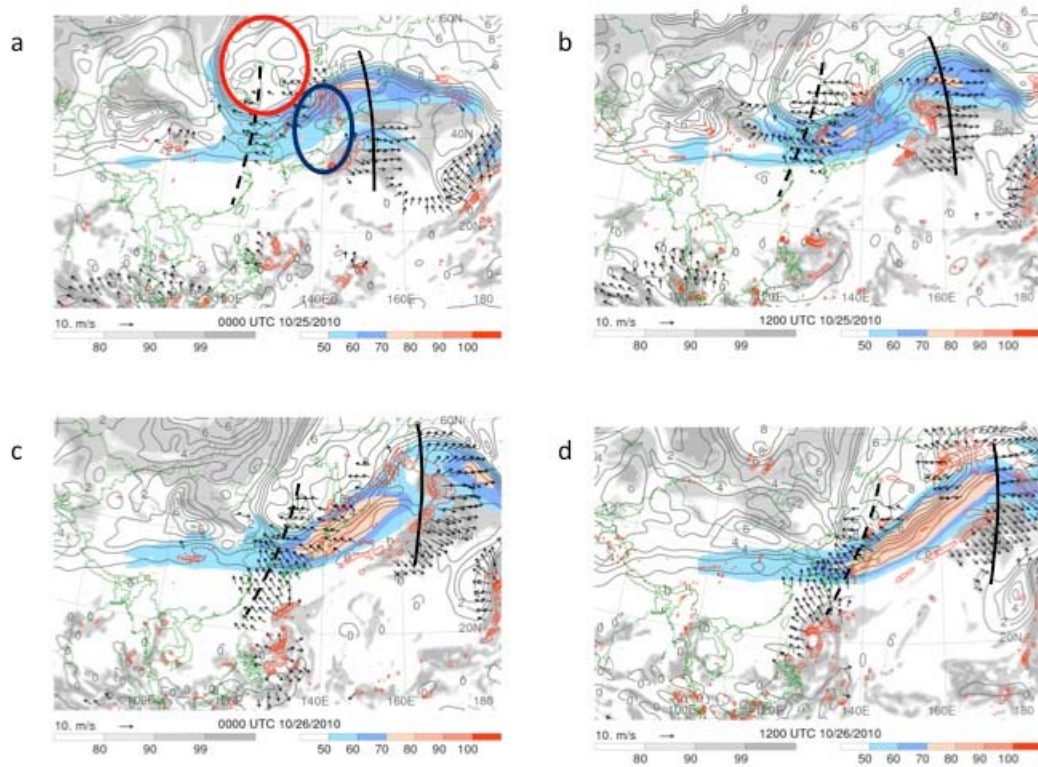


Figure 28. Same as with Figure 22, except for (a) 0000 UTC 25 Oct 2010, (b) 1200 UTC 25 Oct 2010, (c) 0000 UTC 26 Oct 2010, and (d) 1200 UTC 26 Oct 2010 (unpublished figure provided by H. Archambault).

b. Warm Conveyor Belt

On a DT map, regions of high potential temperature extending poleward towards the waveguide identify WCBs. Low-level positive vorticity identifies the cyclonic circulation of the disturbance as well as frontal boundaries associated with the EC. The IW maps indicate rising motion, upper-level divergent outflow, and elevated upper-level humidity. These three indicators are associated with the ascending air stream of a WCB. The SLP maps show closed contours representing the EC, and thickness gradients indicating baroclinic zones, frontal boundaries, and the location of the warm sector of the EC. Additionally, total column precipitable water supports tracking the warm moist advection associated with the WCB.

According to the RWT climatology, RWT number 6824 was triggered near 100°W at 0000 UTC 17 Sep 2006. Figure 29a shows a DT map of the region of RWT initiation at 0000 UTC 14 Sep 2006. At this time, there is a large ridge over the eastern Pacific and a weaker downstream trough over western North America. Twenty-four hours later (Figure 29b) the trough begins to deepen and becomes a cutoff low. By 0000 UTC 17 Sep 2006, there is no evidence of RWT triggering, but there is a region of lower-level vorticity (green circle, Figure 29d) downstream of the cutoff low. This area of upper-level positive vorticity advection (PVA) is favorable for cyclogenesis and the formation of an EC and associated WCB.

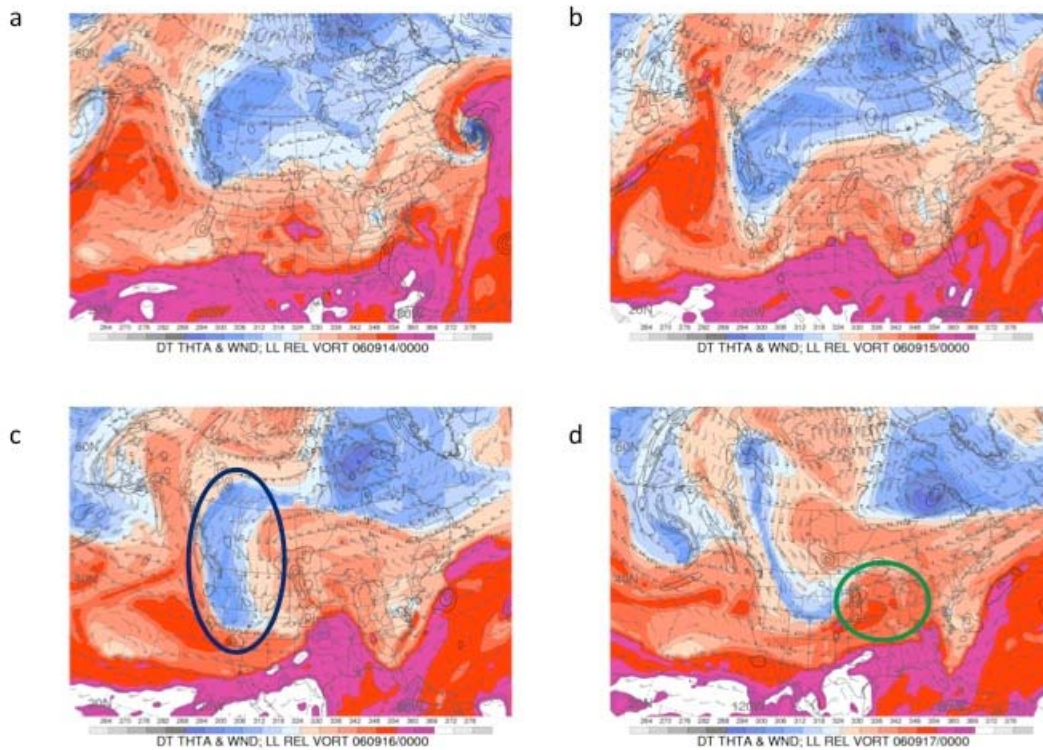


Figure 29. Same as for Figure 21, except for (a) 0000 UTC 14 Sep 2006, (b) 0000 UTC 15 Sep 2006, (c) 0000 UTC 16 Sep 2006, and (d) 0000 UTC 17 Sep 2006 (unpublished figure provided by H. Archambault).

Although 0000 UTC 17 Oct 2006 is the RWT initiation time indicated by the climatology used, variation in meridional winds suggest forcing from the WCB and initiation of RWT number 6824 does not occur until 36 hours later at 1200 UTC 18 Sep 2006. Figure 30a,b shows clear indications of a WCB (green circle) with high potential temperature and meridional movement at 1200 UTC 17 Oct 2006 and 0000 UTC 18 Oct 2006. This tongue of high potential temperature air extending poleward rises and releases latent heat as indicated by the red contours in Figure 31b. It continues to build a ridge near 80°W (Figure 30c,d), with a deepening lee trough (black dashed line) near 90°W, which indicates the formation of a RWT.

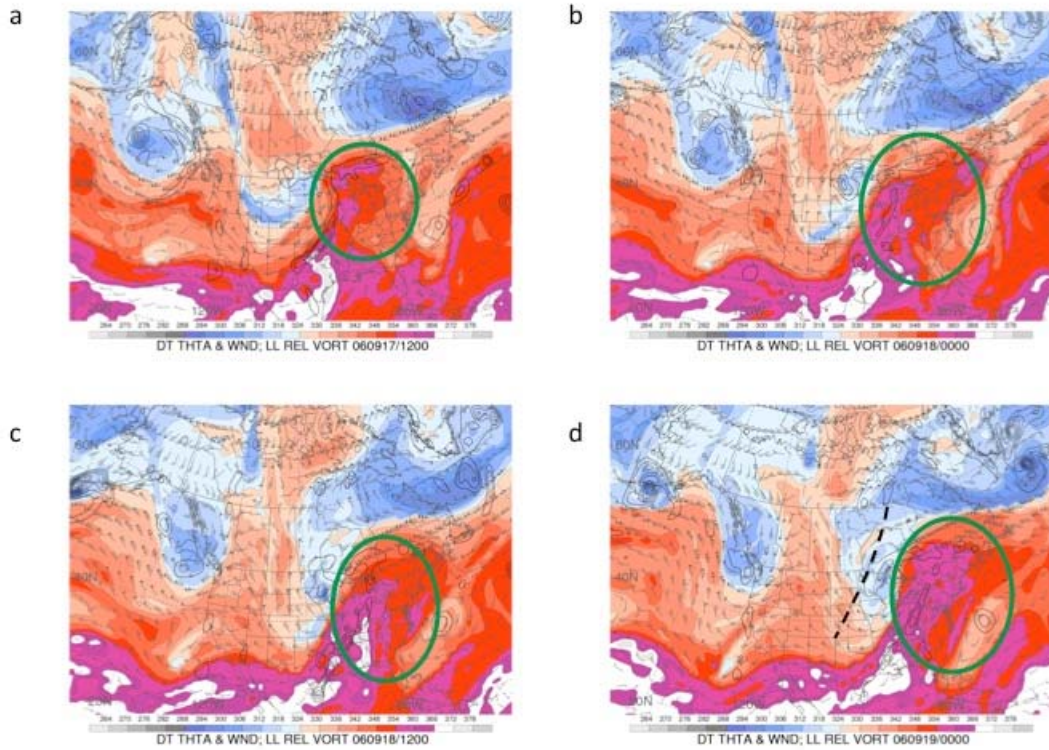


Figure 30. Same as for Figure 21, except for (a) 1200 UTC 17 Sep 2006, (b) 0000 UTC 18 Sep 2006, (c) 1200 UTC 18 Sep 2006, and (d) 0000 UTC 19 Oct 2006 (unpublished figure provided by H. Archambault).

To support the conclusion that RWT triggering is the result of WCB forcing it is helpful to examine plots of total precipitable water and upper-level relative humidity. Figure 31a shows a region of higher precipitable water extending north across the central U.S. (red circle). This area also highlights the SLP minimum and thickness gradients associated with the EC of interest. Figure 31b, however, reveals this moisture has not sufficiently extended into the upper-levels by 1200 UTC 15 Oct 2006. By the time the upstream low has cut off at 1200 UTC 16 Oct 2006, the upper-level support it provides has helped the ascending WCB increase the 250 hPa relative humidity over the central U.S. (Figure 31d, green circle). This is due to the intense rising motion as warm moist air from the south is forced poleward over isentropic surfaces.

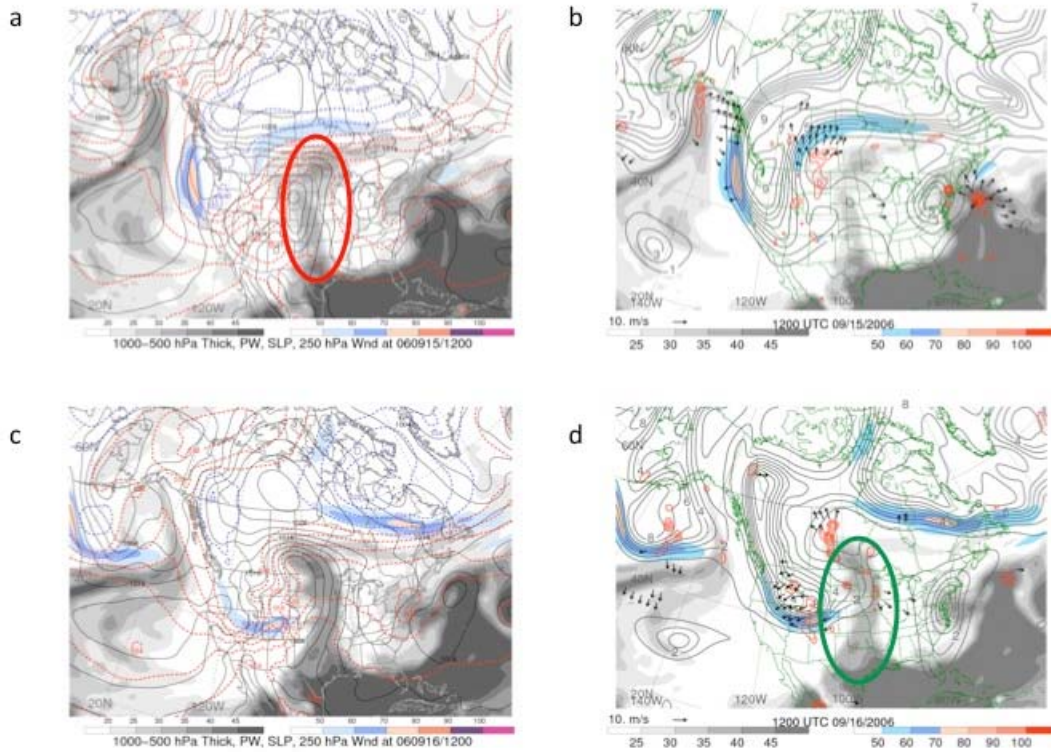


Figure 31. Same as for Figure 23, except for (a) 1200 UTC 15 Sep 2006 and (c) 1200 UTC 16 Sep 2006. Same as for Figure 22 at (b) 1200 UTC 15 Sep 2006 and (d) 1200 UTC 16 Sep 2006 (unpublished figure provided by H. Archambault).

With the overall column moistened sufficiently, LHR associated with the WCB results in diabatic ridging along the waveguide (Figure 32a, green line). As it does, the jet intensifies at 0000 UTC 19 Oct 2006 indicated by the warmer color shading depicted in Figure 32c. This is due to upper-level divergent outflow (red circle). This begins the formation of the first ridge (solid black line) and trough (dashed black line) couplet of the RWT, which intensify over the following 24 hours as indicated by Figure 32d.

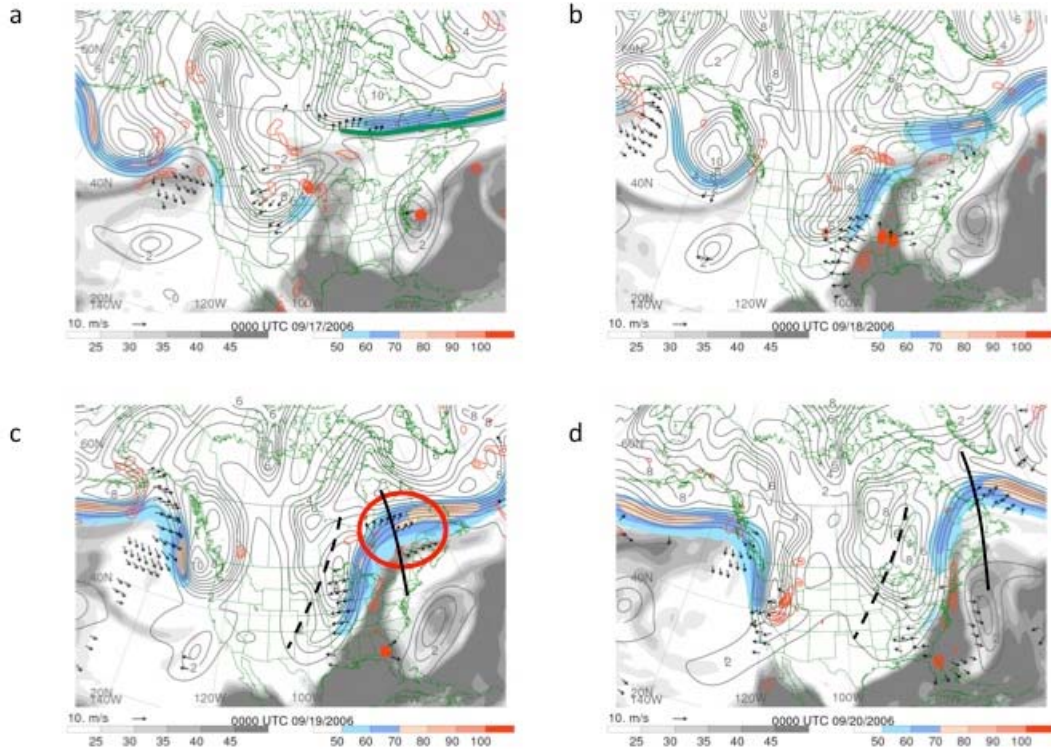


Figure 32. Same as for figure 22, except for (a) 0000 UTC 17 Sep 2006, (b) 0000 UTC 18 Sep 2006, (c) 0000 UTC 19 Sep 2006, and (d) 0000 UTC 20 Sep 2006 (unpublished figure provided by H. Archambault).

RWT formation due to WCB interaction with the waveguide is somewhat more difficult to subjectively identify than formation due to TPVs. Because of the need for upper-level support for Type-B cyclogenesis, there is some existing perturbation in the waveguide prior to the onset of the WCB. This perturbed waveguide presents challenges in determining causality when examining the ridge-trough formation. For definitive identification of the WCB it is easiest to first localize the EC by its lower-level vorticity signature and SLP minimum on the DT and SLP maps, respectively. The WCB can then be identified on the downstream side by its mid-level vertical velocity. Trajectory analyses could also be useful in defining the location of a WCB. This method was used by Madonna et al. (2014) to construct their WCB climatology. After initiation, this RWT

lasted until 1200 UTC 24 Sep 2006, or approximately six days. In that time it propagated from near 80°W to 9°E, or roughly 90° of longitude.

c. Diabatic Rossby Vortex

On a DT map, DRVs appear as areas of lower-level vorticity in a region of high potential temperature. The location of the suspected DRV on the DT map is first checked against the BW13 climatology to confirm the presence of a DRV. The maps of DT also show the presence of upper-level features in relation to the DRV. Although subjective, close proximity to upper-level support can preclude the assessment of the RWT being triggered by a DRV, especially if the suspected DRV does not appear in the BW13 climatology. IW maps show DRVs as areas of high moisture content and rising motion in regions of low PV. With little divergent outflow prior to interaction with upper-level features, as the DRV begins to receive upper-level support its divergent outflow increases and impacts the local jet. SLP maps depict DRVs as regions of low SLP with closed contours and high total column precipitable water. They may also show closed thickness contours due to the large amount of heating occurring.

RWT number 6826 was triggered near 165°E at 0000 UTC 25 Sep 2006. Because DRVs intensify and trigger RWT initiation devoid of upper-level forcing over moist baroclinic zones, diagnosis of a DRV must include analysis of upper-level PV, and lower-level moisture and vorticity. A DT plot at 1200 UTC 22 Oct 2006 identifies a region of lower-level positive relative vorticity as indicated by the red circle in Figure 33a. There is a weak upper-level trough (dashed line) upstream of the DRV that later will support the intensification of the DRV.

BW13 state that the area of lower-level vorticity indicative of a DRV can appear benign on weather maps. Significant intensification associated with DRVs most commonly occurs when the lower-level anomaly (the DRV) interacts with a pre-existing upper-level trough (as is the case here). Less commonly, a DRV can become a sufficiently deep feature to directly interact with a zonal waveguide (i.e. Type-A cyclogenesis). In both scenarios, a troposphere deep cyclone ensues allowing for the

mutual amplification of lower- and upper-level PV anomalies via both baroclinic and diabatic processes.

The feature of interest in Figure 33 contains significant moisture as indicated by the high total column precipitable water (gray shading) in Figure 33b and 33d. By 1200 UTC 23 Oct 2006, the upper-level divergent outflow of the DRV has begun to intensify the jet through the advection of low-PV. This is indicated in Figure 33d by the color shading. In addition, growing interactions between the upper and lower levels are helping to drive deepening of the upper-level trough and increase support for the development of the DRV, illustrating the mutual amplification of lower- and upper-level features discussed in the previous paragraph.

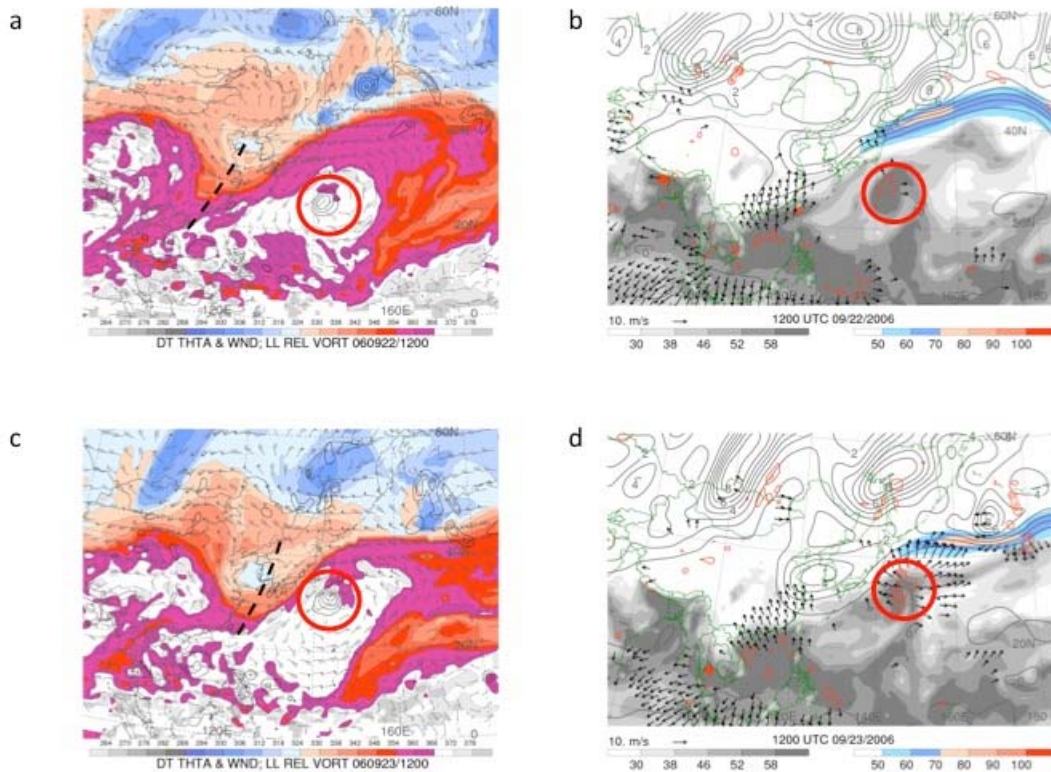


Figure 33. Same as for Figure 21, except for 1200 UTC at (a) 22 Sep 2006 and (c) 23 Sep 2006. Same as for Figure 22 at (b) 22 Sep 2006 and (d) 23 Sep 2006 (unpublished figure provided by H. Archambault).

By 1200 UTC 24 Oct 2006, the impact of the upper-level divergent outflow and diabatic ridging from the DRV has forced the downstream development of a trough, indicated by the dashed line in Figure 34a. Twelve hours later, which is the start time of RWT number 6826, the DRV is producing significant divergent outflow, as indicated by the black vectors in Figure 34b, and has created the ridge-trough pattern indicative of RWT formation. Moreover, the trough produced through downstream development is supporting development of a region of weak rising motion near 40°N 160°E, indicated by the green circle in Figure 25a. This upper-level support aids in the amplification of a follow-on ridge and the downstream development associated with the RWT. In addition to a subjective analysis, the objective climatology of BW13 confirms the existence of the DRV that is seen to trigger RWT number 6826. From the BW13 analysis, a DRV began at 0600 UTC 23 Oct 2006 near 30°N 141.6°E. Six hours later it propagated to 30.6°N 142.8°E, coinciding with the lower-level vorticity highlighted by the red circle in Figure 33a. While this DRV did not meet the criteria of a “bomb,” it did undergo significant intensification, reaching a SLP minimum of 963.88 hPa at 1200 UTC 26 Sep 2006 (BW13).

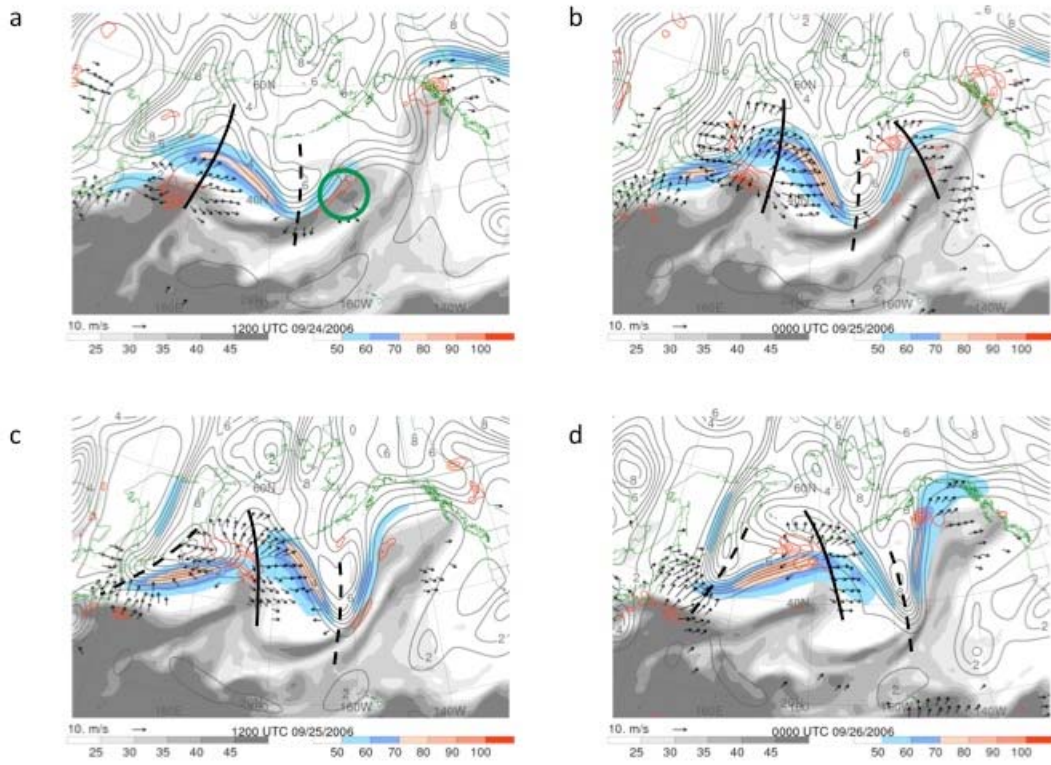


Figure 34. Same as for Figure 11, except for (a) 1200 UTC 24 Sep 2006, (b) 0000 UTC 25 Sep 2006, (c) 1200 UTC 25 Sep 2006, and (d) 0000 UTC 26 Sep 2006 (unpublished figure provided by H. Archambault).

d. Extratropical Transition

On a DT map, TCs appear as areas of intense lower-level vorticity in regions of high potential temperature. On IW maps, TCs are areas of intense rising motion and upper-level divergent outflow within regions of low PV and high upper-level relative humidity, similar to the features of a WCB. Distinguishing between the two requires comparing the location of the lower-level vorticity on the DT map to NHC best-track data. The closed contours of a TC are clearly evident on a SLP chart.

RWT number 7783 was triggered near 075°W at 1200 UTC 20 Sep 2010. Figure 35 depicts the track of Hurricane Igor from 8–21 Sep 2010. The storm begins moving poleward between 18 and 19 Sep 2010. After this, its northward velocity increases, and it is located at approximately 35°N 065°W at the time of RWT initiation.

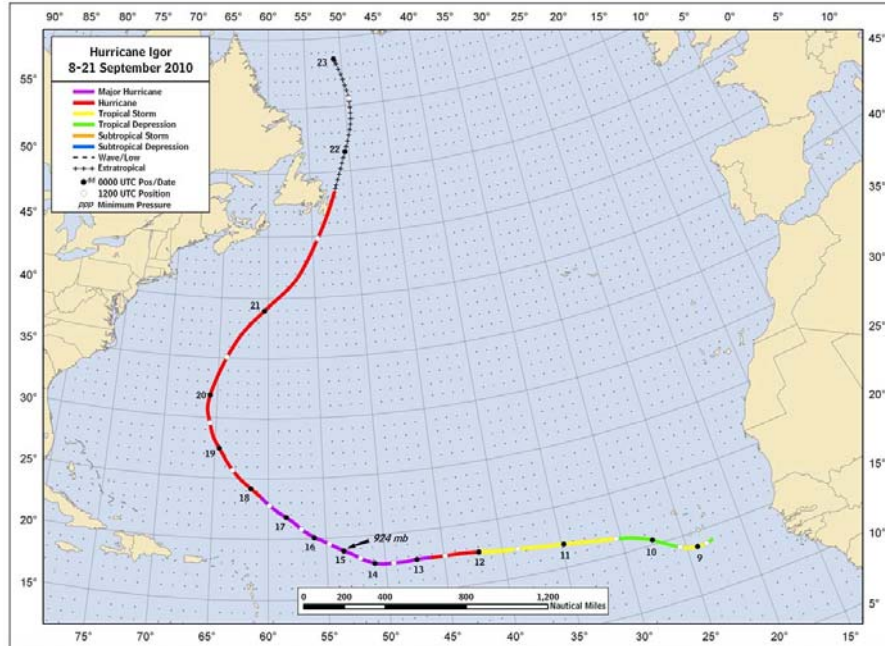


Figure 35. Best track positions for Hurricane Igor, 8–21 September 2010. Track during the extratropical stage is based partially on analyses from NOAA Ocean Prediction Center (from Pasch and Kimberlain 2011).

Of the four RWT triggering mechanisms, TCs are the easiest to identify on DT maps as regions of significant low-level cyclonic vorticity. Figure 36 shows an occluded EC, indicated by a green circle, poleward of Hurricane Igor, indicated by a red circle. The lower-level vorticity signature on the DT plot identifies the EC. Additional analysis of SLP plots (not shown) indicate closed SLP contours associated with the EC. As the EC completes its lifecycle, there exists a weak PV gradient and a relatively undefined waveguide between the two. As Igor undergoes ET, this PV gradient increases as the upper-level divergent outflow from Igor advects lower PV air poleward. The divergent outflow is indicated in Figure 37a and 37b by black vectors.

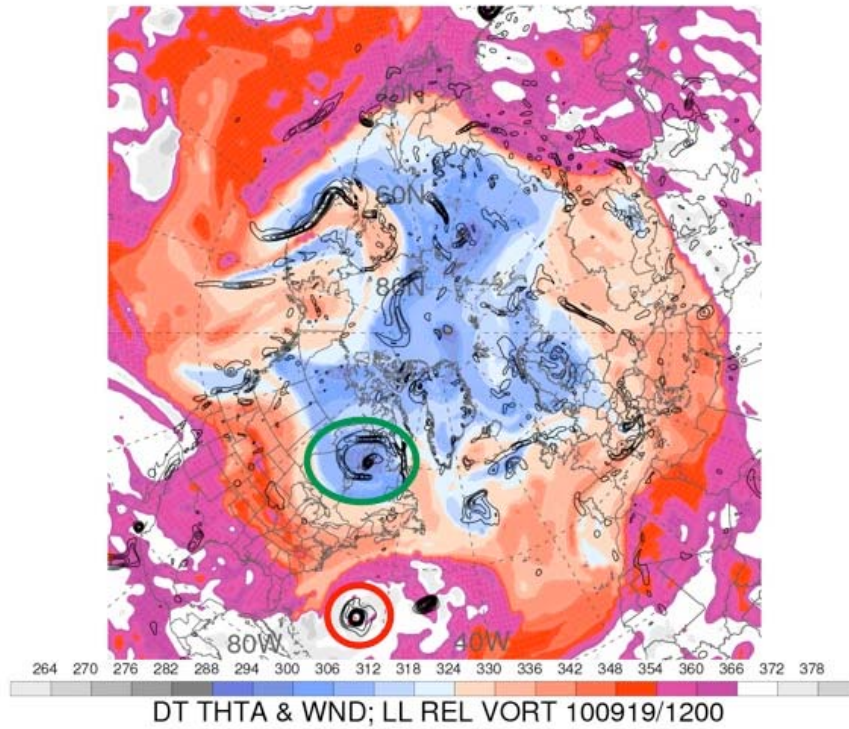


Figure 36. Same as for Figure 21, except for 1200 UTC 19 Sep 2010 (unpublished figure provided by H. Archambault).

Figure 37 shows the impact of the divergent outflow from Igor from 0000 to 0600 UTC 20 Sep 2010. Immediately poleward of the green line, between the lower-PV outflow from Igor and the higher PV remnants of the EC, the PV gradient strengthens. The increased gradient is necessary to provide a sufficiently strong waveguide for RWT triggering and propagation. An area of upper-level positive PV is also present downstream as indicated by the red circles in Figure 37. Initially this region is centered between 50° and 60°N but as the divergent outflow strengthens the waveguide, ridge building forces the waveguide near 60°W poleward. This elicits an equatorward response in the downstream region of positive PV. This will later become a trough as a result of Igor's ET.

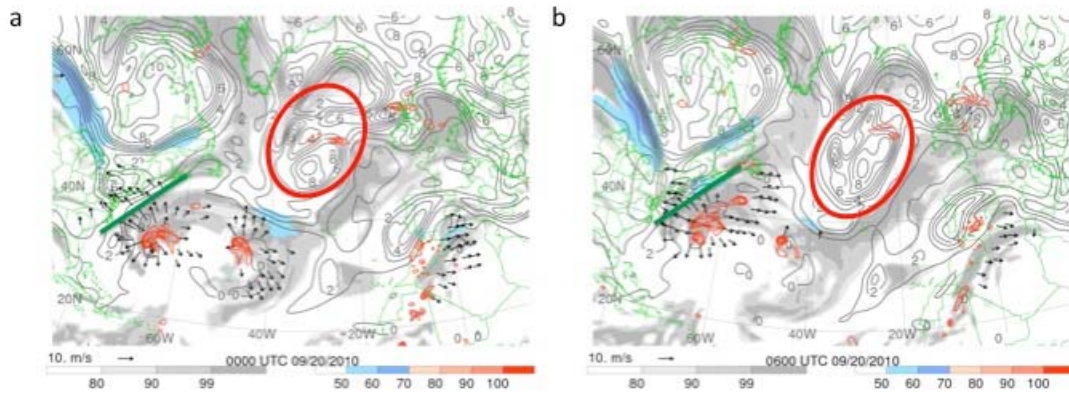


Figure 37. Same as for Figure 22, except for (a) 0000 UTC 20 Sep 2010 and (b) 0600 UTC 20 Sep 2010 (unpublished figure provided by H. Archambault).

At the time of initiation, 1200 UTC 20 Sep 2010 (Figure 38a), some key features of RWT triggering occur. First, the upper-level divergent outflow, buoyed by support from the upstream trough, has increased significantly. This outflow results in ridge building, indicated by the solid line in Figure 38a, and intensification of the nearby jet, further tightening the PV gradient defining the waveguide. Second, the ridge building has forced further deepening of the upstream trough, indicated by the dashed line, creating a region of upper-level PVA above the ET. Upper-level PVA supports further development of the system, prompting upper-level divergence and intensification of the divergent outflow through a positive feedback mechanism typical of a growing extratropical system.

According to the NHC Tropical Cyclone Report for this system, Igor transitioned to an extratropical cyclone at 1800 UTC 21 Sep 2010, 30 hours after the initiation of RWT number 7783 (Pasch and Kimberlain 2011). The NHC report also shows increasing SLP minimums for Igor beginning at 1800 UTC 18 Sep 2010. This indicates Igor was in the transformation stage prior to RWT triggering (Klein et al. 2000). After the time of RWT triggering, the central pressure of Igor remained steady at 960 hPa for 18 hours, falling afterwards to 950 hPa by 1500 UTC 21 Sep 2010 as the storm moved into the reintensification stage (Pasch and Kimberlain 2011; Klein et al. 2000). This is near the

time of Figure 38c, which shows ridge amplification as the storm reintensifies. This continues through 0000 UTC 22 Sep 2010, at which point the ridge amplification caused by the now extratropical system has produced a downstream trough off of Europe and Africa that stretches nearly 40° of latitude.

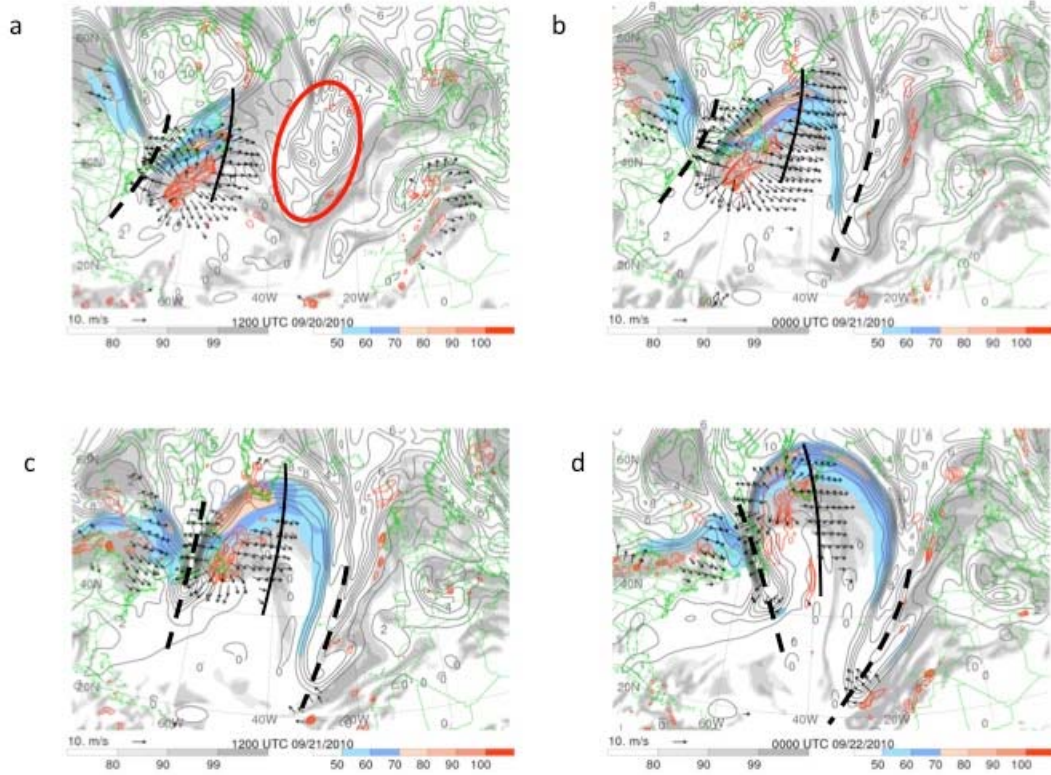


Figure 38. Same as for Figure 22, except for (a) 1200 UTC 20 Sep 2010, (b) 0000 UTC 21 Sep 2010, (c) 1200 UTC 21 Sep 2010, and (d) 0000 UTC 22 Sep 2010 (unpublished figure provided by H. Archambault).

THIS PAGE INTENTIONALLY LEFT BLANK

III. CLIMATOLOGICAL ANALYSIS

With the exception of using 300 hPa meridional winds, as opposed to 250 hPa, the climatology used for this research was developed with the same techniques described in GW13. Because the techniques were applied to the ERA-Interim dataset, it is necessary to ensure the two climatologies are in good agreement in order to validate the results of this research. Specifically, the initial climatology created from the ERA-40 dataset shows distinct regions where RWTs of durations greater than four days and greater than nine days preferentially form and decay. It also gives frequency distributions for the varying lifetimes of the identified RWTs. For comparison, presented in this chapter is a similar, but abbreviated, analysis to that in GW13 of the ERA-Interim RWT climatology. Furthermore, seasonal variations in the number of RWT initiations, as well as longitudinal variations in RWT initiation and decay, will be examined.

A. ERA-40 ROSSBY WAVE TRAIN CLIMATOLOGY

A review of the ERA-40 derived RWT climatology follows. This analysis provides a baseline for comparison of the ERA-Interim derived RWT climatology to follow.

1. Frequency Distribution and Lifetime Correlation

In the GW13 climatology, RWTs varied in lifetime from just two days to upwards of 34 days. Because of the design of the RWT identification methodology, the aforementioned “clipping parameter” plays a role in the statistics that follow. The choice of an absolute clipping parameter τ yields the histogram in Figure 39a. Here, the greatest number of RWTs of durations less than about five days occurs in summer (JJA). According to GW13, beyond RWT durations of about six days the number of RWTs per month decays “approximately exponentially.” The rate of decay of longer-lived RWTs is more rapid for summer than for the other seasons.

To illustrate the sensitivity of the results to the choice of the clipping parameter, Figure 39b presents the same data with a relative clipping parameter, τ^* . The most

immediate change noted is the higher rate of longer duration RWTs during summer. GW13 offers an explanation of this stating that due to the lower amplitude RWTs during summer, the relative clipping parameter, which is correspondingly lower, may not reject smaller wave features not associated with true RWTs.

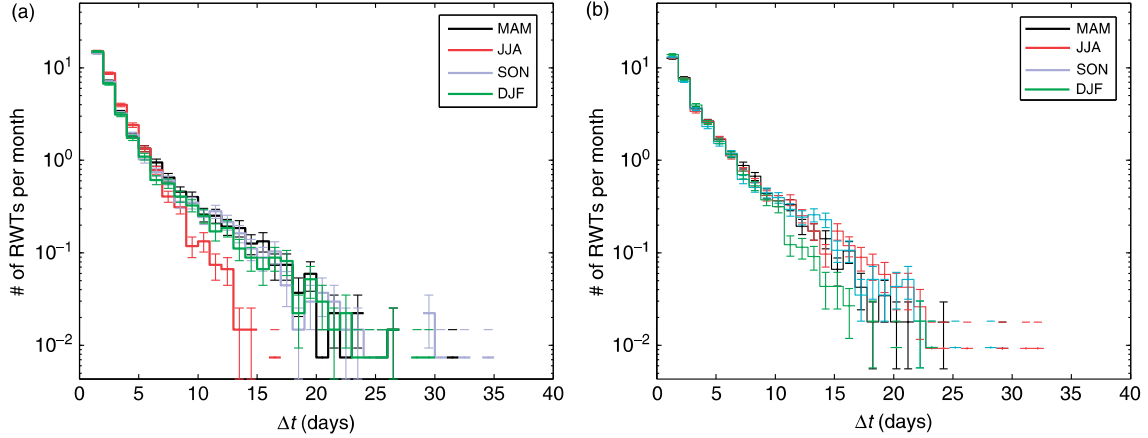


Figure 39. Frequency distribution of RWT lifetime in the ERA-40 data. Each bin has the width of one day. The different shadings refer to the different seasons. The error bars denote \sqrt{N} (where N is the total count in the respective bin), which we take as a measure for the statistical error, divided by the number of considered months and thus scaled to the occurrence of RWTs per months: (a) absolute choice of τ ($\tau = 35 \text{ m s}^{-1}$); (b) relative choice of τ ($\tau^* = 3.5$ (from GW13)).

In order to further characterize the relationship between the longevity of a RWT and its parameters, GW13 analyzed the correlation between RWT duration and both longitudinal extent (shown in Figure 40a) and mean amplitude (shown in Figure 40b). Although the plot in Figure 40a shows a significant degree of spread, the relationship between RWT duration in days and the longitudinal extent traveled is roughly linear, on average, according to GW13. GW13 states that, given a general speed of progression of RWTs, it seems reasonable that for every additional day a RWT lives it travels some mean longitudinal distance further. There is a significant grouping of RWTs across a wide range of durations, all with longitudinal extents less than about 300° . Notwithstanding, it is possible for RWTs to travel greater than 360° and return to their initiation longitude, though this is rare.

Figure 40b shows a plot of the correlation of mean RWT amplitude with duration. According the GW13, for RWTs living less than about seven or eight days, mean amplitude \bar{A} increases with RWT longevity. GW13 demonstrates that near this cutoff in duration, the median of the mean amplitude, indicated by the red line, appears to become asymptotic around 15 ms^{-1} . GW13 attributes this behavior to Rossby wave breaking, a phenomenon by which the material contours of the wave are irreversibly deformed (McIntyre and Palmer 1983). Although there are numerous points indicating RWTs with mean amplitudes greater than 15 ms^{-1} , these tend to be short-lived with the widest spread around seven days duration. The mean amplitude of longer-lived RWTs approaches the asymptotic limit from both directions, indicating that as RWTs live longer, they gradually stabilize in amplitude due to wave breaking.

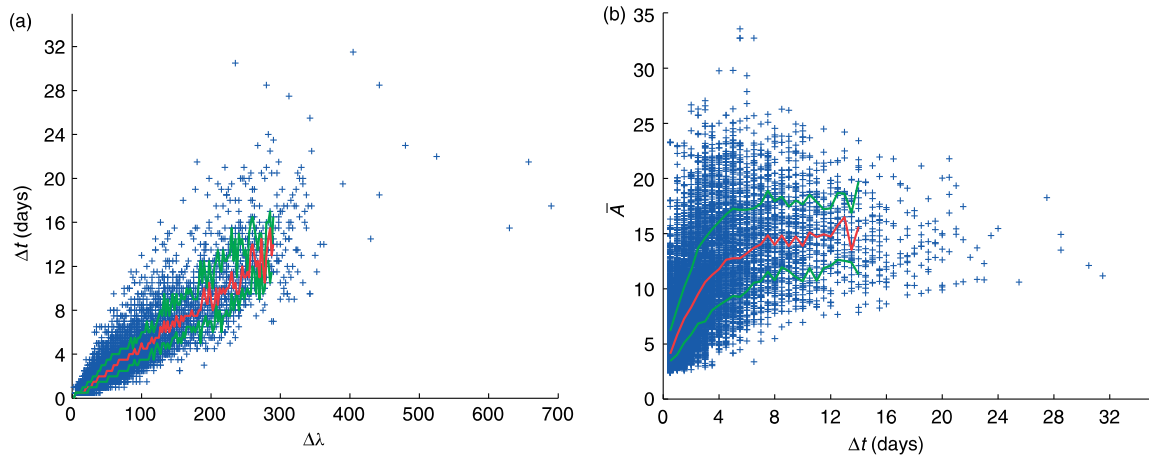


Figure 40. Scatter-plots showing the correlation between different RWT properties: (a) lifetime plotted against the longitudinal extent; and (b) mean amplitude plotted against the lifetime. The central line (red line) depicts the median of the marginal distribution corresponding to a given bin on the x -axis, and the outer lines (green lines) depict the corresponding 20% and 80% percentile, respectively (from GW13).

2. Longitudinal Distribution

Because of their method of extracting RWT objects, GW13 is able to specifically focus on only longer-lived RWTs. RWTs living longer than four days were examined in a group separate from RWTs living longer than nine days. The numbers of RWTs they

catalogued are listed in Table 2. Unsurprisingly, the data show more short-duration RWTs, yet RWTs of either duration are more prevalent in spring and least in summer.

RWT Duration	Spring	Summer	Fall	Winter	Total
> 4 days	714	441	612	573	2340
> 9 days	201	42	196	167	606

Table 2. Seasonal breakdown of longer-lived RWTs identified in the ERA-40 dataset by GW13.

Figure 41 shows a seasonal breakdown of the longitudinal variation of RWT initiation locations. Beginning in spring, RWTs of both long- and short-duration preferentially initiate over the western Pacific. Increasing baroclinicity in this region during spring is favorable for DRVs (BW13) and extratropical cyclogenesis (Wernli and Schwerz 2006), both of which have the potential to excite RWTs. A second region of preferential initiation also exists over North America. Longer duration RWTs are initiated here in fewer numbers, likely due to the fact that few RWTs remain coherent after moving over Europe. Because of their speed of propagation, many RWTs forming over North America may decay over Europe after surviving less than nine days.

By summer, the peak of RWT initiation over the Pacific has decreased and the spread in the region of short-duration RWT initiation over the Pacific has expanded. The peaks of initiation of long- and short-duration RWTs over North America are decreased. Reasonable interpretations of onset regions of long-duration RWTs are very difficult given the small number of them identified during summer (GW13).

Fall conditions indicate the return of a discernible region of long- and short-duration RWTs over the western Pacific. This peak is reduced and spread more zonally than it was in spring. The peak in short-duration RWT initiation over North America is present and has a lower value than it did in summer. While the signal is noisy, there is an increase in the number of long-duration RWTs triggered from the dateline east to North America. RWT initiations over the Pacific increase with the onset of winter.

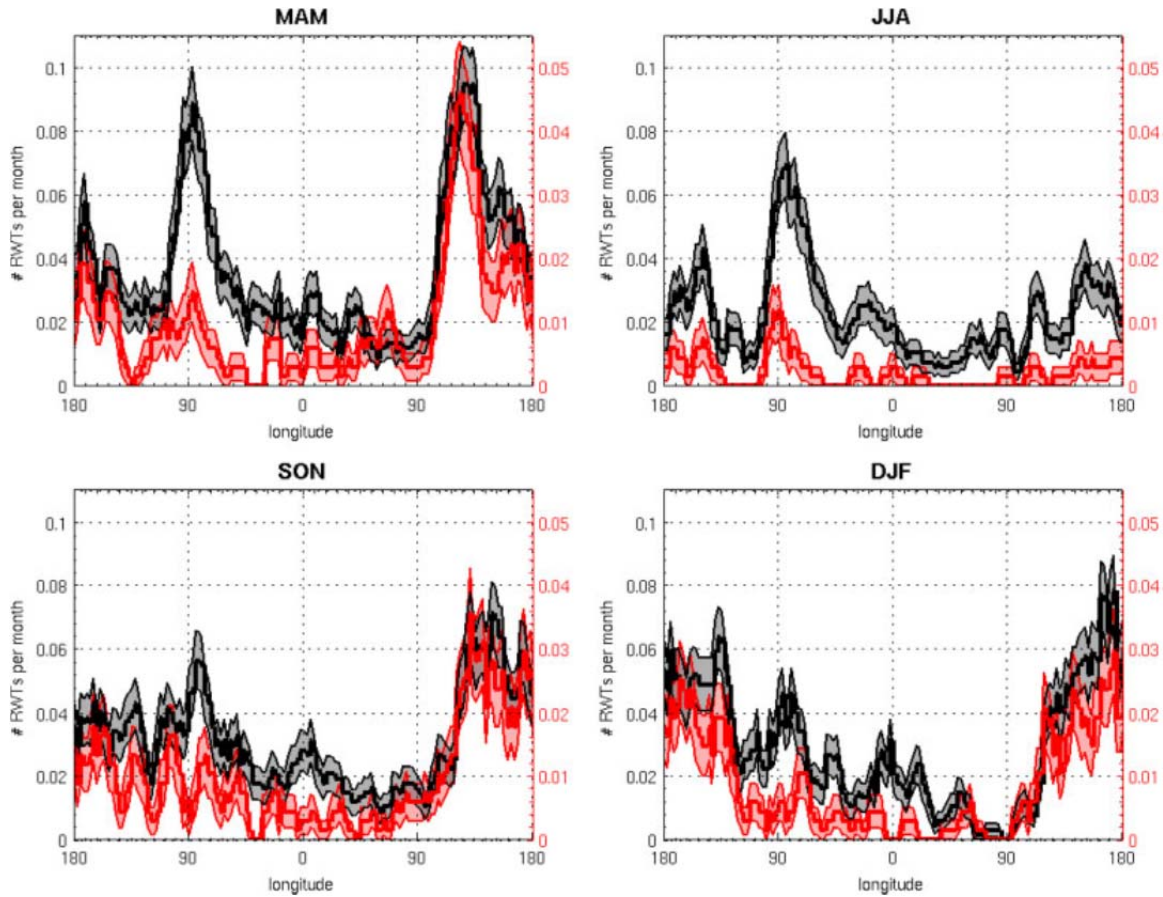


Figure 41. Distribution of the longitudes of onset of RWTs with a minimum lifetime of 4 days (dark/black line, left scale) and 9 days (scaled by a factor of 2, pale/red line, right scale), respectively. MAM, spring; JJA, summer; SON, autumn; DJF, winter. The data, which are available with a resolution of 2.5° in longitude, have been smoothed by a 3-point running mean. The lighter shaded area represents the respective estimate for the statistical error; it was obtained from the square root of the count in each bin, suitably calibrated to the number of RWTs per month and using Gaussian error propagation to deal with the running average. The relatively small bin width is associated with large statistical error, but the structure of the distribution manifests more clearly than with a coarser bin resolution (from GW13).

Similarly, Figure 42 shows the analysis for longitudes of RWT decay. In general, both long- and short-duration RWTs preferentially decay over Europe and North America for all seasons. In spring, the large peak near 0° supports the previous assertion that RWT termination over Europe is a factor in the large number of short-duration RWTs initiated over North America during this season. Additional peaks in long- and short-duration

RWT terminations west of 90°W and over Europe are consistent with regions of Rossby wave breaking. Over North America these breaking waves can form cutoff lows and trigger extratropical cyclogenesis and the initiation of new RWTs, yielding the peaks in RWT initiation over North America in Figure 41. The overall decrease in the number of longer duration RWTs during summer is evident, however, peaks in short-duration RWT termination over North America and Europe remain.

During fall, there is a significant increase in both long- and short-duration RWTs terminating over Europe with continued preferential decay of short-duration RWTs over North America. It is noteworthy that during this season a majority of long-duration RWTs were initiated just west of the date line while a majority also terminated near the prime meridian. Likely at least some of these traveled more than 180° to terminate in Europe, thus dynamically linking sensible weather on opposite sides of the Northern Hemisphere. By winter, the region of increased decay of RWTs of either duration has broadened over Europe, with a spike in short-duration RWT decay over North America remaining.

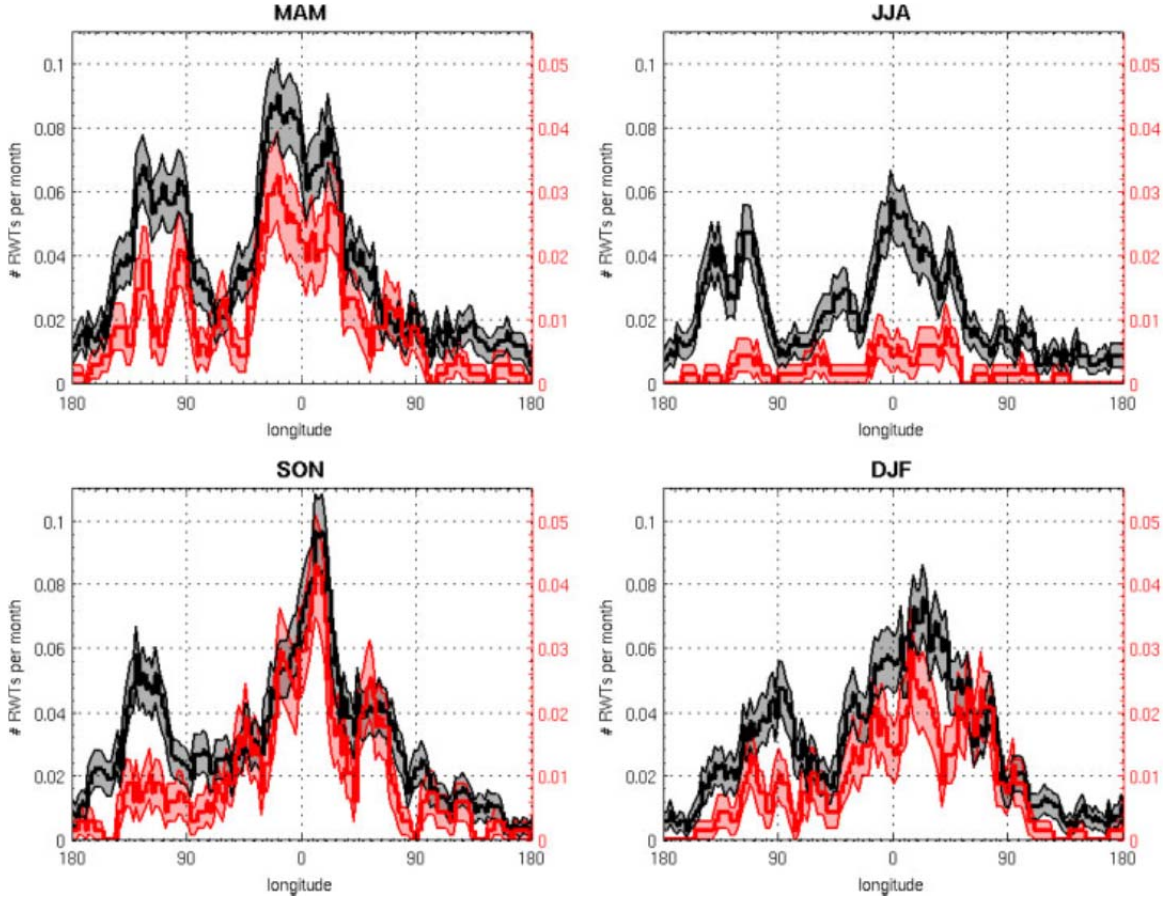


Figure 42. As in Figure 41, except for longitude of decay (from GW13).

B. ERA-INTERIM ROSSBY WAVE TRAIN CLIMATOLOGY

An abbreviated analysis of the ERA-Interim derived RWT climatology follows. To allow for comparison with the ERA-40 analysis, the ERA-Interim data are examined using figures similar to those presented in Section 2 of the preceding section.

1. Longitudinal Distribution

To ensure relative agreement between the ERA-40 and ERA-Interim RWT climatologies, plots of the longitudinal variations in RWT initiation and decay by season were created in a manner similar to Figures 41 and 42. There are some discrepancies in the data that will be briefly addressed. The total number of RWTs by season is presented in Table 2 for comparison with the ERA-40 analysis. The total numbers of long- and short-duration RWTs from the ERA-Interim climatology are within 10% and 13%,

respectively, of the total number of long- and short-duration RWTs in the ERA-40 derived climatology.

RWT Duration	Spring	Summer	Fall	Winter	Total
> 4 days	583	361	565	545	2054
> 9 days	175	26	178	171	550

Table 3. Same as for Table 2 for the ERA-Interim derived RWT climatology.

Figure 43 shows a seasonal breakdown of RWT initiation longitudes. Beginning in spring, the overall shape of the curve is similar to that presented in Figure 41. The ERA-Interim derived climatology contains a peak in RWT initiation over North America, particularly for short-duration RWTs. It also contains similar peaks for long- and short-duration RWTs over the Western Pacific. These peaks are similar in magnitude to those present in the ERA-40 analysis. Two main discrepancies are evident. First, there is an increase in RWT initiations near 30°E. Second, the peak in RWT initiation over the Pacific is broader than the well-defined peak in the ERA-40 derived climatology. For this and all seasons, identifying the roots of these inconsistencies is beyond the scope of this research, but their presence does not detract from this analysis. Because this research focuses on individual RWTs, and identifies areas of genesis and lysis for each case independently, disparities in the overall distribution of RWT initiation and decay regions are inconsequential.

In summer, the ERA-Interim derived climatology of RWT initiations agrees well with the previous work. Well-defined peaks, particularly in the initiation of short-duration RWTs, are noted over the eastern and western boundaries of the Pacific and near 90°W. By fall, the climatologies do not agree as well. First, the broad peak in RWT generation over the Pacific is 0.02–0.03 RWTs month⁻¹ greater in the ERA-Interim derived data. Second, the peak in short-duration RWTs near 0° in the ERA-Interim

derived climatology is roughly doubled from that in the ERA-40 data. Similar patterns of agreement and incongruity are noted in winter.

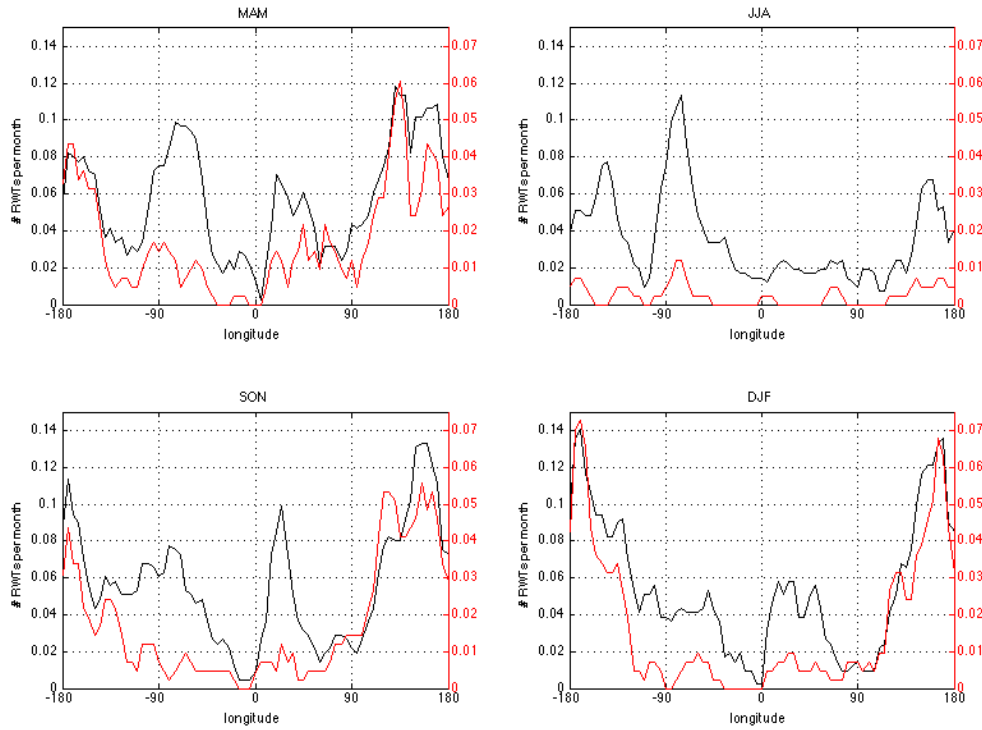


Figure 43. Distribution of RWT initiation longitudes in the ERA-Interim derived climatology. RWTs of a minimum lifetime of four (nine) days are shown using the black (red) line and the left (right) scale. Seasons are denoted by MAM (spring), JJA (summer), SON (fall), and DJF (winter). Longitude bins are 5° wide and are smoothed by a 3-point running mean.

The seasonal breakdowns of longitudes of RWT decay depicted in Figure 44 all show relative agreement with the ERA-40 derived climatology presented in Figure 42. Across all seasons, peaks in RWT decay over western North America and near 0° , and the overall shapes of the curves, are consistent with those in Figure 42, although the ERA-40 derived climatology depicts somewhat broader peaks. The major discrepancy noted is in the peak values of regions of RWT decay. Throughout all four seasons, for

both long- and short-duration RWTs, the peak values of the number of RWTs decaying per month are roughly double those depicted by the ERA-40 derived climatology.

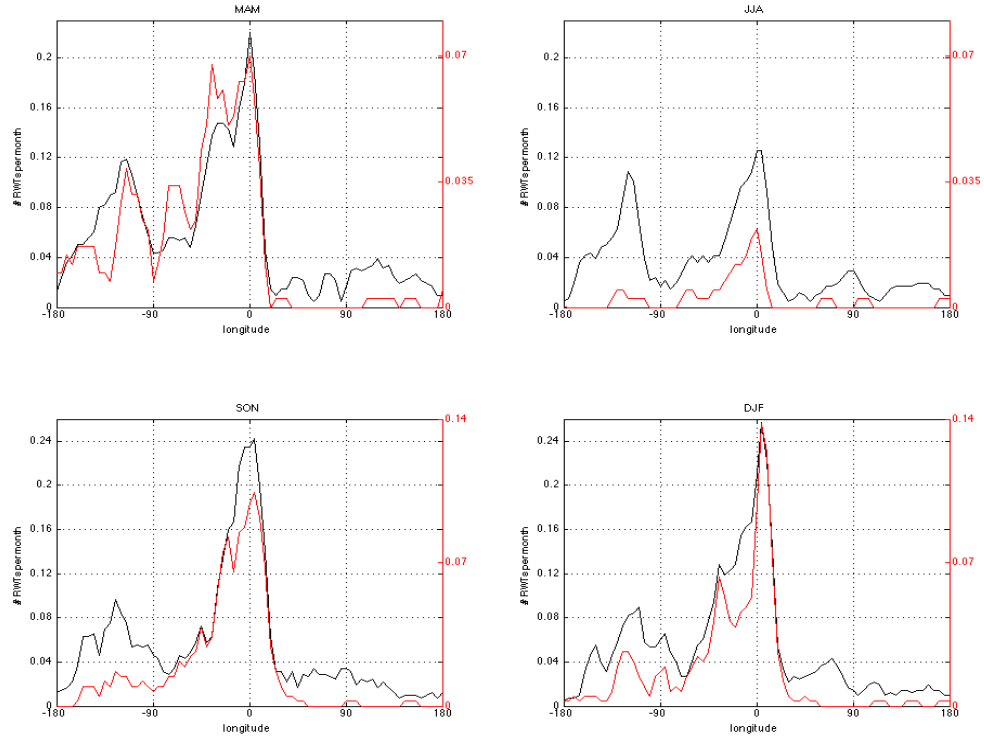


Figure 44. Same as for Figure 43 except for longitudes of RWT decay.

IV. DETAIL OF ROSSBY WAVE TRAIN LIFE CYCLES

The analyses in this chapter build on the discussion in Chapter II, where examples of the triggering of RWTs by four distinct atmospheric phenomena were presented. The focus here will be on the downstream development and RWT termination for the previously presented examples. As described by Chang (1993), because the energy of a RWT travels with a group velocity that is faster than the phase velocity of an individual Rossby wave, the RWT can dynamically force the creation of perturbations on the DT ahead of the wave packet itself.

For all figures in this Chapter, blue circles indicate areas of interest, red circles indicate a triggering phenomenon, solid black lines indicate ridges, dashed black lines indicate troughs, and black arrows indicate movement and direction. Any additional annotations are explained when presented.

A. TROPOPAUSE POLAR VORTEX

Section A describes in detail the lifecycle of a RWT triggered by a TPV over the North Pacific. Highlighted features are used to illustrate downstream development and emphasize the sensible weather impacts resulting from it.

1. Triggering Phase

This section details the lifecycle of RWT number 7805 that was previously shown to be triggered by a TPV at 0000 UTC 25 Oct 2010. Figure 45a defines the time of initiation, stepping forward in 12 hour increments (b,c,d). The TPV responsible for triggering the RWT is highlighted (red circle), as is the first downstream ridge/trough couplet resulting from the perturbation of the waveguide (solid black line/dashed black line, numbered two and three, respectively). Trough one forms equatorward of the triggering TPV, providing upper-level PVA for the region highlighted (blue circle, Figure 45a). This area develops into an EC by 1200 UTC 26 Sep 2010 as indicated by closed SLP contours (not shown). By 1200 UTC 25 Oct 2010 trough one, ridge two, and trough three have all amplified as the TPV continues to move equatorward. Over the next 24

hours these features spread zonally and continue to amplify as they propagate downstream.

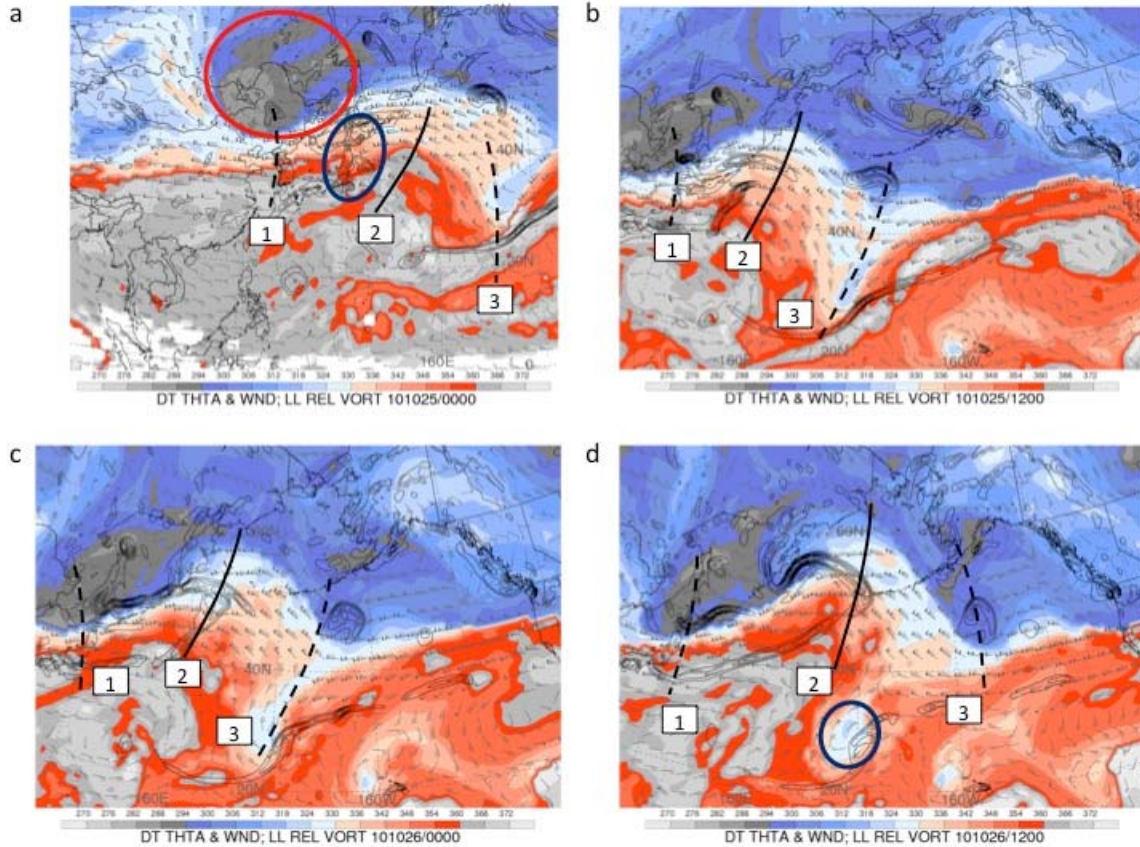


Figure 45. Same as for Figure 21, except for (a) 0000 UTC 25 Oct 2010, (b) 1200 UTC 25 Oct 2010, (c) 0000 UTC 26 Oct 2010, and (d) 1200 UTC 26 Oct 2010 (unpublished figure provided by H. Archambault).

2. Propagation Phase and Downstream Development

Figure 46 shows the first 36 hours of propagation and downstream development of RWT number 7805. By 0000 UTC 27 Oct 2010 the waveguide near trough one has started to return to a mostly zonal flow. Concurrently, the EC that formed and intensified in association with upper-level support downstream of trough one (PVA) is beginning to occlude. Moving over North America in Figure 46b, ridge four begins to develop downstream of trough three. The blue circle highlights a previously existing low (as indicated by SLP plots, not shown) beginning to occlude over the Great Lakes. As ridge

four builds, the waveguide near 100°W (blue circle, Figure 46c,d) is relatively zonal. Through 0000 UTC 28 Oct 2010 trough three deepens and ridge four builds.

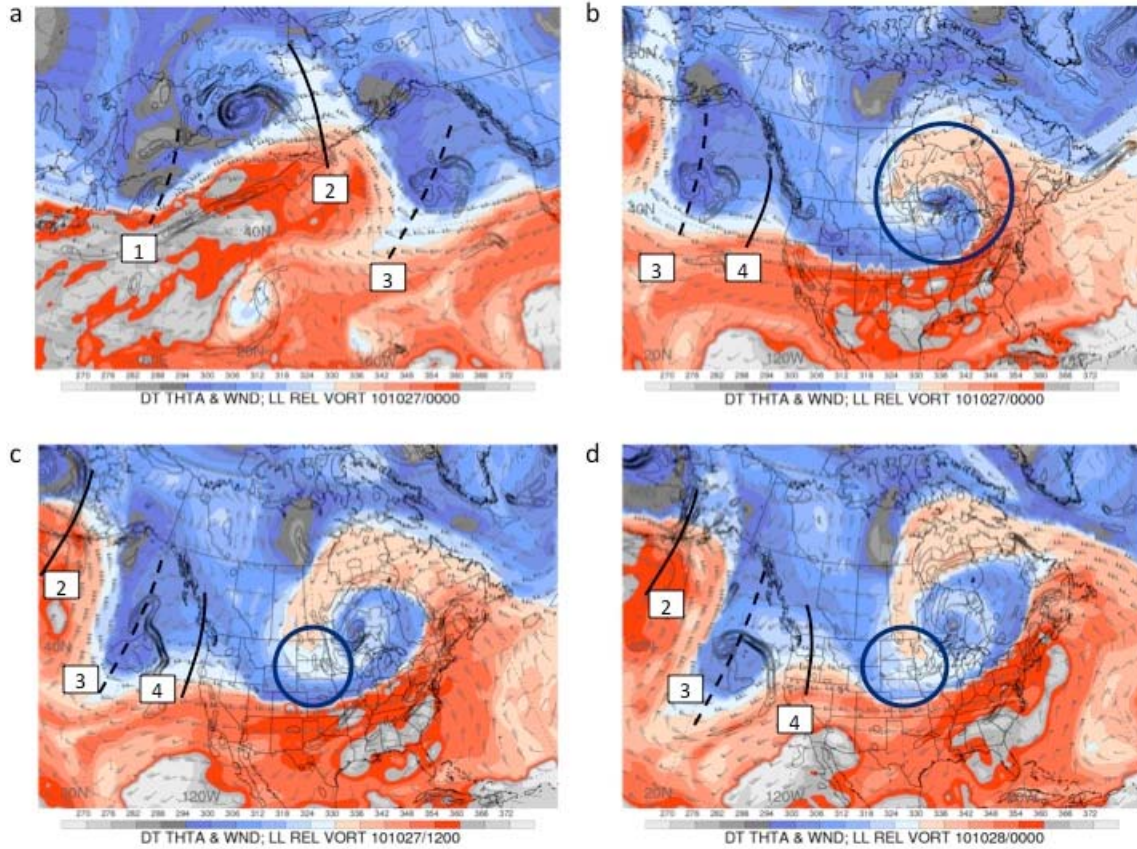


Figure 46. Same as for Figure 21, except for (a) 0000 UTC 27 Oct 2010, (b) 0000 UTC 27 Oct 2010, (c) 1200 UTC 27 Oct 2010, and (d) 0000 UTC 28 Oct 2010 (unpublished figure provided by H. Archambault).

The continued evolution of the RWT from 1200 UTC 28 Oct 2010 to 1200 UTC 29 Oct 2010 is shown in Figure 47. As the previously existing low in Figure 46b occludes, ridge four builds and trough five is formed, indicated by the dashed line in Figure 47a. Over the next 12 hours, ridge four amplifies and trough five deepens. Moving over the North Atlantic in Figure 47c, trough five deepens upstream of a relatively zonal region of the waveguide (blue circle). Trough five continues to deepen through 1200 UTC 29 Oct 2010.

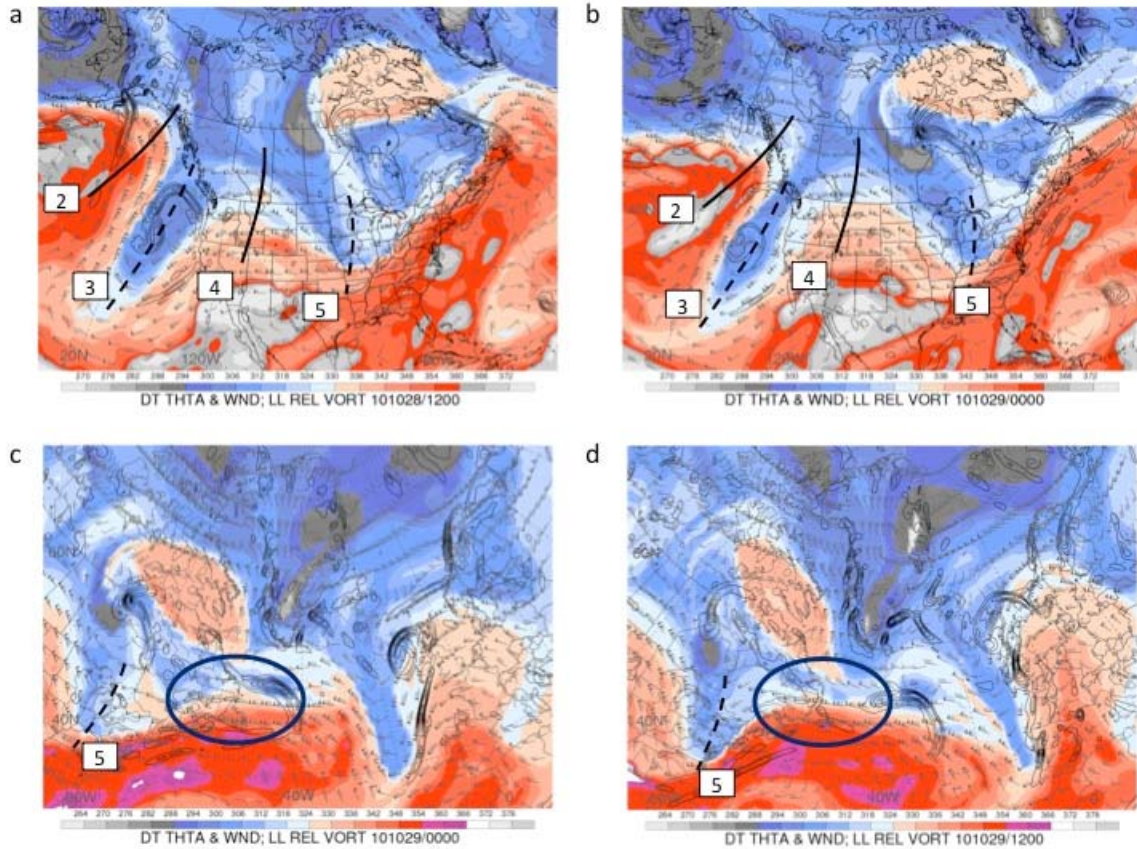


Figure 47. Same as for Figure 21, except for (a) 1200 UTC 28 Oct 2010, (b) 0000 UTC 29 Oct 2010, (c) 0000 UTC 29 Oct 2010, and (d) 1200 UTC 29 Oct 2010 (unpublished figure provided by H. Archambault).

The downstream development associated with a RWT is evident in Figure 48 using 300 hPa meridional wind anomalies from the NCEP Reanalysis dataset averaged between 25°–55°N. The diagram begins at 0000 25 Oct 2010 (top) and ends at 0000 29 Oct 2010 (bottom). Figure 48 shows clearly ridge two intensifying near 1200 UTC 26 Oct 2010. Before 0000 UTC 27 Oct 2010, trough three began developing and nearly simultaneously ridge four amplified. The three features propagate eastward until 0000 UTC 28 Oct 2010, after which ridge two decays. Trough three begins to decay while ridge four amplifies until 0000 UTC 29 Oct 2010, when trough five forms.

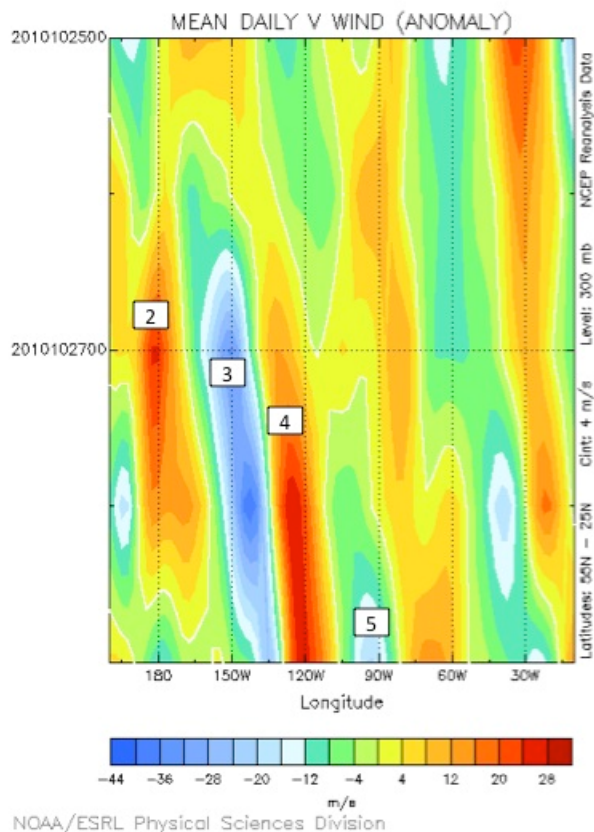


Figure 48. Same as for Figure 24 except from 0000 UTC 25 Oct 2010 to 0000 UTC 29 Oct 2010. (Image provided by the NOAA/ESRL Physical Sciences Division).

The latter portion of the lifecycle of RWT number 7805 (0000 UTC 30 Oct 2010 through 1200 UTC 31 Oct 2010) is shown in Figure 49. From 0000 to 1200 UTC 30 Oct 2010, trough five provides upper-level PVA support, ridge six amplifies, and the previously existing region of low potential temperature downstream, indicated by the blue circle in Figure 49a, develops into trough seven. Concurrently, an EC is formed as indicated by the low-level vorticity and closed SLP contours (not shown) between trough five and ridge six. This EC is occluding by 1200 UTC 31 Oct 2010 as trough five has decayed, ridge six builds, and trough seven deepens.

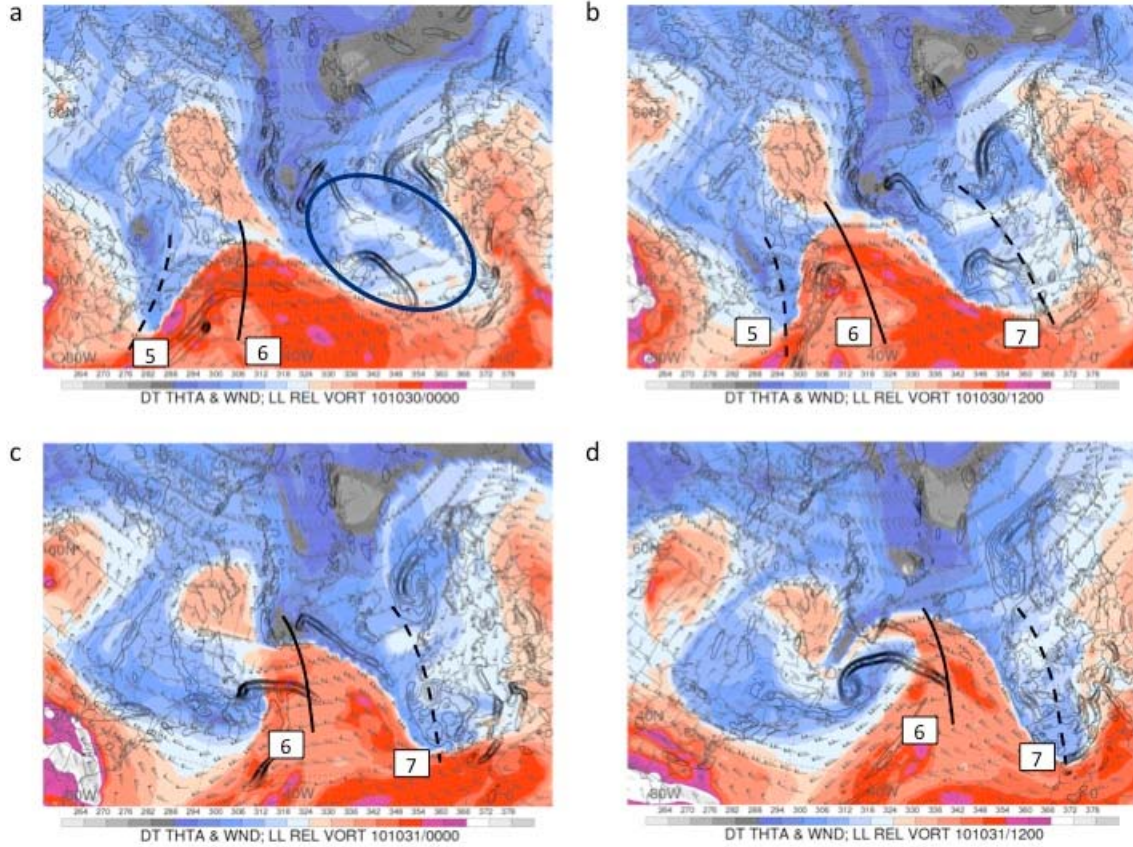


Figure 49. Same as for Figure 21, except for (a) 0000 UTC 30 Oct 2010, (b) 1200 UTC 30 Oct 2010, (c) 0000 UTC 31 Oct 2010, and (d) 1200 UTC 31 Oct 2010 (unpublished figure provided by H. Archambault).

3. Termination Phase

Figure 50 shows the decay of RWT number 7805, which occurs at 1200 UTC 02 Nov 2010. Beginning at 0000 UTC 01 Nov 2010, the EC described in the previous paragraph occludes and Rossby wave breaking ensues. A cutoff low forms by 1200 UTC 01 Nov 2010 (blue circle, Figure 50b). This Rossby wave-breaking event is consistent with the dynamics of the surrounding waveguide. In this region, meridional temperature gradients are decreased, as is baroclinicity, and the weaker waveguide is unable to support high amplitude Rossby waves.

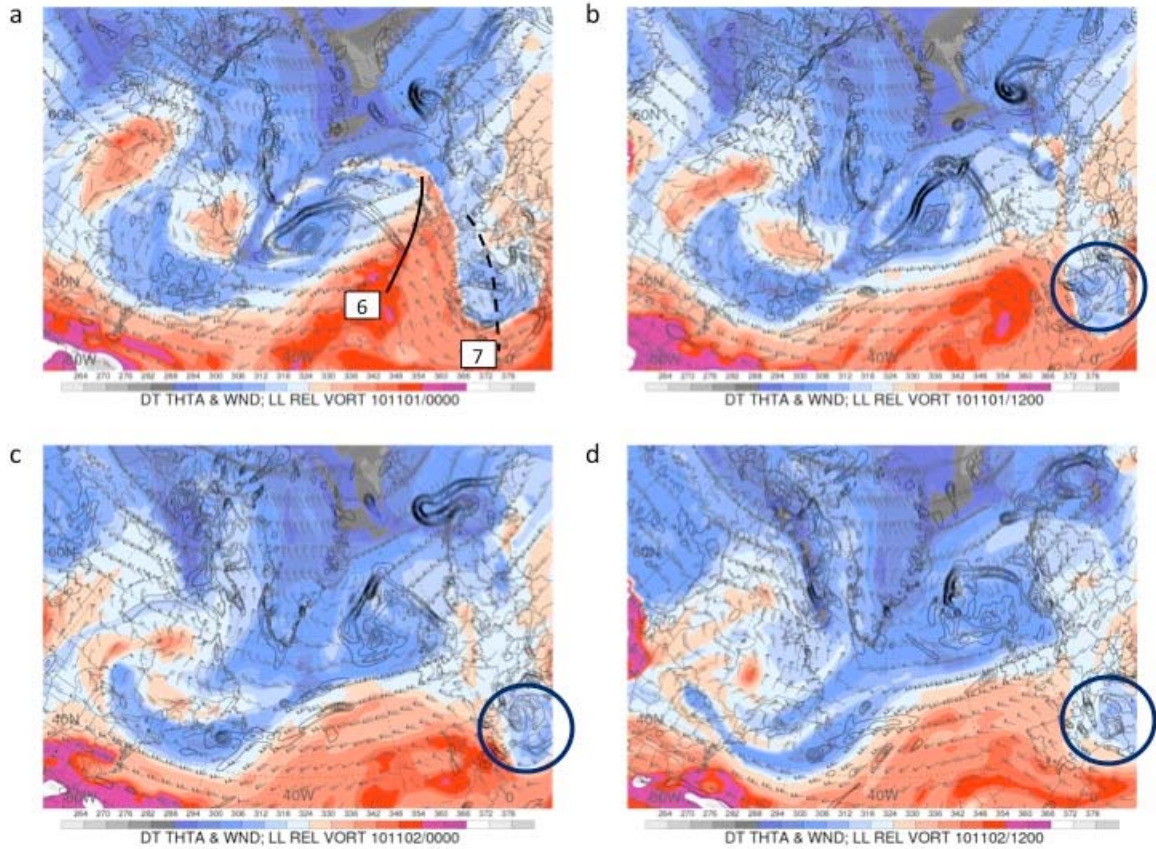


Figure 50. Same as for Figure 21, except for (a) 0000 UTC 01 Nov 2010, (b) 1200 UTC 01 Nov 2010, (c) 0000 UTC 02 Nov 2010, and (d) 1200 UTC 02 Nov 2010 (unpublished figure provided by H. Archambault).

Figure 51 presents a Hovmöller diagram created in a manner similar to Figure 48. It depicts the end of the lifecycle of RWT number 7805. The diagram begins at 0000 UTC 29 Oct 2010, moves through RWT decay at 1200 UTC 02 Nov 2010, and ends at 0000 UTC 06 Nov 2010. The Hovmöller plot shows that after 0000 30 Oct 2010, ridge six begins to decay as the EC occludes and Rossby wave breaking occurs 24 hours later. The blue circle denotes the cutoff low formed by the Rossby wave-breaking event. This cutoff low occurs alongside the decay of ridge six and the RWT climatology gives an ending time for RWT number 7805 of 1200 UTC 02 Nov 2010.

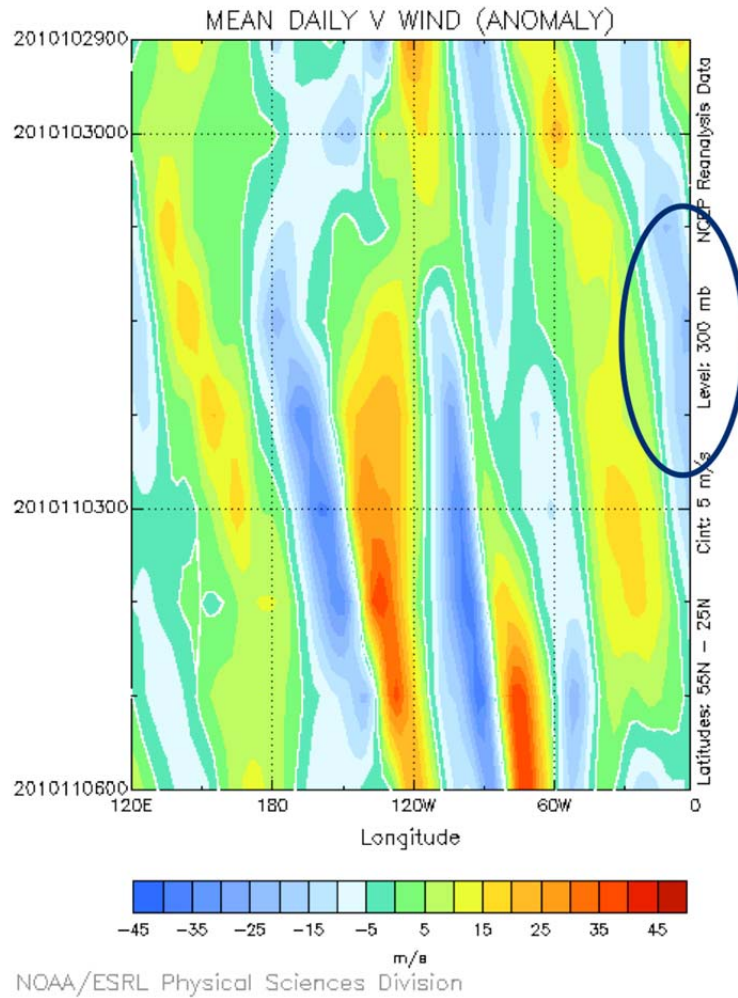


Figure 51. Same as for Figure 24 except from 0000 UTC 29 Oct 2010 to 0000 UTC 06 Nov 2010. (Image provided by the NOAA/ESRL Physical Sciences Division).

4. Sensible Weather Impacts

Sensible weather can be created along the propagation path of a RWT as well as at the region of termination. Because this research is focused on downstream development over Europe, only examples of sensible weather impacts near the region of RWT lysis will be presented.

Even in the region of RWT termination, sensible weather impacts need not occur only at the time of decay, but can manifest hours or days prior. Figure 52 shows a SLP plot for the North Atlantic at 0000 UTC 31 Oct 2010, 60 hours before the lysis of RWT

number 7805. It shows an EC over the North Atlantic indicated by the closed SLP contours with a central pressure of 968 hPa. Closer to Europe, another low sits south of the United Kingdom with a central pressures of 984 hPa.

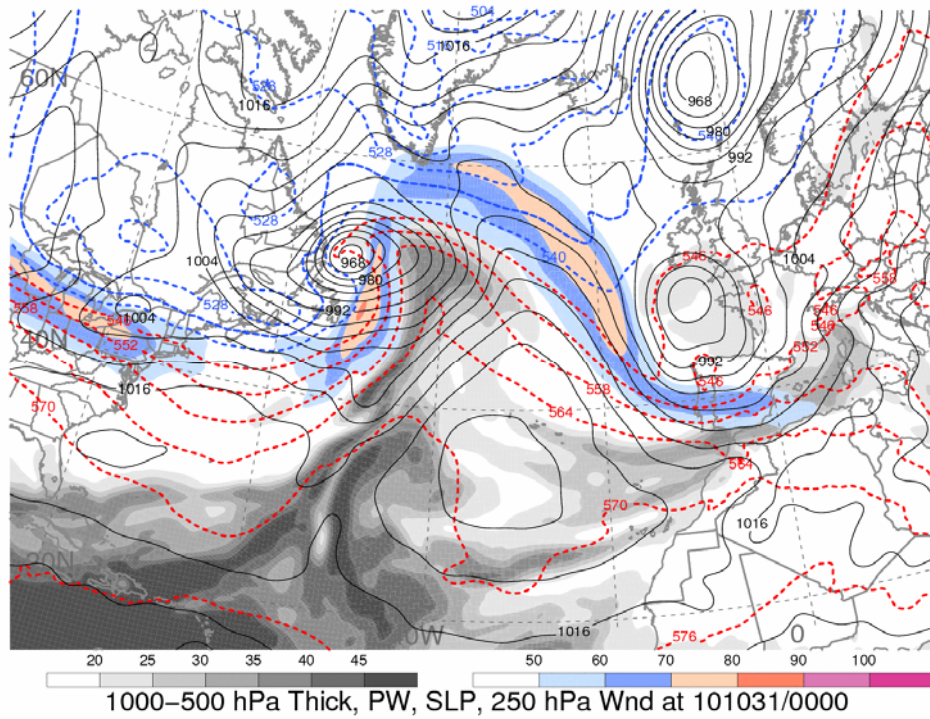


Figure 52. Same as for Figure 23, except for 0000 UTC 31 Oct 2010 (figure provided by H. Archambault).

This low is indicated by the negative SLP anomaly south of the UK shown in Figure 53. This plot was created with 1-day SLP anomalies from the NCEP Operational dataset for 31 Oct 2010. Without further analysis this research cannot quantify how anomalous these values are for any of the cases presented, but it is sufficient to demonstrate the downstream development of a low-pressure system associated with a RWT. The region of anomalous low pressure in Figure 53 is associated with a cyclonic circulation and tropical storm force wind anomalies approaching 22 m s^{-1} , as indicated by the warmer colors west of Portugal in Figure 54. Figure 54 shows 1-day 1000 hPa wind anomalies, also from the NCEP Operational dataset, for 31 Oct 2010. Together, these graphics demonstrate the sensible weather impacts over Europe resulting from the

downstream development of RWT number 7805, which was triggered in the Western Pacific six days earlier.

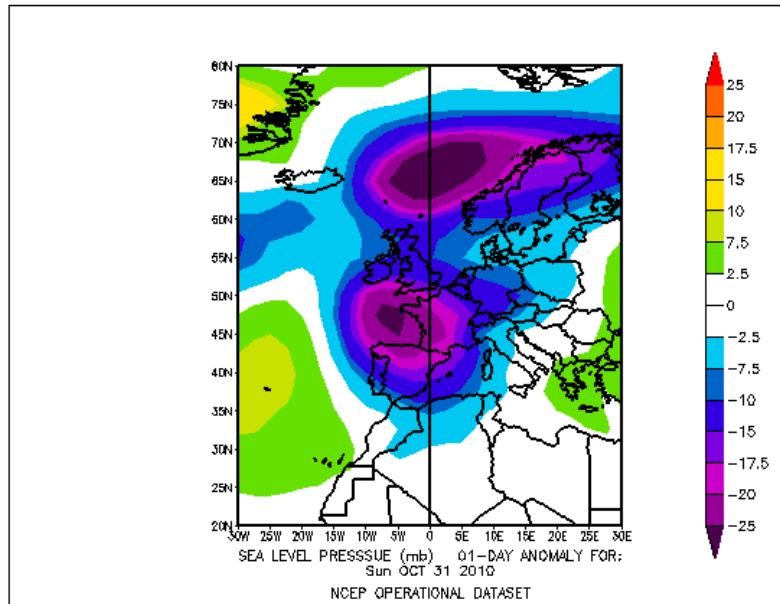


Figure 53. A 1-day SLP anomaly (color shading, hPa) from the NCEP operational dataset for 31 Oct 2010. (Image provided by the NOAA/ESRL Physical Sciences Division).

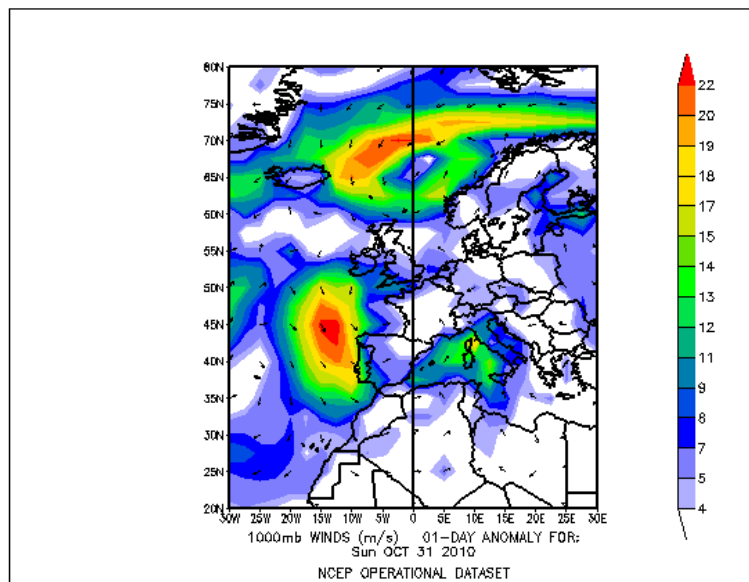


Figure 54. A 1-day 1000 hPa wind anomaly (color shading, m s^{-1}) from the NCEP operational dataset for 31 Oct 2010. (Image provided by the NOAA/ESRL Physical Sciences Division).

B. WARM CONVEYOR BELT

In this section, the lifecycle of RWT number 6824 is presented. As previously shown, this RWT was triggered by a WCB over North America. This example aligns well with the outline of the proposed experiment described in Chapter I in that the RWT is triggered near the entrance to the North Atlantic waveguide and terminates over Europe.

1. Triggering Phase

The climatology used for this research states that RWT number 6824 began at 0000 UTC 17 Sep 2006, however, when examining DT maps, significant forcing does not occur until 36 hours later at 1200 UTC 18 Sep 2006. It is the researcher's assessment that this latter time corresponds to the initiation of RWT number 6824 by a WCB associated with an EC.

At 1200 UTC 15 Sep 2006, Figure 55a shows a previously existing cutoff low denoted trough one. Immediately downstream the waveguide is relatively zonal, as highlighted by the blue circle. Over the next 36 hours, an EC develops as indicated by the lower-level vorticity (red circle, Figure 55d) and closed SLP contours (not shown). By 0000 UTC 17 Sep 2006, the climatological initiation time of the RWT, an area of higher potential temperature associated with a WCB is extending poleward downstream of the lower-level vorticity maximum of the EC (red circle, Figure 55d). Although evidence exists indicating the initiation of a WCB, the waveguide poleward remains relatively zonal.

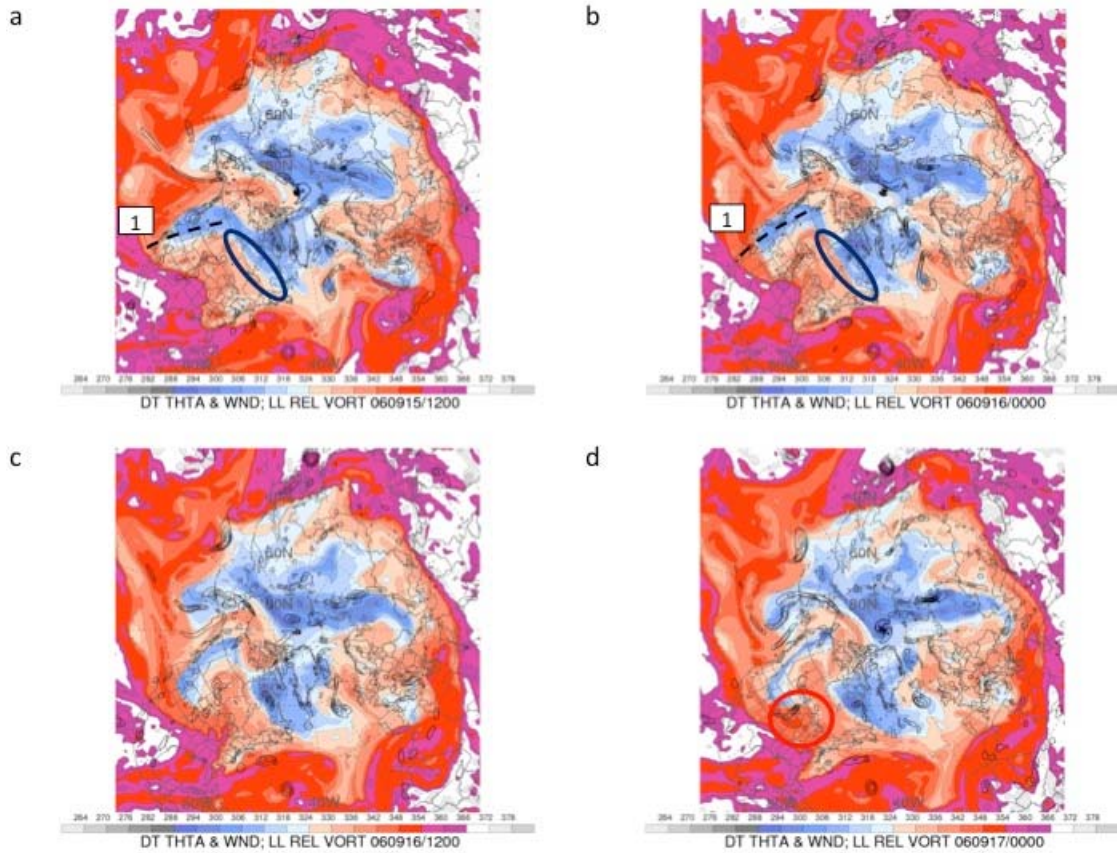


Figure 55. Same as for Figure 21, except for (a) 1200 UTC 15 Sep 2006, (b) 0000 UTC 16 Sep 2006, (c) 1200 UTC 16 Sep 2006, and (d) 0000 UTC 17 Sep 2006 (unpublished figure provided by H. Archambault).

Moving over North America, Figure 56a shows a more detailed view of the same time as Figure 55d, 0000 UTC 17 Sep 2006. The red circle indicates the triggering mechanism. The WCB intensifies, evidenced by the region of high potential temperature air extending poleward as indicated by the black arrow in Figure 56b. The blue circle shown highlights a region of the waveguide that remains unperturbed to this point. The coherent airstream of the WCB continues to move poleward through 0000 UTC 18 Sep 2006 (black arrow, Figure 56c). Twelve hours later, trough two develops upstream of the WCB, now denoted ridge three, and RWT initiation has occurred.

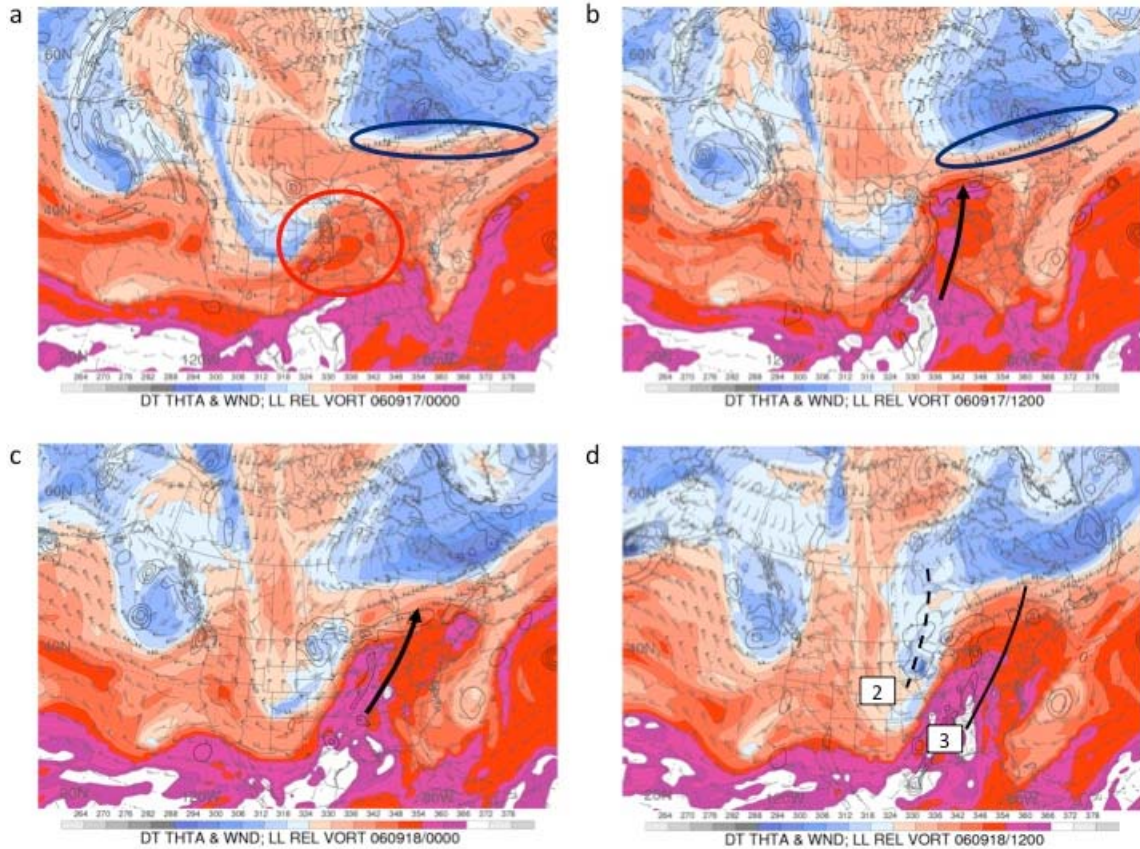


Figure 56. Same as for Figure 21, except for (a) 0000 UTC 17 Sep 2006, (b) 1200 UTC 17 Sep 2006, (c) 0000 UTC 18 Sep 2006, and (d) 1200 UTC 18 Sep 2006 (unpublished figure provided by H. Archambault).

2. Propagation Phase and Downstream Development

Over the North Atlantic, ridge two amplifies while trough four develops downstream as indicated in Figure 57a, which shows the North Atlantic waveguide at 0000 UTC 19 Sep 2006. The blue circle highlights a relatively unperturbed region of the waveguide downstream. By 1200 UTC 19 Sep 2006, Figure 57b indicates trough four has become an EC as indicated by the lower-level vorticity structure. Additional SLP plots (not shown) indicated this EC reaches a minimum central pressure of 964 hPa at 1200 UTC 20 Sep 2006. Downstream of the EC, ridge five and trough six form. Over the next 24 hours, the EC now denoted four begins to occlude as ridge five builds and trough six deepens.

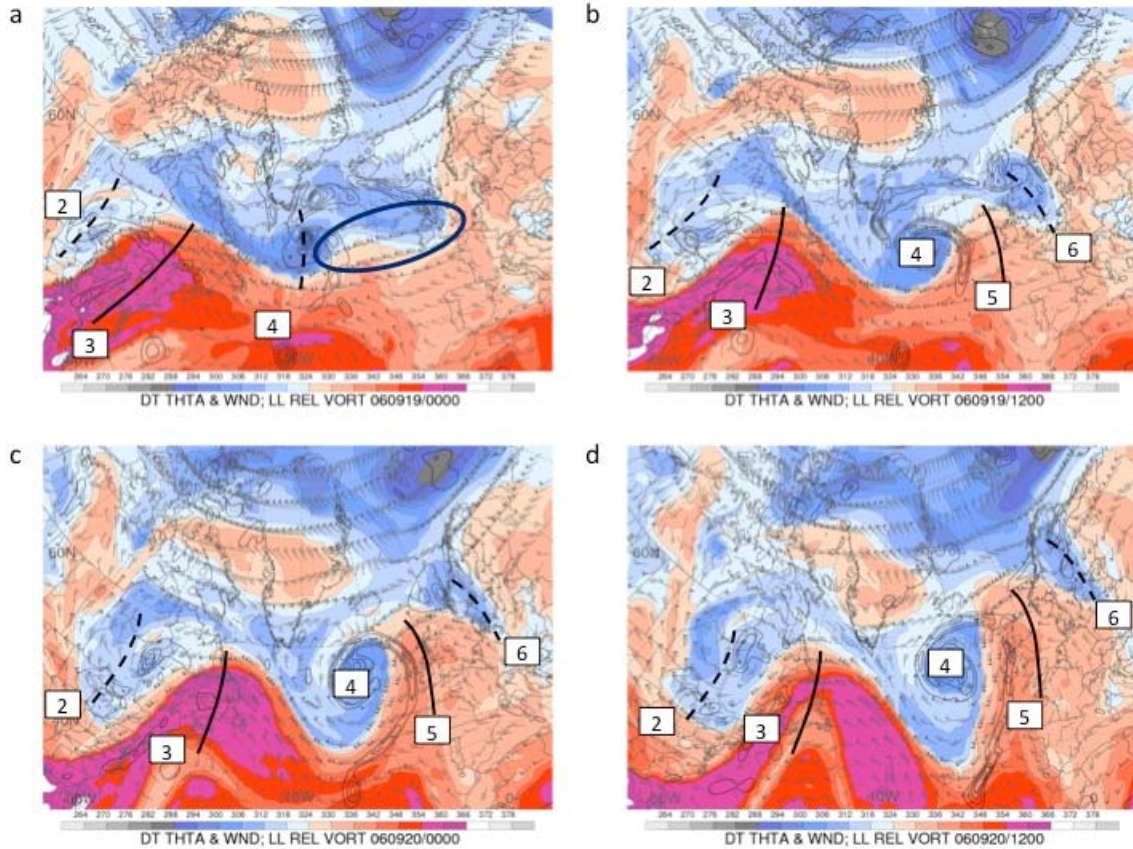


Figure 57. Same as for Figure 21, except for (a) 0000 UTC 19 Sep 2006, (b) 1200 UTC 19 Sep 2006, (c) 0000 UTC 20 Sep 2006, and (d) 1200 UTC 20 Sep 2006 (unpublished figure provided by H. Archambault).

At 0000 UTC 21 Sep 2006, EC four is occluded, and Rossby wave breaking takes place as shown in Figure 58a, where ridge five is amplified. Rossby wave breaking continues over the next 36 hours. By 1200 UTC 22 Sep 2006 EC four is a cutoff low and ridge five is a broad region of high potential temperature over Europe.

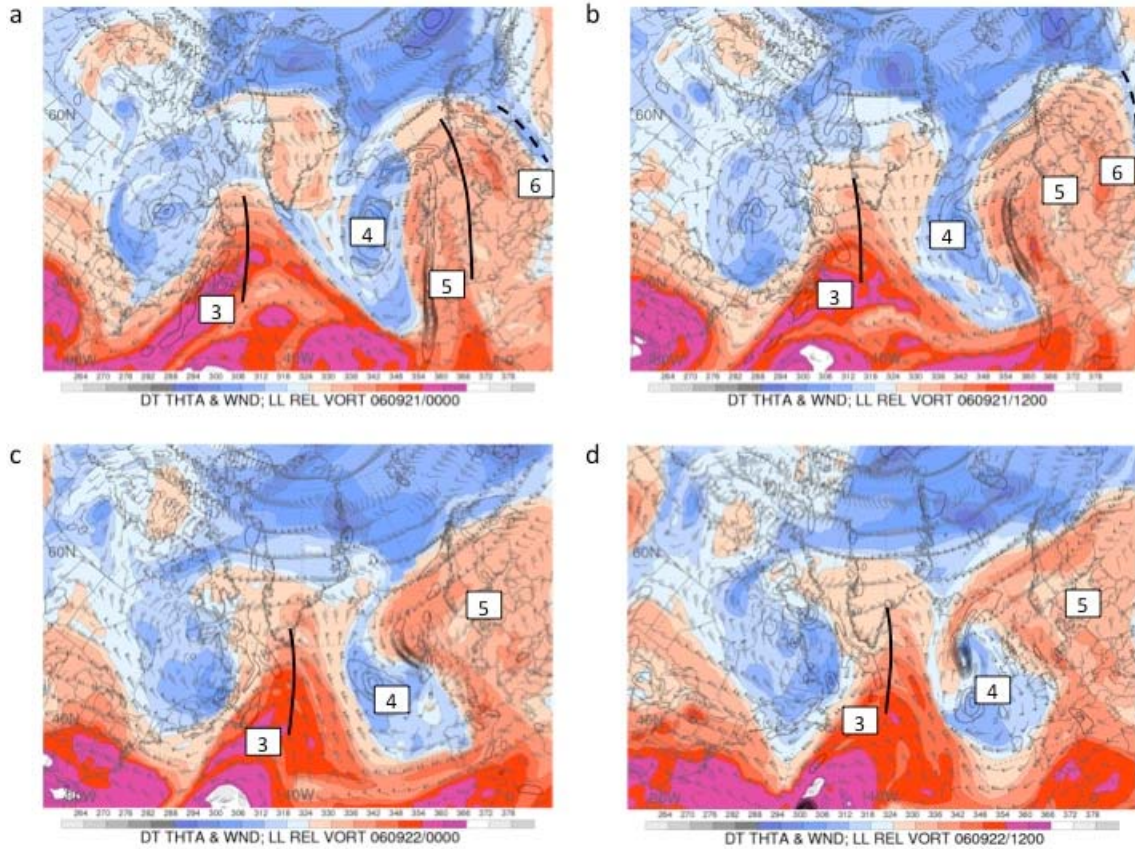


Figure 58. Same as for Figure 21, except for (a) 0000 UTC 21 Sep 2006, (b) 1200 UTC 21 Sep 2006, (c) 0000 UTC 22 Sep 2006, and (d) 1200 UTC 22 Sep 2006 (unpublished figure provided by H. Archambault).

3. Termination Phase

The RWT climatology used for this research states that RWT number 6824 terminated at 1200 UTC 24 Sep 2006. Figure 59a shows the locations of ridge three, cutoff low four, and ridge five 36 hours prior to this. At 1200 UTC 23 Sep 2006 there is a region of higher potential temperature air poleward of cutoff four as it moves equatorward. This region becomes a cutoff high and is surrounded by lower potential temperature air poleward of cutoff four, which has rejoined the waveguide poleward of ridge three by the time of RWT decay. No additional features are produced as a result of downstream development.

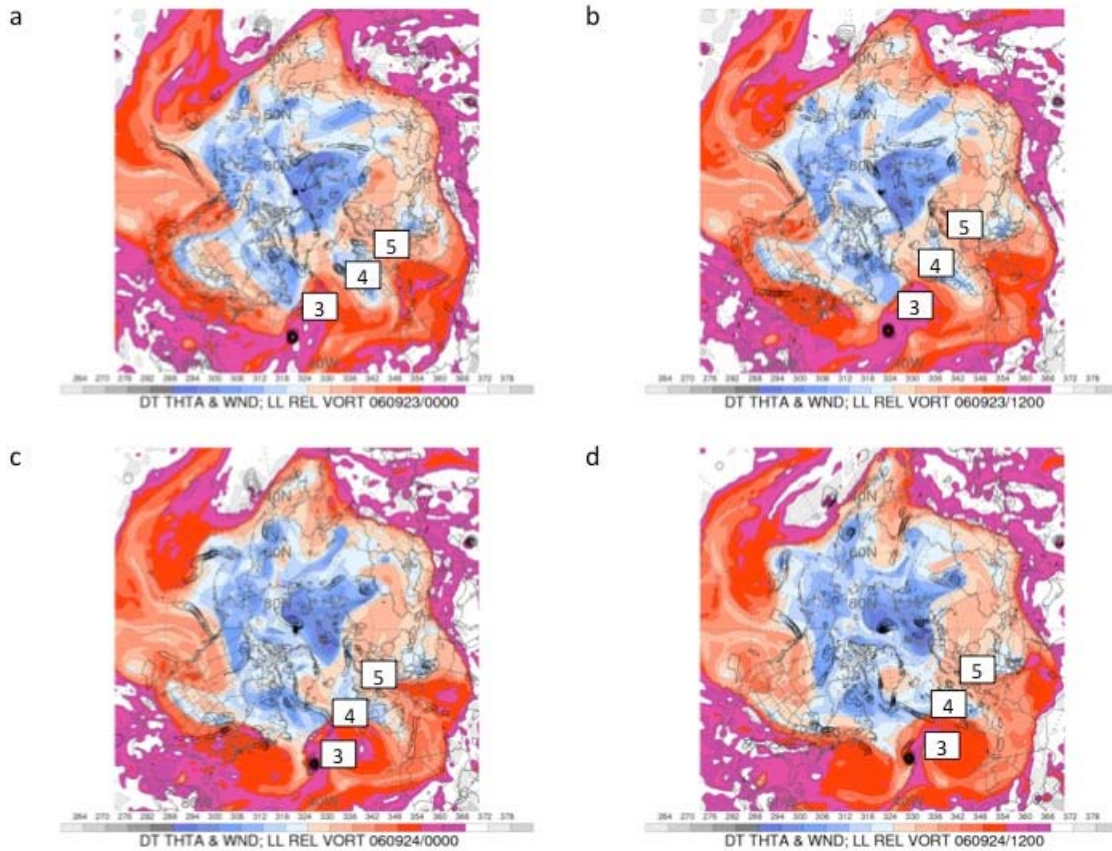


Figure 59. Same as for Figure 21, except for (a) 0000 UTC 23 Sep 2006, (b) 1200 UTC 23 Sep 2006, (c) 0000 UTC 24 Sep 2006, and (d) 1200 UTC 24 Sep 2006 (unpublished figure provided by H. Archambault).

A Hovmöller diagram of the lifecycle of RWT number 6824 is presented in Figure 60. This graphic is the same as the example presented in Figure 24, with troughs and ridges labeled to coincide with the features described throughout the lifecycle analysis of RWT number 6824. The time of RWT genesis is 1200 UTC 18 Sep 2006. Here, the Hovmöller diagram shows the formation of trough four downstream of ridge three and trough two. As time increases downward on the plot, the eastward propagation and downstream development of trough four and ridge five are shown. The time of RWT decay, 1200 UTC 24 Sep 2006, shows the decay of ridge five.

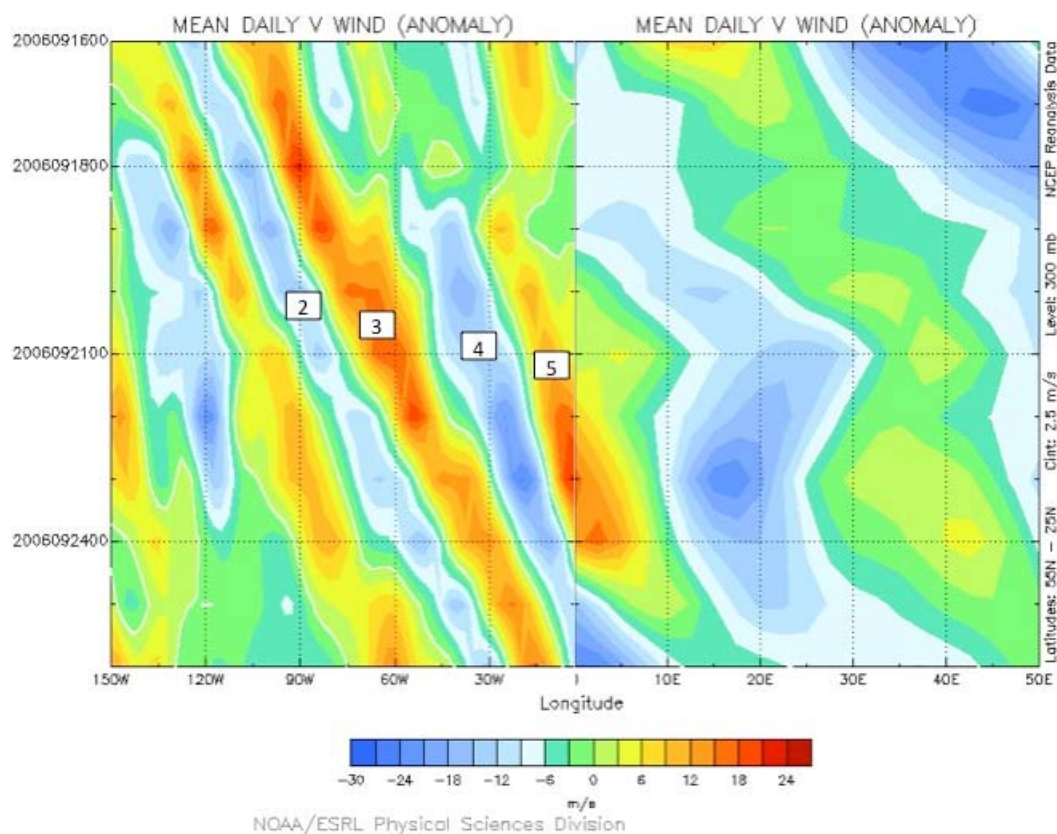


Figure 60. Same as for Figure 24 except with features of RWT number 6824 labeled. (Image provided by the NOAA/ESRL Physical Sciences Division).

4. Sensible Weather Impacts

The downstream development of RWT number 6824 produces the previously described cutoff low four west of the UK at 0000 UTC 23 Sep 2006. The SLP plot in Figure 61 shows the cutoff low reached a central pressure of 988 hPa 36 hours before RWT decay.

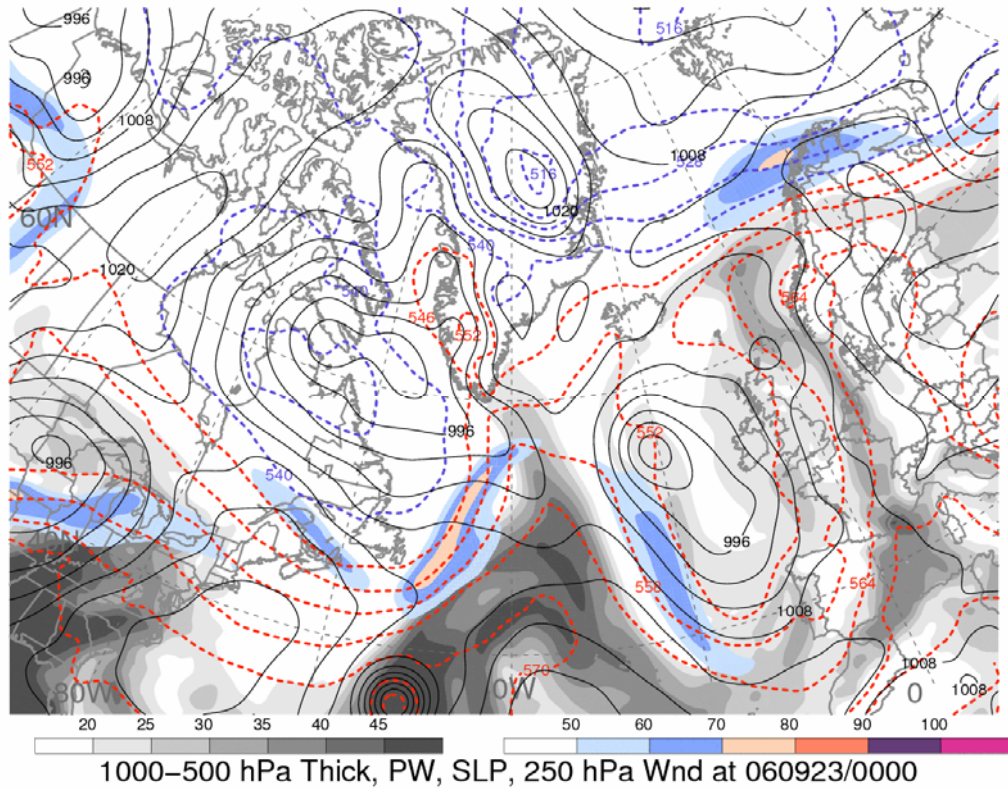


Figure 61. Same as for Figure 23, except for 0000 UTC 23 Sep 2006 (figure provided by H. Archambault).

This region is depicted as an area of cooler colors in the 1-day SLP anomaly plot for 23 Sep 2006 shown in Figure 62. As with the TPV example presented, it is beyond the scope of this study to quantify how anomalous this particular occurrence is, but this cutoff low produces tropical storm force winds approaching 22 m s^{-1} , as depicted in the 1-day 850 hPa wind anomalies for 23 Sep 2006 shown in Figure 63. These conditions are a response to the downstream development of RWT number 6824 that was triggered six days earlier over North America.

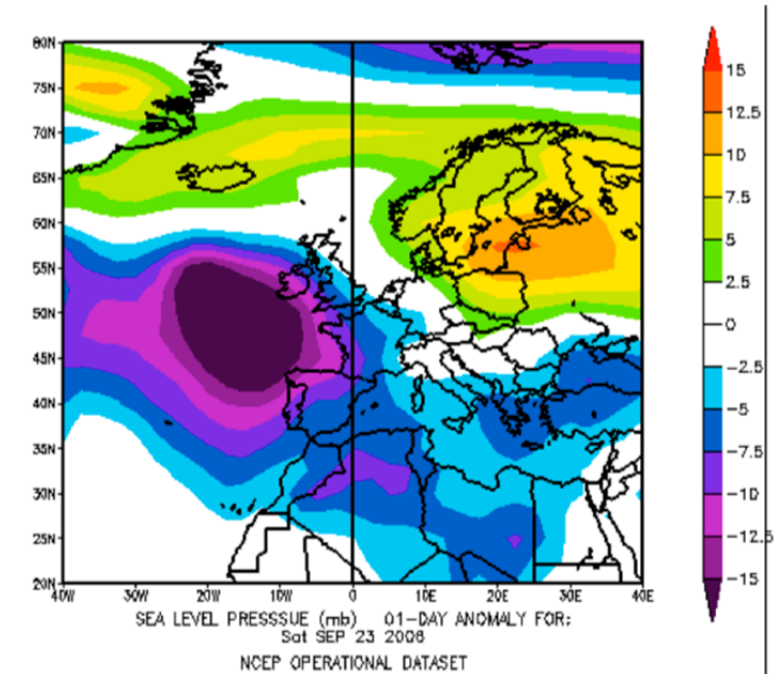


Figure 62. Same as for Figure 53, except for 23 Sep 2006. (Image provided by the NOAA/ESRL Physical Sciences Division).

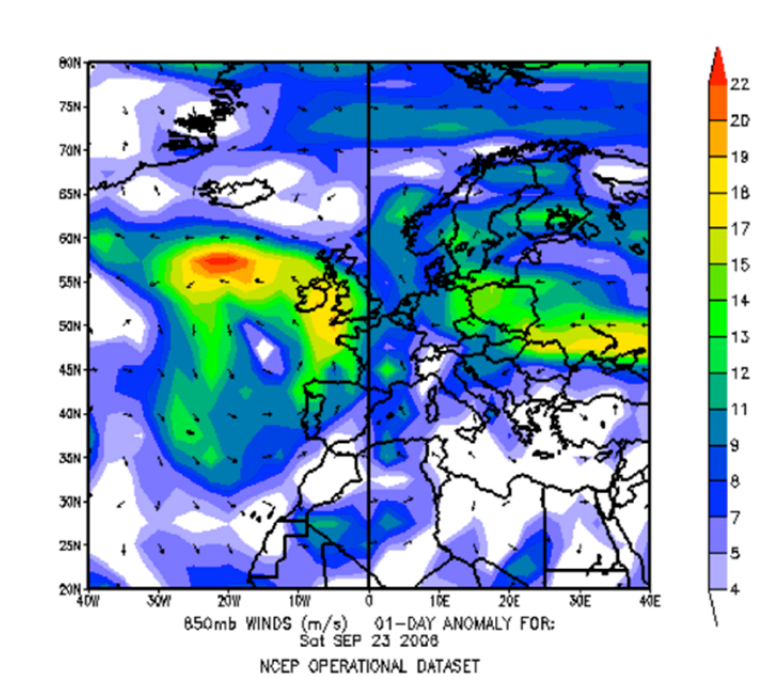


Figure 63. Same as for Figure 54 except at the 850 hPa level for 23 Sep 2006. (Image provided by the NOAA/ESRL Physical Sciences Division).

C. DIABATIC ROSSBY VORTEX

The RWT presented in this section was triggered by a DRV over the Western Pacific and terminated eight days later over Europe. This example illustrates the far-reaching potential for impactful weather associated with the downstream development of RWTs.

1. Triggering Phase

The RWT number 6826 was initiated at 0000 UTC 25 Sep 2006. Previous analysis has shown the triggering mechanism was a DRV in the Western Pacific near 165°E. Thirty-six hours prior to RWT initiation, at 1200 UTC 23 Sep 2006, Figure 64a shows the DT over the Western Pacific with the triggering mechanism indicated by a red circle. Also highlighted is a previously existing upper-level trough (blue circle). The DRV is distinguished by closed contours of low-level relative vorticity and its position is confirmed as a DRV in the BW13 climatology. As the DRV approaches the waveguide it interacts with the upstream trough and by 1200 UTC 24 Sep 2006 the previously existing upper-level trough deepens and is annotated as trough one, while ridge two is formed. These features further amplify, showing RWT initiation at 0000 UTC 25 Sep 2006 (Figure 64d).

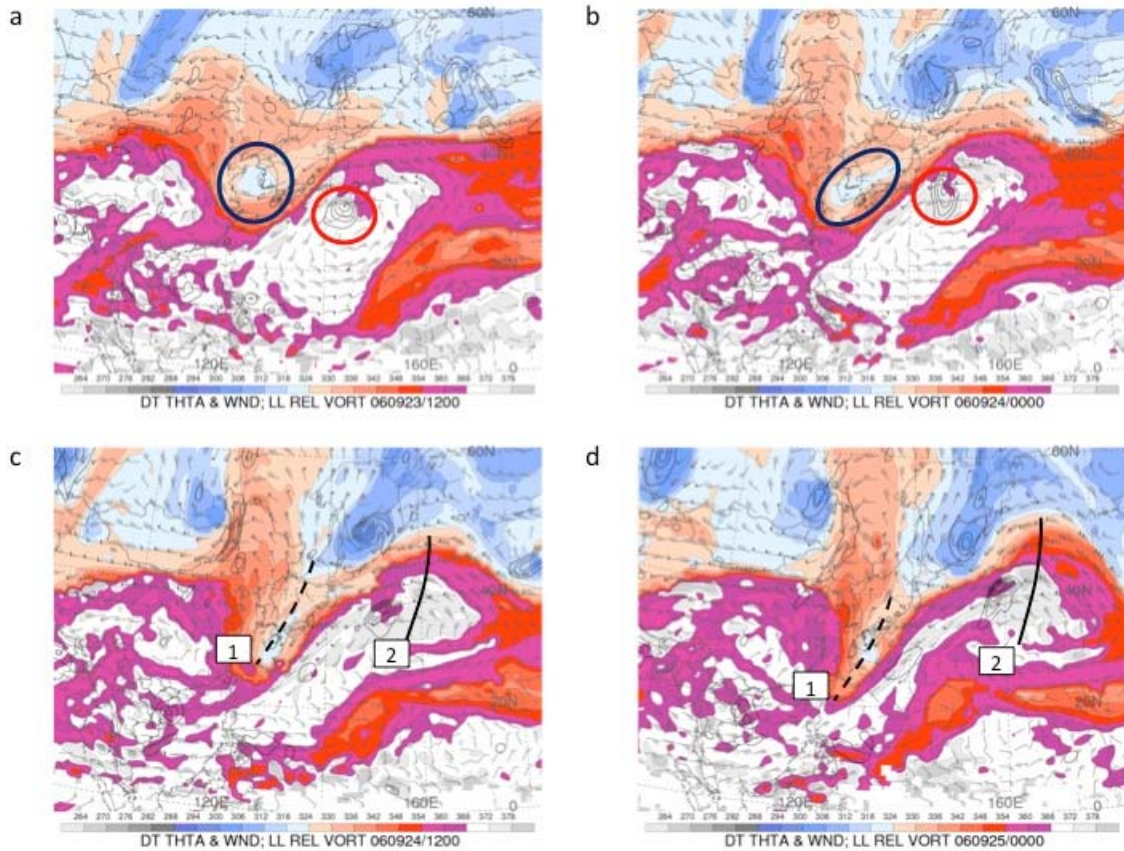


Figure 64. Same as for Figure 21, except for (a) 1200 UTC 23 Sep 2006, (b) 0000 UTC 24 Sep 2006, (c) 1200 UTC 24 Sep 2006, and (d) 0000 UTC 25 Sep 2006 (unpublished figure provided by H. Archambault).

2. Propagation Phase and Downstream Development

Moving eastward over the North Pacific, Figure 65a shows the presence of a previously existing region of low potential temperature (blue circle) downstream of the newly formed RWT. As the DRV intensifies from 0000 to 1200 UTC 25 Sep 2006, downstream development produces trough three and ridge four. The initiating DRV is now an EC as indicated by the lower-level vorticity between trough one and ridge two. This EC reaches a minimum SLP of 972 hPa at 1200 UTC 26 Sep 2006 (not shown) before occluding. With the intensifying EC, the downstream amplification of trough three and ridge four continues through 1200 UTC 26 Sep 2006 as indicated in Figure 65d.

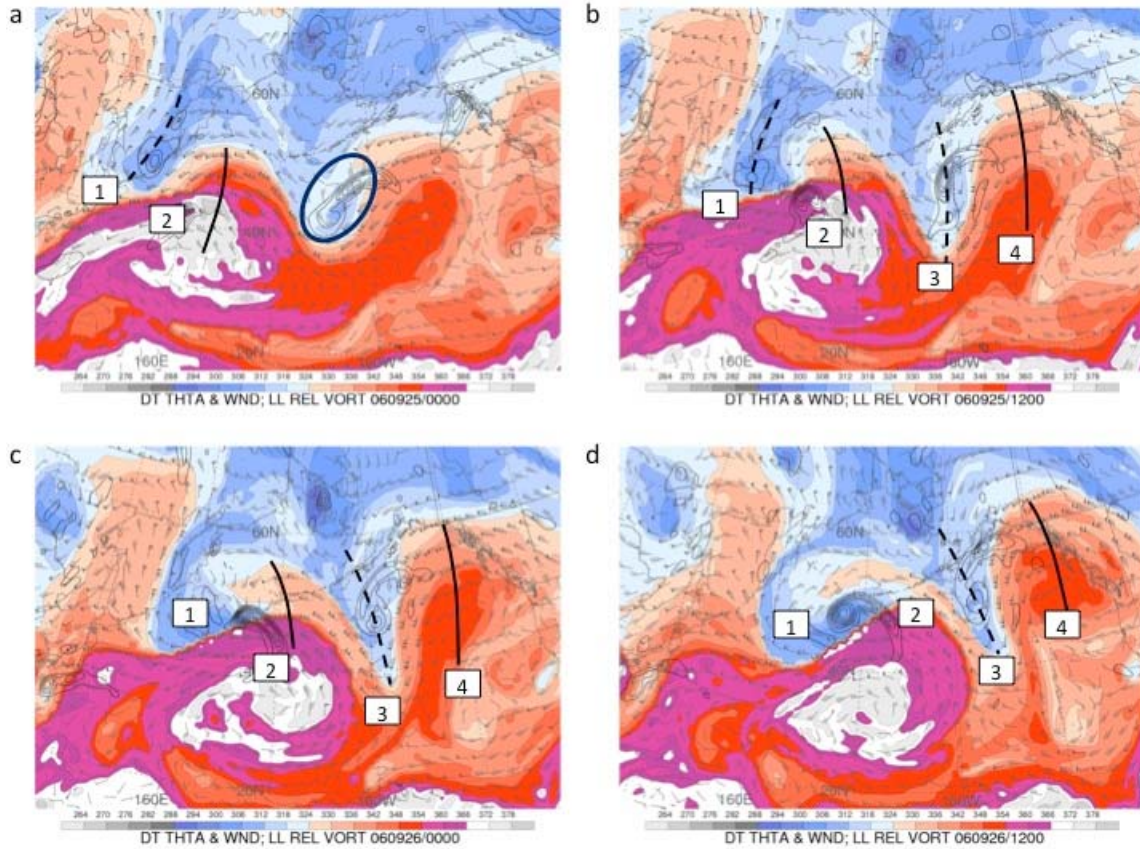


Figure 65. Same as for Figure 21, except for (a) 0000 UTC 25 Sep 2006, (b) 1200 UTC 25 Sep 2006, (c) 0000 UTC 26 Sep 2006, and (d) 1200 UTC 26 Sep 2006 (unpublished figure provided by H. Archambault).

Moving over North America at 1200 UTC 26 Sep 2006, trough three and ridge four are upstream of a relatively zonal jet over the northern U.S., as indicated by the blue circle in Figure 66a. Over the next 24 hours, ridge four continues to amplify and trough five is produced by 1200 UTC 27 Sep 2006, with subsequent downstream development of ridge six by 0000 UTC 28 Sep 2006.

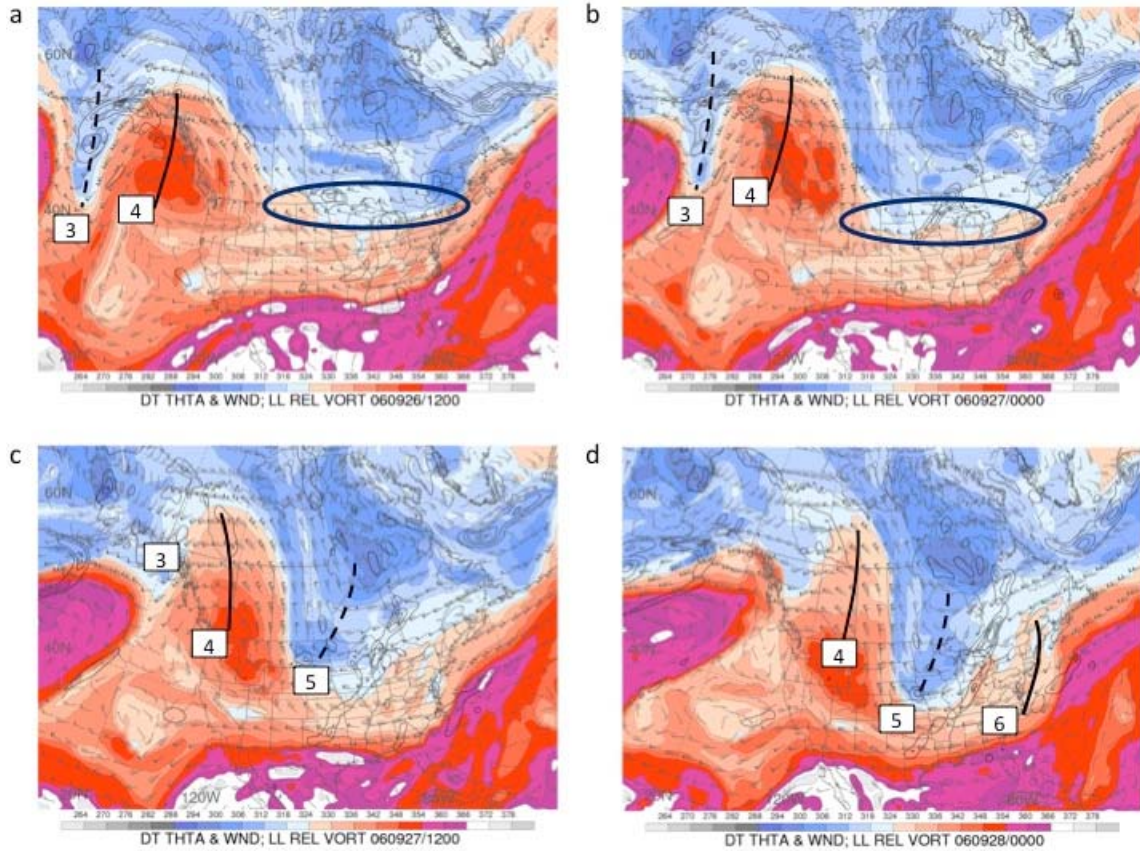


Figure 66. Same as for Figure 21, except for (a) 1200 UTC 26 Sep 2006, (b) 0000 UTC 27 Sep 2006, (c) 1200 UTC 27 Sep 2006, and (d) 0000 UTC 28 Sep 2006 (unpublished figure provided by H. Archambault).

Over the North Atlantic, trough five deepens and ridge six builds upstream of a previously existing area of low potential temperature indicated by the blue circle in Figure 67a. This area forms a cutoff low downstream of trough five and ridge six as all three features propagate eastward from 1200 UTC 28 Sep 2006 to 0000 UTC 30 Sep 2006.

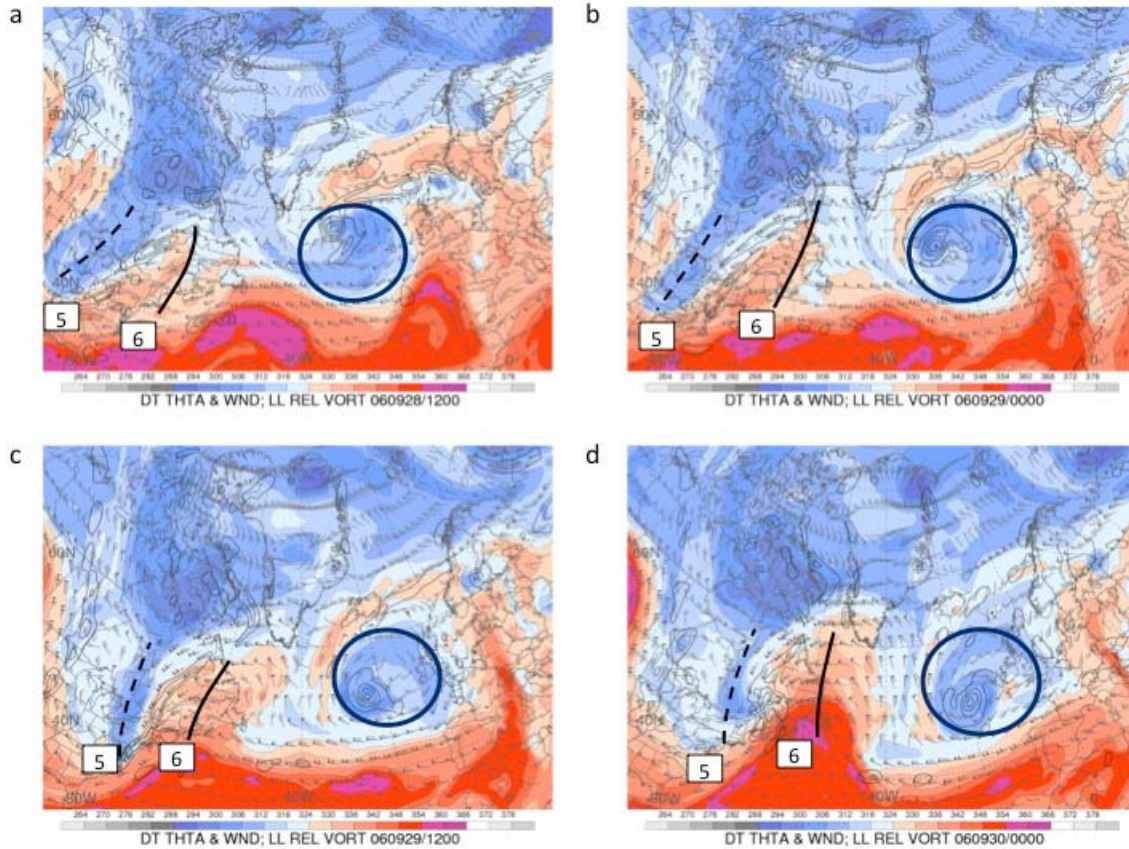


Figure 67. Same as for Figure 21, except for (a) 1200 UTC 28 Sep 2006, (b) 0000 UTC 29 Sep 2006, (c) 1200 UTC 29 Sep 2006, and (d) 0000 UTC 30 Sep 2006 (unpublished figure provided by H. Archambault).

At 1200 UTC 30 Sep 2006, an EC is present between trough five and ridge six as indicated by the lower-level vorticity. Additionally, SLP plots (not shown) indicate this EC reaches a minimum SLP of 992 hPa at 0000 01 Oct 2006. At this time Figure 68b shows further deepening of trough five, amplification of ridge six and the downstream development of trough seven. Over the next 24 hours the EC occludes and ridge six forms a cutoff high.

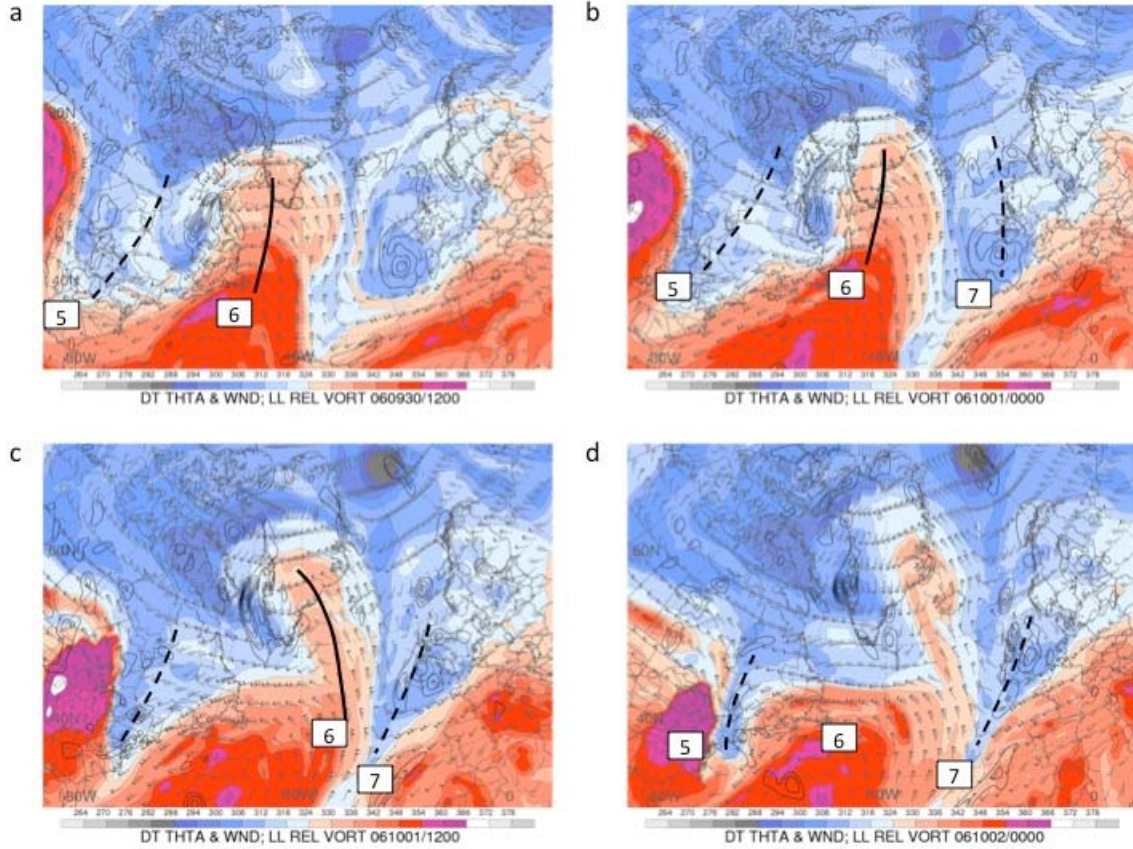


Figure 68. Same as for Figure 21, except for (a) 1200 UTC 30 Sep 2006, (b) 0000 UTC 01 Oct 2006, (c) 1200 UTC 01 Oct 2006, and (d) 0000 UTC 02 Oct 2006 (unpublished figure provided by H. Archambault).

3. Termination Phase

The RWT climatology used for this study states that RWT number 6826 ended its lifecycle at 0000 UTC 03 Oct 2006. At 1200 UTC 02 Oct 2006, Figure 69a shows trough five begins to form a cutoff low and ridge six does not amplify significantly. Over the next 12 hours, Rossby wave breaking continues, and, after the time of RWT lysis, the waveguide poleward of ridge six begins to return to a zonal orientation. At 0000 UTC 04 Oct 2006 trough seven remains but is no longer a component of a coherent packet of waves.

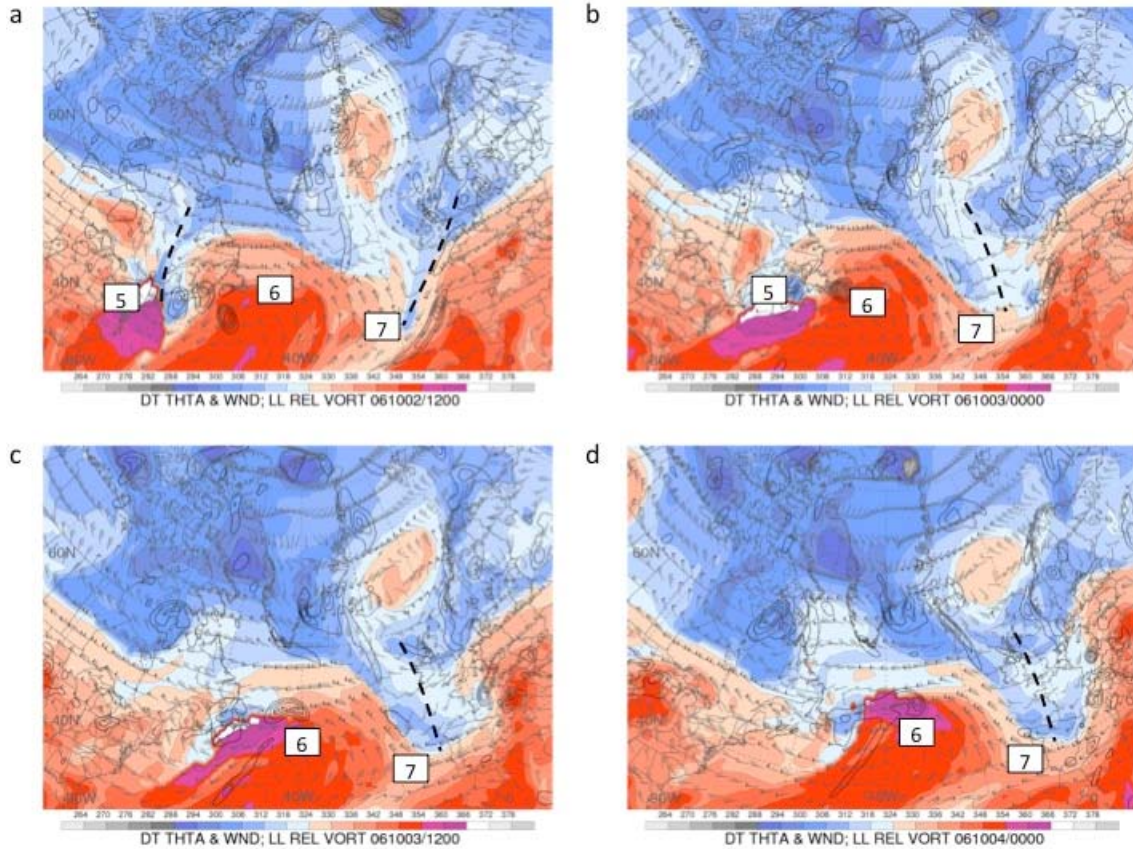


Figure 69. Same as for Figure 21, except for (a) 1200 UTC 02 Oct 2006, (b) 0000 UTC 03 Oct 2006, (c) 1200 UTC 03 Oct 2006, and (d) 0000 UTC 04 Oct 2006 (unpublished figure provided by H. Archambault).

A Hovmöller diagram of the end of the lifecycle of RWT number 6826 is presented in Figure 70. This plot was created using the same method as that defined for Figure 24, except that the meridional wind anomalies here were averaged from 40°–65°N to better capture the features of this RWT. The plot begins at 0000 UTC 23 Sep 2006 and ends at 0000 UTC 05 Oct 2006. The features indicating trough five, ridge six, and trough seven are labeled. After 0000 27 Sep 2006, ridge six and trough seven are formed via downstream development. The termination of RWT number 6826 is indicated by the decay of these features after 0000 03 Oct 2006.

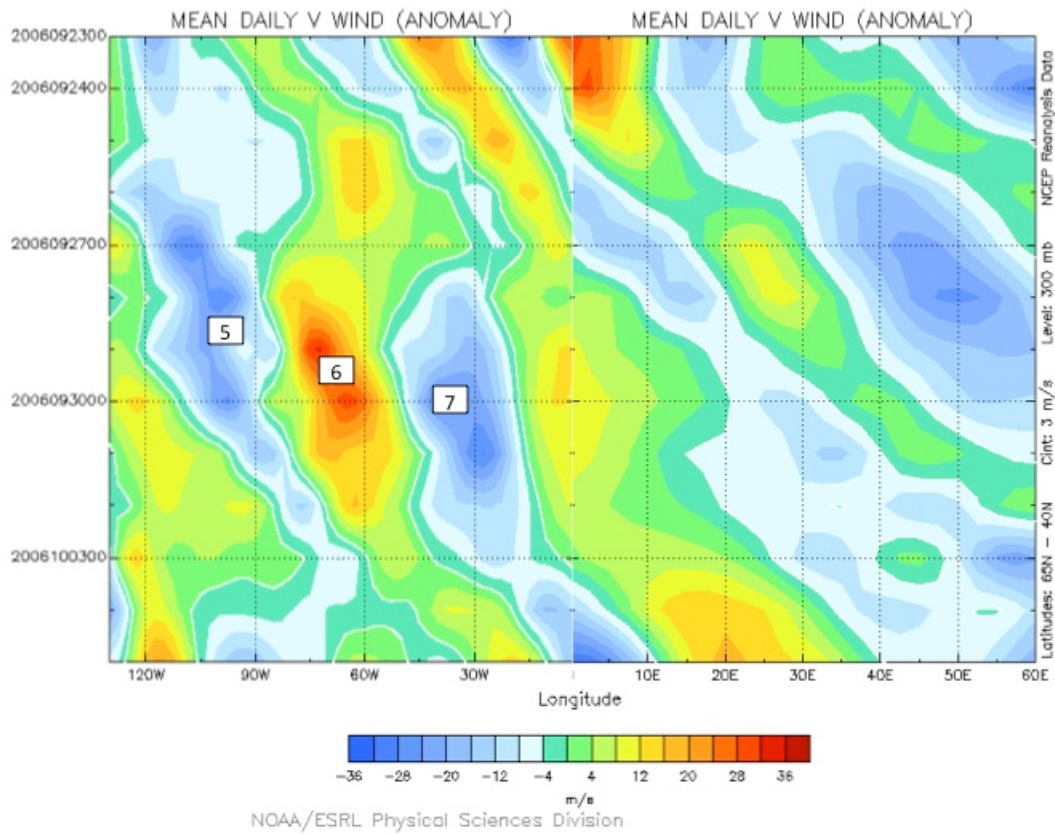


Figure 70. Same as for Figure 24 except anomalies are averaged between 40°–65°N from 0000 UTC 23 Sep 2006 to 0000 UTC 05 Oct 2006. (Image provided by the NOAA/ESRL Physical Sciences Division).

4. Sensible Weather Impacts

The downstream development of RWT number 6826 results in the previously described trough seven forming over Europe. This low reaches a central SLP of 996 hPa over the North Sea at the time of RWT decay, 0000 UTC 03 Oct 2006. This is depicted in the SLP plot in Figure 71.

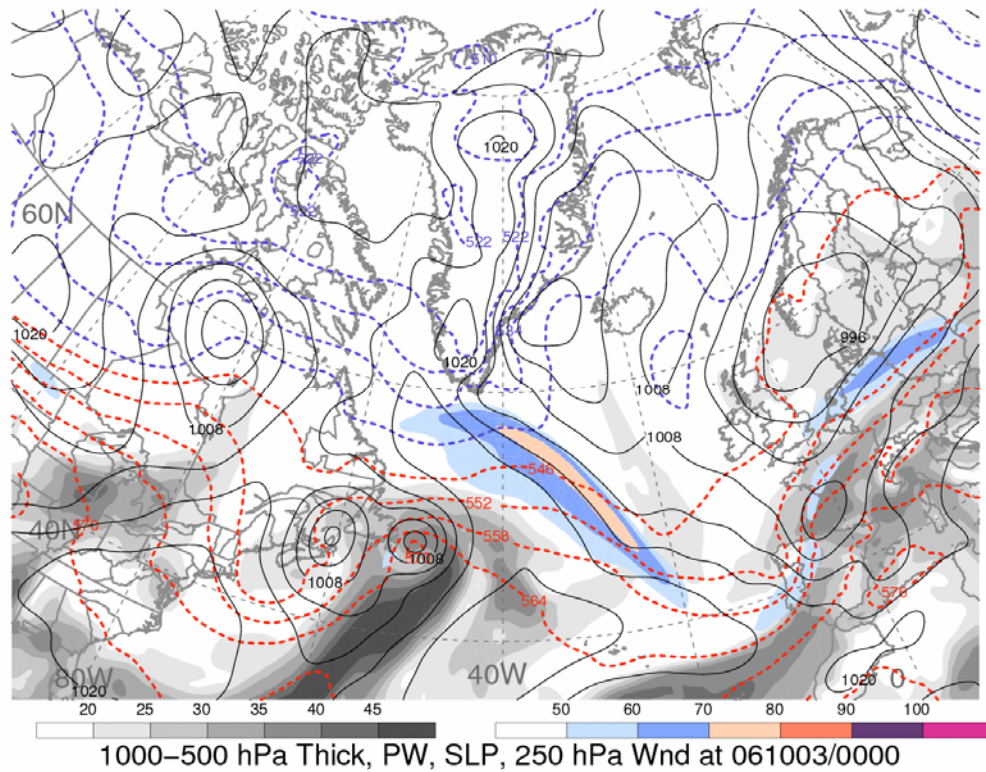


Figure 71. Same as for Figure 23, except for 0000 UTC 03 Oct 2006 (figure provided by H. Archambault).

Trough seven is responsible for negative SLP anomalies of 18 hPa as depicted in the 1-day SLP anomaly plot in Figure 71. As a result, a localized area over the North Sea shows a 1-day anomaly of 1000 hPa winds of tropical storm force (18 m s^{-1}) on 03 Oct 2006. This can be seen in the warm color shading in Figure 72. In contrast to the two previous examples in Chapter IV, the largest sensible weather impacts from RWT number 6826 occur coincident with the time of RWT decay. These conditions are a result of the downstream development of RWT number 6826 that was triggered by a DRV eight days earlier over the Western Pacific.

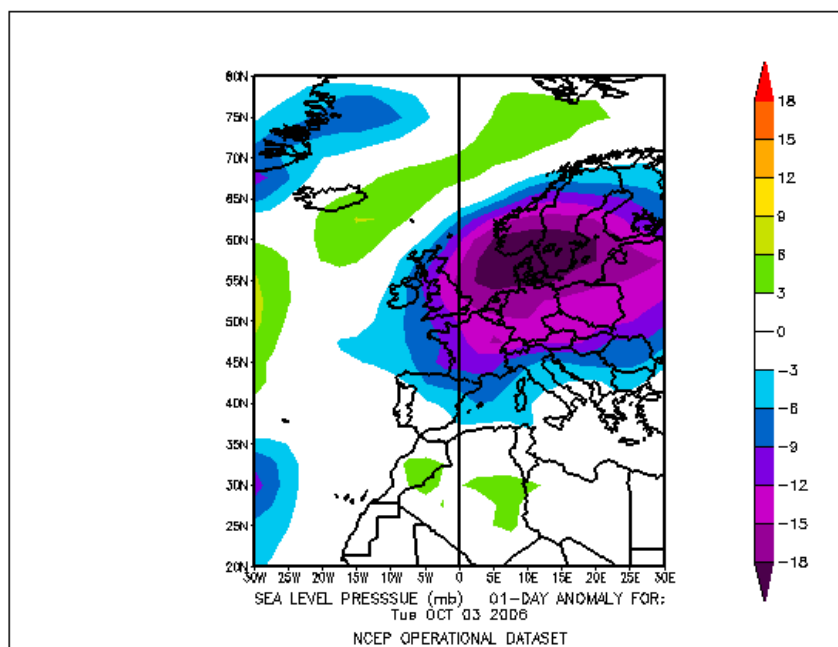


Figure 72. Same as for Figure 53, except for 03 Oct 2006. (Image provided by the NOAA/ESRL Physical Sciences Division).

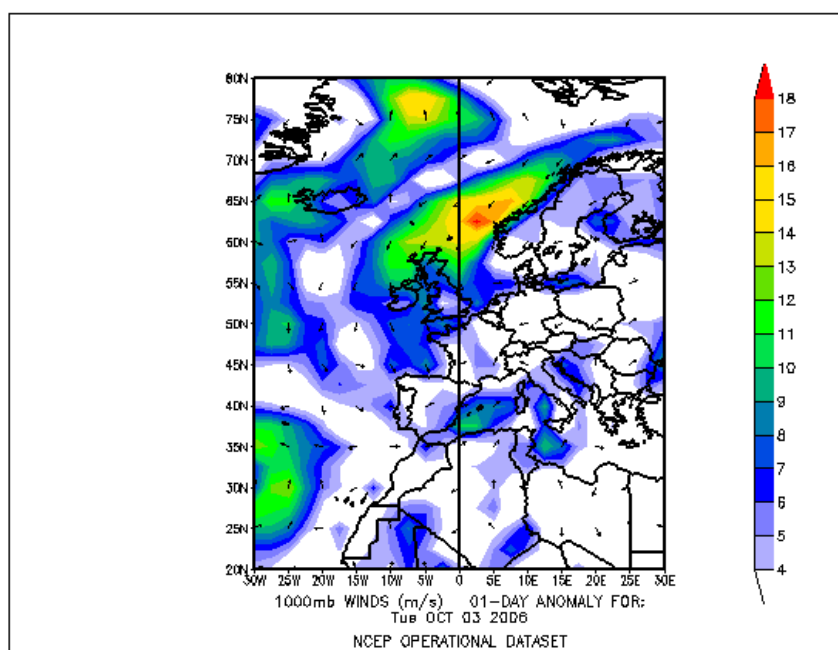


Figure 73. Same as for Figure 54, except for 03 Oct 2006. (Image provided by the NOAA/ESRL Physical Sciences Division).

D. EXTRATROPICAL TRANSITION

The final example presented in this chapter details the lifecycle of a RWT that was triggered by the ET of Hurricane Igor over the North Atlantic. This example provides an ideal representation of wave evolution during ET.

1. Triggering Phase

The RWT climatology states that RWT number 7783 was initiated at 1200 UTC 20 Sep 2010 near 75°W. A previous analysis has demonstrated the ET of Hurricane Igor triggered this RWT. In Figure 74a, Hurricane Igor is highlighted by a red circle near 60°W. Also annotated are two regions of low potential temperature (blue circles) poleward of the tropical cyclone. As Hurricane Igor tracks poleward, a region of high potential temperature air precedes it. By 0000 UTC 20 Sep 2010, the continued track of Hurricane Igor causes it to begin to interact with the upper-level features highlighted in blue. Twelve hours later the ET has initiated RWT number 7783 as evidenced by the formation of trough one, ridge two, and trough three as indicated in Figure 74d. Although an ET event, Hurricane Igor was not classified as extratropical until 1800 UTC 21 Sep 2010, according to the NHC Tropical Cyclone Report (Pasch and Kimberlain 2011). This indicates Igor was in the transformation stage of ET (Klein et al. 2000) prior to RWT triggering.

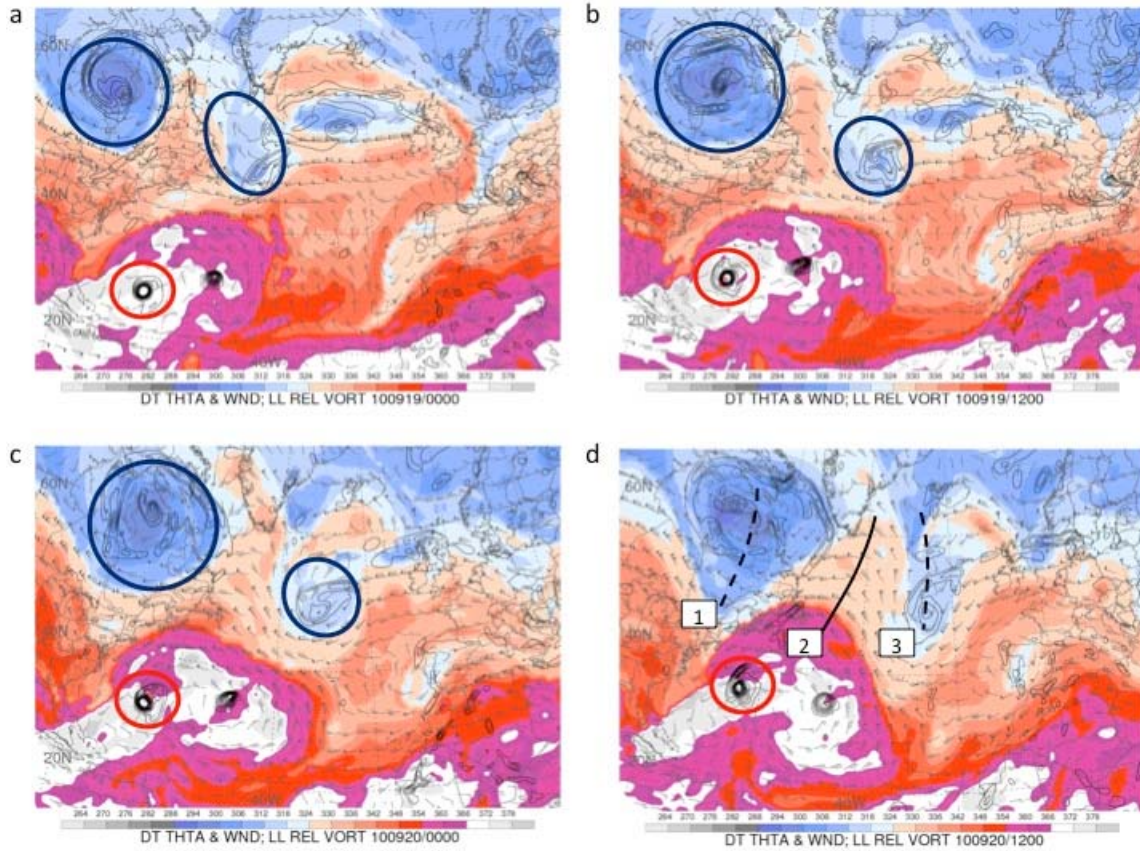


Figure 74. Same as for Figure 21, except for (a) 0000 UTC 19 Sep 2010, (b) 1200 UTC 19 Sep 2010, (c) 0000 UTC 20 Sep 2010, and (d) 1200 UTC 20 Sep 2010 (unpublished figure provided by H. Archambault).

2. Propagation Phase and Downstream Development

Figure 75a shows the lower-level vorticity signature of the transitioning cyclone between trough one and ridge two at 0000 UTC 21 Sep 2010. At this time, the central SLP of Igor is 950 hPa (Pasch and Kimberlain 2011). Following this time, the central pressure of the storm falls to 950 hPa as it enters the reintensification stage of its ET (Klein et al. 2000). This intensification builds ridge two by 1200 UTC 21 Sep 2010 as indicated in Figure 75b. Simultaneously, trough three deepens and ridge four develops downstream. The transitioning storm is now an EC. Over the next 24 hours the EC occludes and ridge two build significantly. Downstream, trough three deepens and ridge four builds.

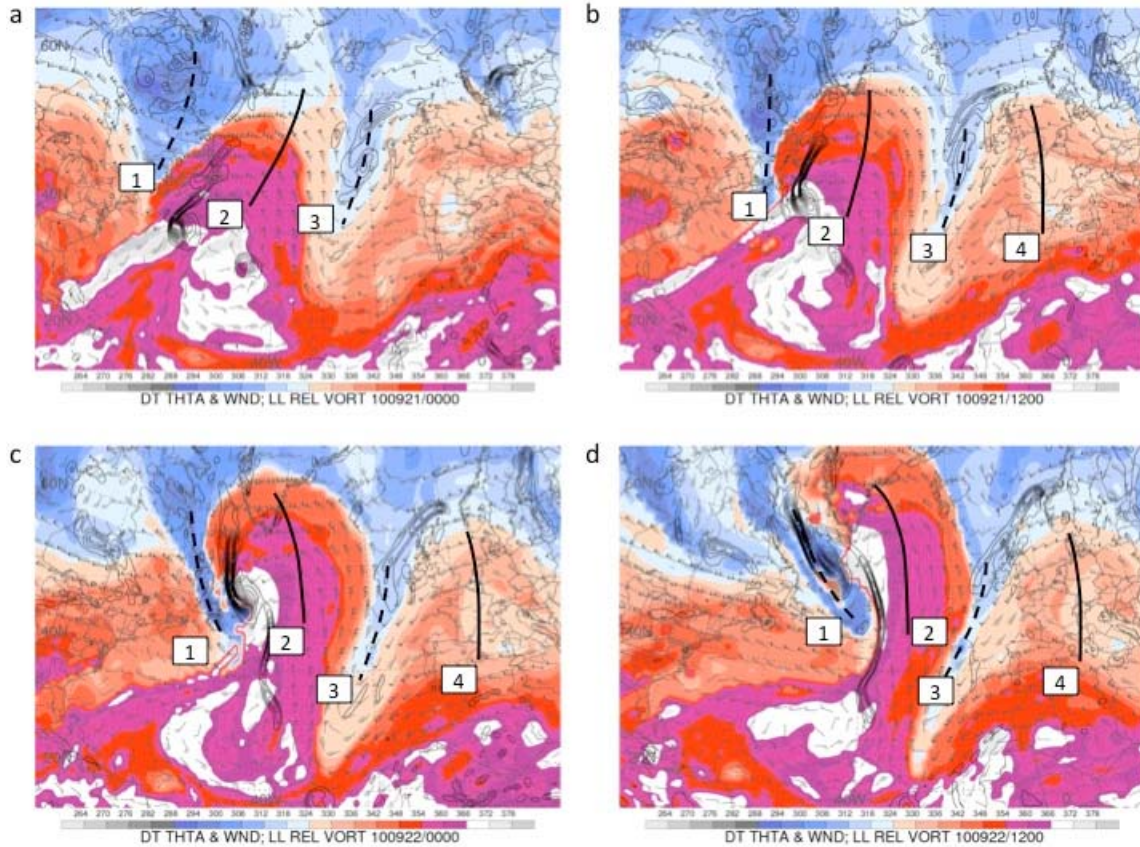


Figure 75. Same as for Figure 21, except for (a) 0000 UTC 21 Sep 2010, (b) 1200 UTC 21 Sep 2010, (c) 0000 UTC 22 Sep 2010, and (d) 1200 UTC 22 Sep 2010 (unpublished figure provided by H. Archambault).

By 0000 UTC 23 Sep 2010, Figure 76a illustrates the further amplification of ridge two and the deepening of trough three into a narrow filament extending equatorward. Twelve hours later the equatorward portion of trough three has formed a cutoff low. Concurrently, trough one continues to propagate eastward while ridge two does not amplify further. From 0000 to 1200 UTC 24 Sep 2006, the trough ridge pattern of the RWT becomes highly amplified as the individual features pack together zonally. This is indicated in Figure 76d as trough one is no longer distinguishable.

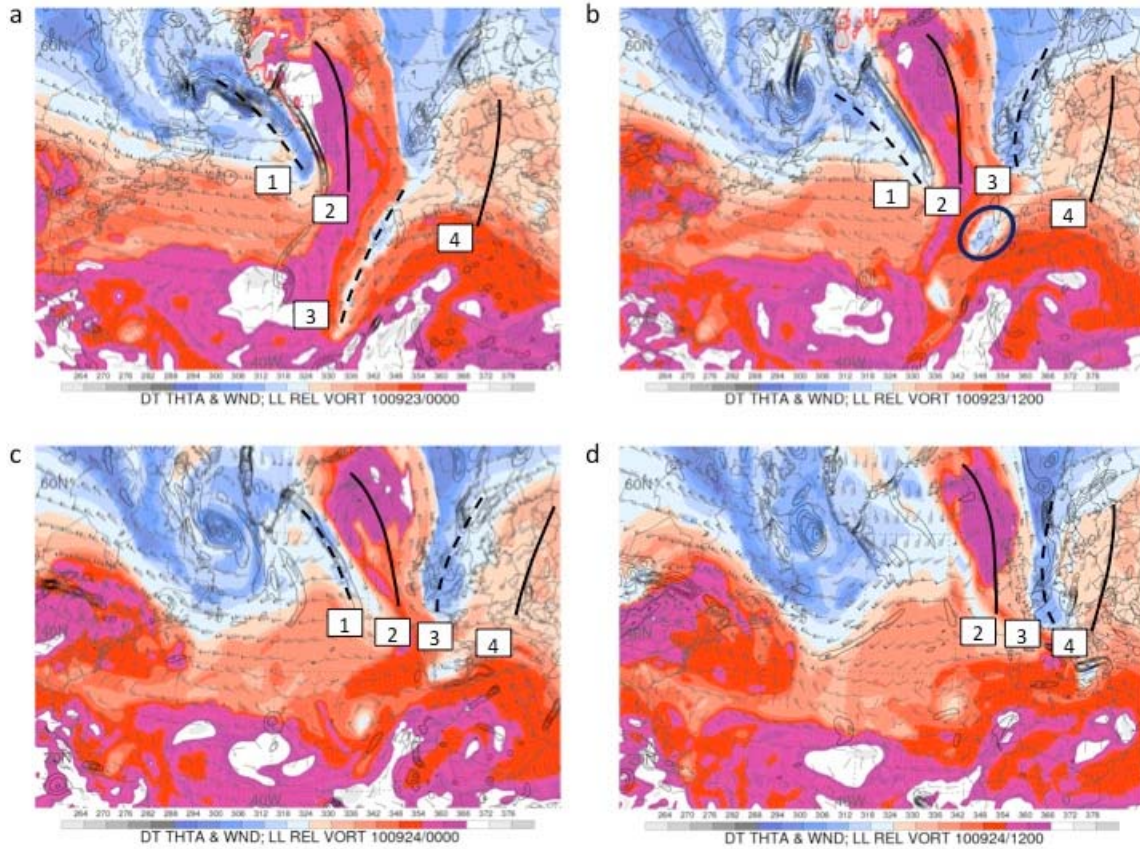


Figure 76. Same as for Figure 21, except for (a) 0000 UTC 23 Sep 2010, (b) 1200 UTC 23 Sep 2010, (c) 0000 UTC 24 Sep 2010, and (d) 1200 UTC 24 Sep 2010 (unpublished figure provided by H. Archambault).

3. Termination Phase

The RWT climatology states that RWT number 7783 ended its lifecycle at 0000 26 Sep 2010. At 0000 UTC 25 Sep 2010 the highly amplified ridge-trough pattern of the RWT is discernable in Figure 77a as ridge two, trough three, and ridge four propagate downstream. In the following 24 hours, Rossby wave breaking ensues and by 0000 UTC 26 Sep 2010 the features of RWT number 7783 are no longer apparent. A region of high potential temperature gradient results from the wave-breaking event and is highlighted in Figure 77c (blue circle).

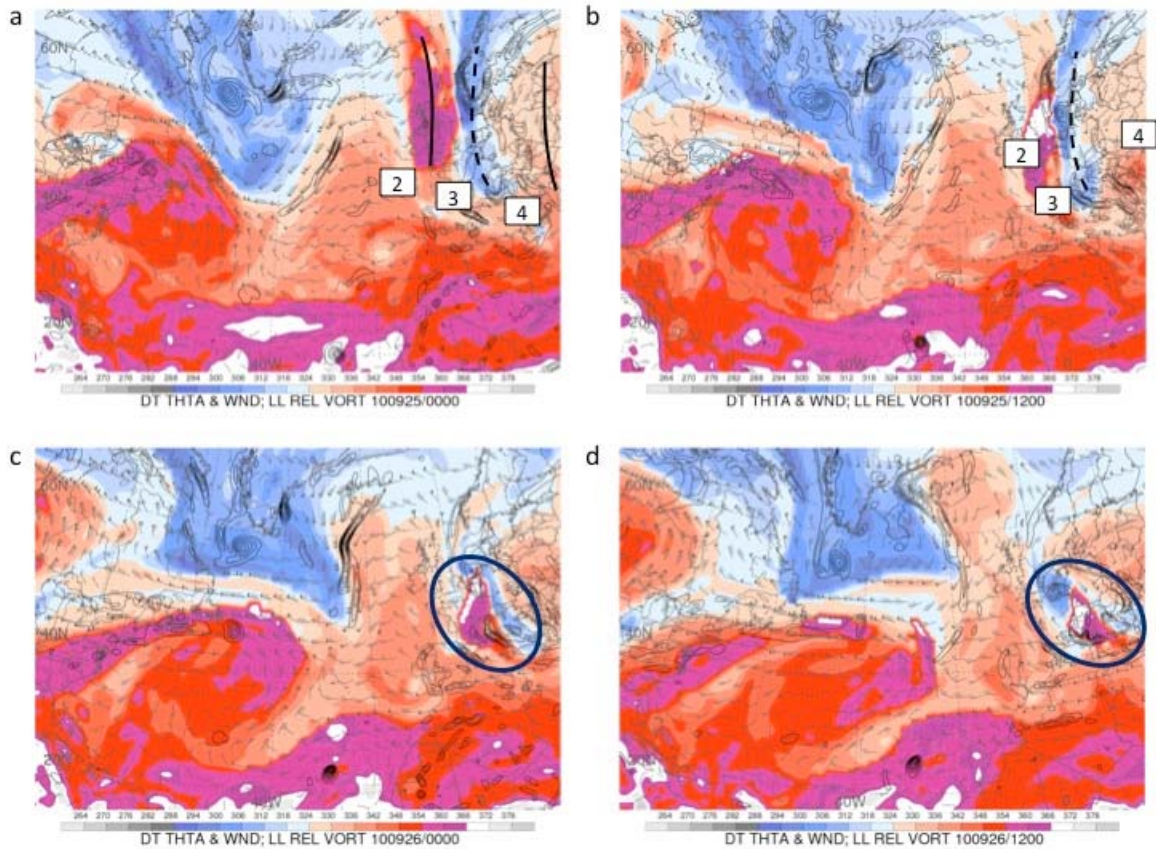


Figure 77. Same as for Figure 21, except for (a) 0000 UTC 25 Sep 2010, (b) 1200 UTC 25 Sep 2010, (c) 0000 UTC 26 Sep 2010, and (d) 1200 UTC 26 Sep 2010 (unpublished figure provided by H. Archambault).

A Hovmöller diagram of the lifecycle of RWT number 7783 is presented in Figure 78. This plot was created using the same method as that defined for Figure 24, except that the meridional wind anomalies here were averaged from 45°–65°N to better capture the features of this RWT. At 0000 UTC 19 Sep 2010 the precursor to ridge two begins to amplify with the initial poleward trajectory of Hurricane Igor. Twelve hours after the initiation of the RWT, ridge two is further amplified as the transitioning cyclone begins to enter the reintensification stage (Klein et al. 2000). Trough three and ridge four develop downstream and the eastward propagation of the RWT is evident. Near 0000 UTC 26 Sep 2010, the decay of trough three marks the end of the lifecycle of RWT number 7783.

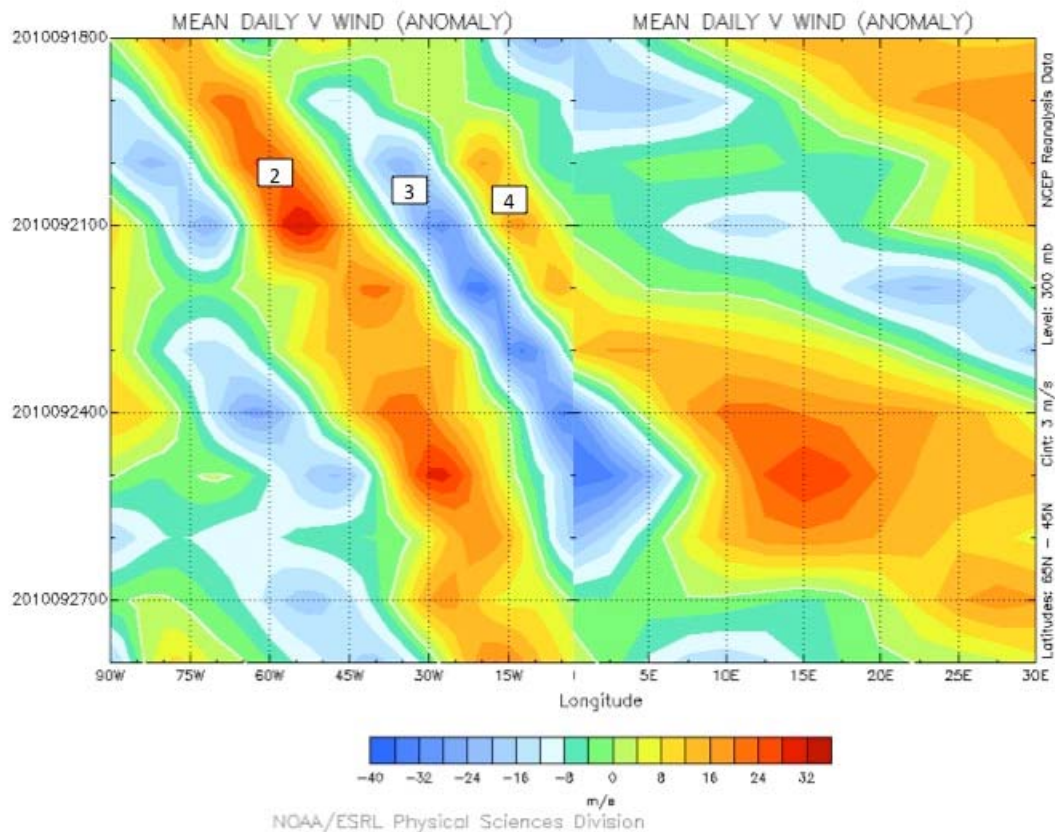


Figure 78. Same as for Figure 24 except anomalies are averaged between 45°–65°N from 0000 UTC 18 Sep 2010 to 0000 UTC 28 Sep 2010. (Image provided by the NOAA/ESRL Physical Sciences Division).

4. Sensible Weather Impacts

The ET of Hurricane Igor and subsequent downstream development of the ensuing RWT result in the formation of a low over Europe associated with trough three. At 0000 UTC 26 Sep 2010, the SLP plot shown in Figure 79 indicates this feature reaches a minimum SLP of 996 hPa east of the Adriatic Sea.

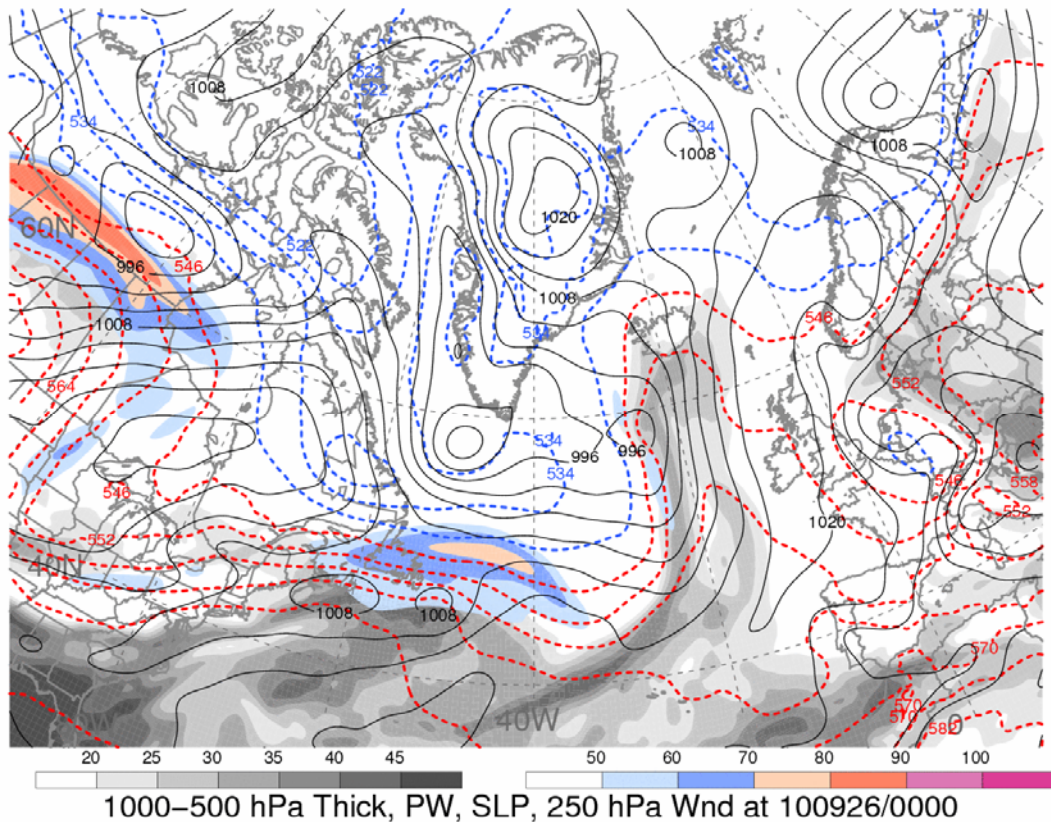


Figure 79. Same as for Figure 23, except for 0000 UTC 26 Sep 2010 (figure provided by H. Archambault).

Although the SLP plot does not indicate a significantly low central pressure associated with this system, a large region of high SLP anomaly exists over Northern Europe as indicated by the region of warmer colors on the 1-day SLP anomaly plot for 26 Sep 2010 presented in Figure 80. The low SLP anomaly resulting from the downstream development of RWT number 7783 is indicated by cooler colors. There exists a strong gradient between these two features resulting in anomalous easterly winds approaching 17 m s^{-1} over the North Sea as indicated by the 1-day 1000 hPa wind anomaly plot for 26 Sep 2010 shown in Figure 81. Additionally, anticyclonic flow around the anomalous high generates near-tropical storm force winds south of Iceland.

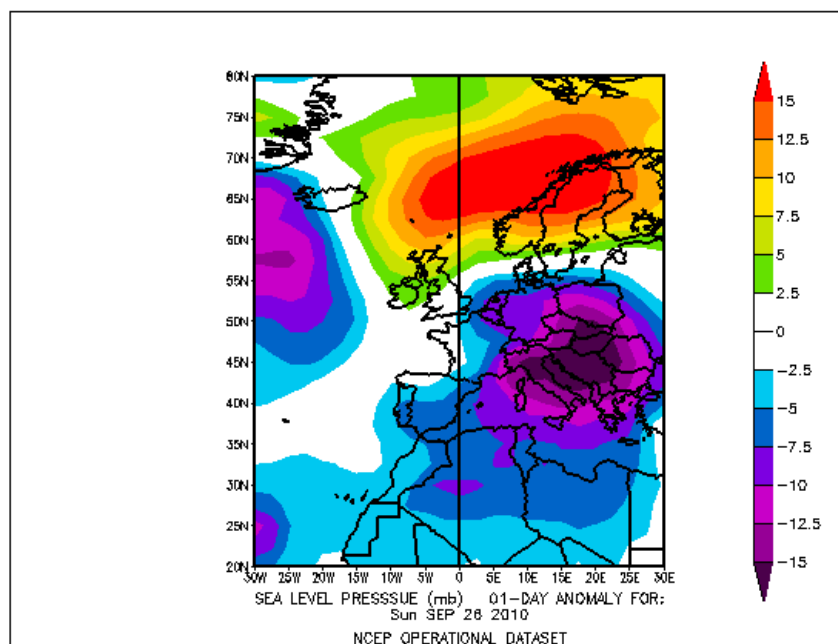


Figure 80. Same as for Figure 53, except for 26 Sep 2010. (Image provided by the NOAA/ESRL Physical Sciences Division).

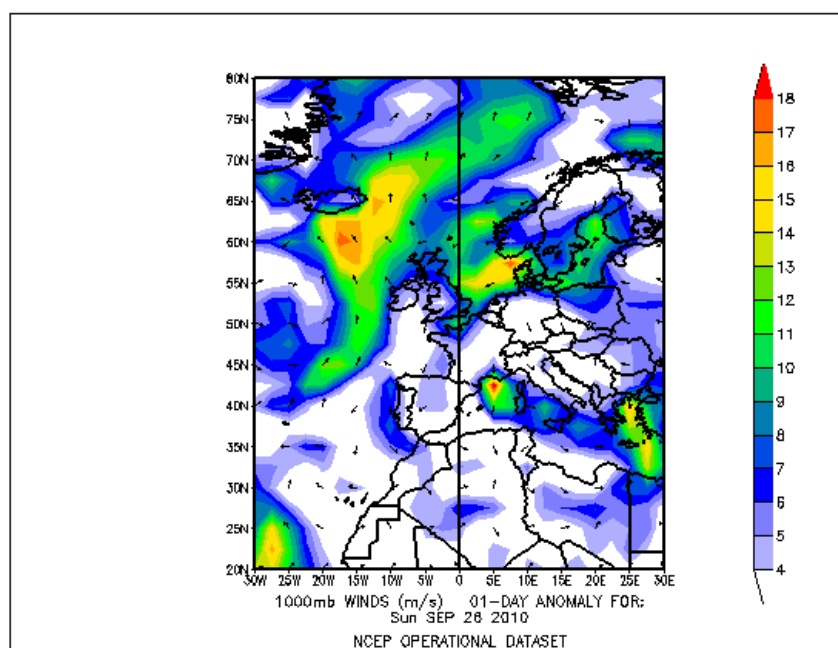


Figure 81. Same as for Figure 54, except for 26 Sep 2010. (Image provided by the NOAA/ESRL Physical Sciences Division).

THIS PAGE INTENTIONALLY LEFT BLANK

V. STATISTICS OF ROSSBY WAVE TRAIN TRIGGERS

A. TOTAL NUMBERS OF ROSSBY WAVE TRAIN TRIGGERS

A detailed analysis of the 38 RWTs in Table 1 subjectively determined which of the four triggering mechanisms presented was responsible for each RWT initiation. The breakdown of triggering events is presented in Figure 82. Although the majority of RWTs in this subset were triggered by WCBs, due to the small sample size used, no broad conclusions about triggering mechanisms for the larger RWT climatology can be made. Table 4 lists the total number and percentage of RWTs initiated by each triggering mechanism.

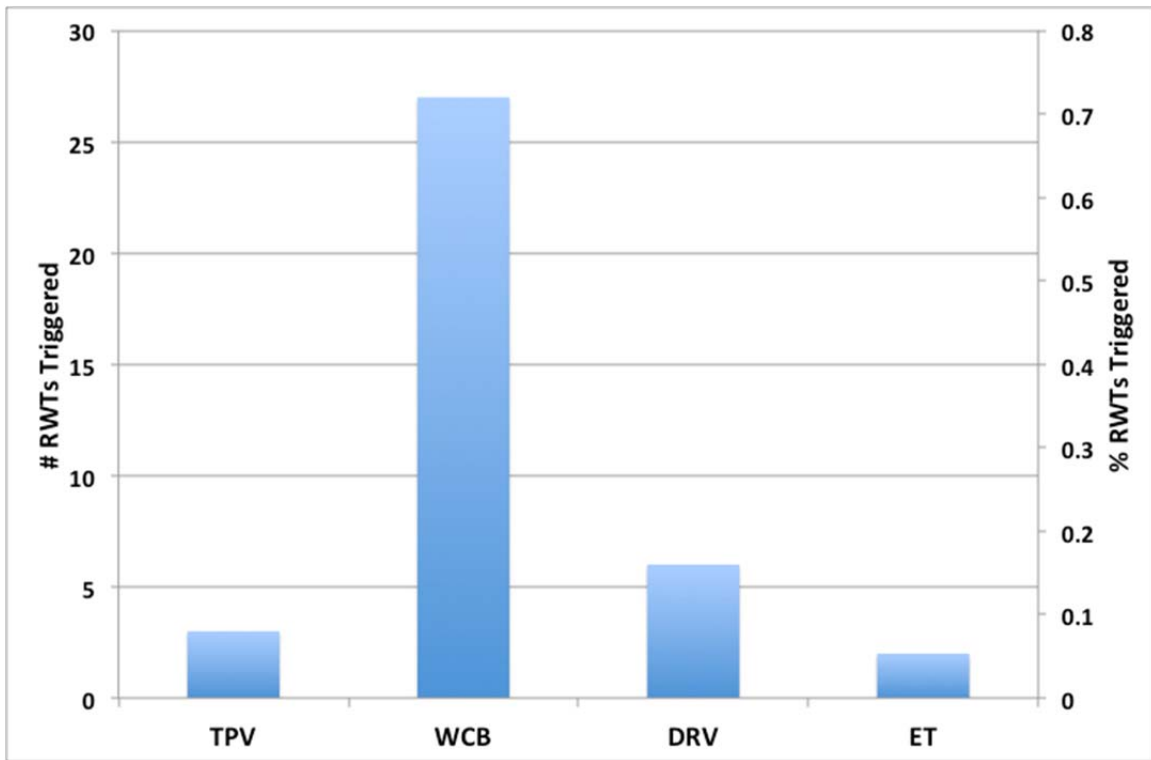


Figure 82. Histogram of the number (left axis) and percentage (right axis) of RWTs listed in Table 1 initiated by each of the four triggering mechanisms.

	TPV	WCB	DRV	ET
Number	3	27	6	2
Percentage	8	71	16	5

Table 4. Number and percentage of RWTs initiated by each triggering mechanism.

B. LONGITUDINAL VARIATIONS AND FREQUENCY OF ROSSBY WAVE TRAIN TRIGGERS

Figure 83 shows a longitudinal breakdown of the triggering mechanisms associated with each of the 38 RWTs analyzed. The longitudes associated with each RWT trigger are taken from the RWT initiation longitude provided in the ERA-Interim derived climatology provided by GW13. As the climatology used properties averaged between 20° and 80°N to identify the RWT, the latitudes of each marker in Figure 83 differ only so that markers do not overlap. They do not represent the latitudes of RWT initiation.

Two features are readily apparent in Figure 83. Although WCB initiations are concentrated over North American and the North Atlantic, they are present from roughly 110°E to the Greenwich meridian. The fact that RWTs triggered across this wide range of longitudes all terminated over Europe attests to the significant role RWTs can play in the downstream development of sensible weather impacts over Europe. Second, at least one type of each trigger is present over the North Atlantic. Again, given the small sample size used, this variability in triggers over the region of interest bolsters the theory that all four triggering mechanisms are likely to occur over the North Atlantic in the fall.

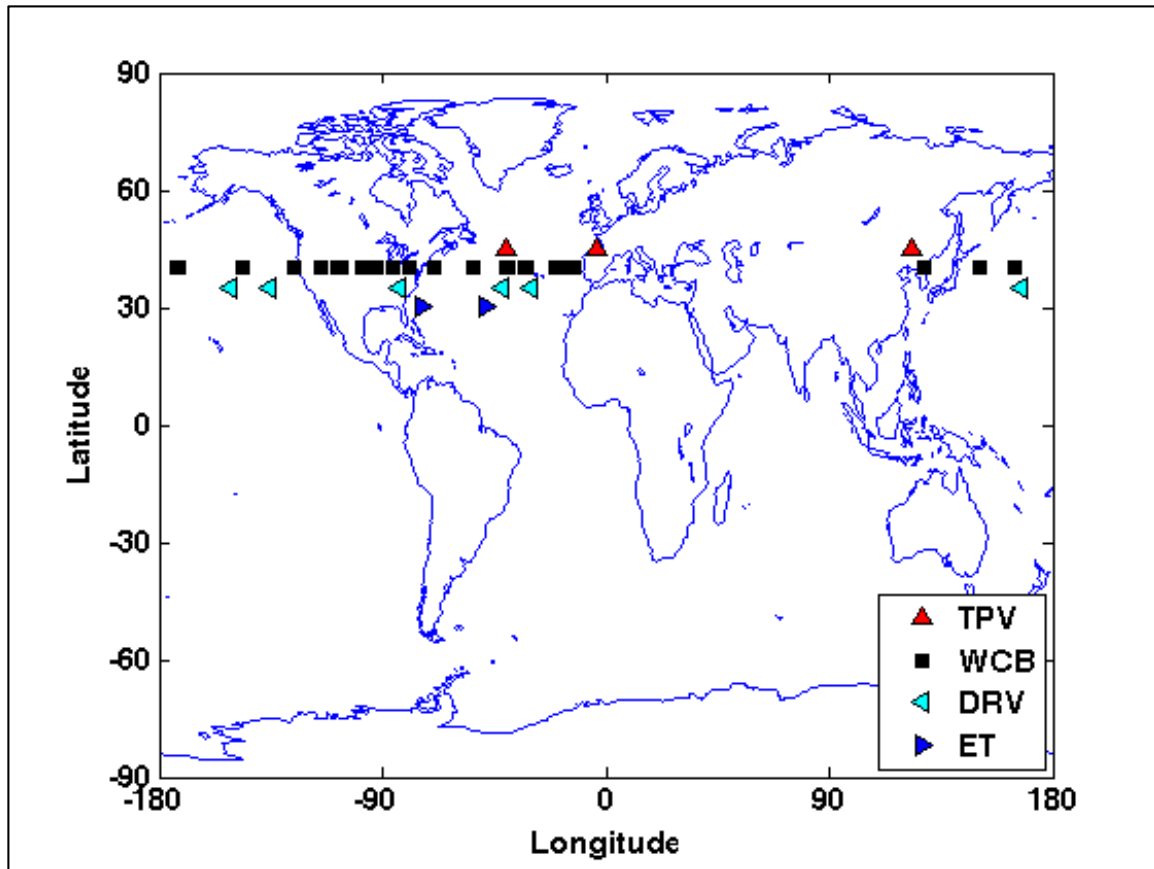


Figure 83. Longitudinal breakdown of RWT triggers as indicated by RWT starting locations from the Glatt and Wirth climatology.

To ascertain the relative frequency of RWTs triggered by longitude, Figure 84 shows the sum of RWTs triggered in longitude bins 10° wide. Blue bars represent the number of RWTs from the subset analyzed that were initiated within each bin. The data show a clear peak in the number of RWTs triggered over the North Atlantic and that all these RWTs decayed over Europe.

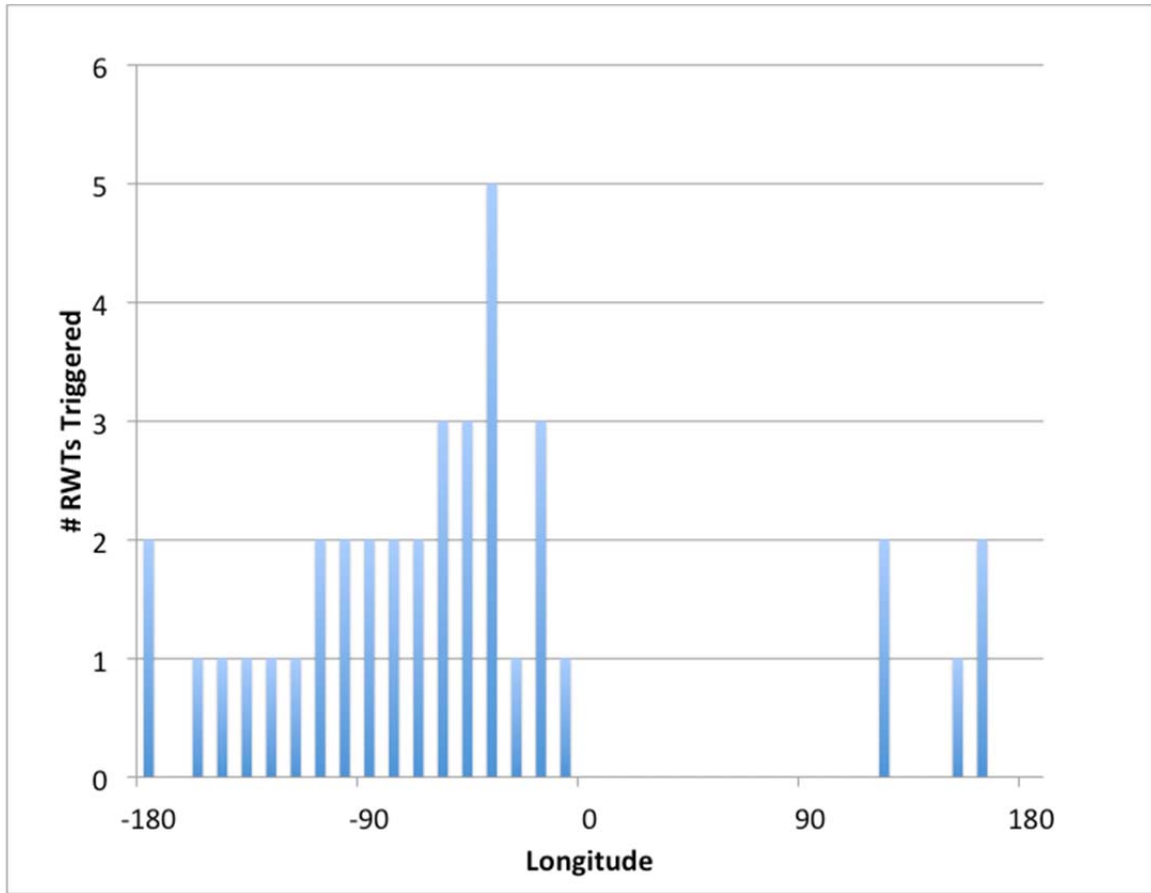


Figure 84. Number of RWTs initiated by longitude. Longitude bins are 10° wide.

There are several reasons for the peak in Figure 84. According to Madonna et al. (2014), WCBs associated with ECs occur more often in winter in the Northern Hemisphere. As the Northern Hemisphere moves from summer through fall, Madonna et al. (2014) further state that the initiation latitudes of WCBs move poleward, increasing the interaction between WCBs and the midlatitude waveguide. Also at this time, increasing baroclinicity in the North Atlantic results in more frequent WCB generation, leading up to a local maximum in winter.

Kew et al. (2010) state that a concentration of TPV tracks lies north of the entrance region of the North Atlantic jet. This proximity allows for interactions between, and perturbations of, the midlatitude jet by TPVs. BW13 shows that DRVs play a statistically significant role as precursors to explosive cyclogenesis in the North Atlantic. Furthermore, this role becomes more significant from September to October.

Additionally, the intensification of the North Atlantic tropical cyclone season during this period means there is a greater likelihood of RWTs being triggered by all four mechanisms over the North Atlantic during fall.

THIS PAGE INTENTIONALLY LEFT BLANK

VI. SUMMARY AND CONCLUSIONS

The overall goal of this research was to offer some insight into the relative frequency of occurrence of RWTs triggered by each of four waveguide perturbation mechanisms. These mechanisms included TPVs, WCBs associated with ECs, DRVs, and the ET of tropical cyclones. This research was focused to only analyze RWTs whose life cycles terminated over Europe and elicited downstream development there. This was done primarily to help align this research with the observational design of the experiment proposed for September and October of 2016.

From a climatology of objectively identified RWTs, thirty-eight were selected for detailed analysis. A subjective analysis of each was performed using various resources, including DT, SLP, and IW maps. These maps allowed the identification of a single triggering mechanism for each RWT. Of the 38 RWTs analyzed, three were triggered by TPVs, 27 by WCBs associated with ECs, six by DRVs, and 2 by the ET of TCs.

This research shows that for even a small set of RWTs, triggering events occur from the Western Pacific to the North Atlantic. While WCBs dominated the triggering events of RWTs in this subset (71%), this fact cannot be extended to the larger RWT climatology due to the small sample size presented here. Though this research did not limit the initiation region for RWTs, it does confirm that, at least for the subset analyzed here, RWTs were triggered by all mechanisms over the North Atlantic with a greater frequency than elsewhere in the Northern Hemisphere. This conclusion further supports the design proposed for the upcoming experiment.

One limitation of this study is the subjective nature of the triggering mechanism analysis performed. As the identification of upper-level features on various maps and the determination of upper-level support for lower-level features are open to interpretation, so are the determinations of RWT triggers presented here. This limitation was countered through the application of a rigorous methodology, and the results of this investigation are consistent with accepted climatologies for individual triggering mechanisms. Subsequent to this research, future investigations into creating an objective methodology

for determining RWT triggering mechanisms could prove useful in assessing the role of individual triggering mechanisms in the downstream development of sensible weather impacts.

LIST OF REFERENCES

- Archambault, H. M., L. F. Bosart, D. Keyser, and J. M. Cordeira, 2013: A climatological analysis of the extratropical flow response to recurving western North Pacific tropical cyclones. *Mon. Wea. Rev.*, **141**, 2325–2346.
- _____, H. M., cited 2014: GFS analysis archive. [Available online at www.met.nps.edu/~hmarcham/]
- Boettcher, M., and H. Wernli, 2011: Life cycle study of a diabatic Rossby wave as a precursor to rapid cyclogenesis in the North Atlantic—dynamics and forecast performance. *Mon. Wea. Rev.* **139**, 1861–1878.
- _____, and _____, 2013: A 10-yr climatology of diabatic Rossby waves in the Northern Hemisphere. *Mon. Wea. Rev.*, **141**, 1139–1154.
- Cavallo, S. M., and G. J. Hakim, 2009: Potential vorticity diagnosis of a tropopause polar cyclone. *Mon. Wea. Rev.*, **137**, 1358–1371.
- Chagnon, J. M., S. L. Gray, and J. Methven, 2013: Diabatic processes modifying potential vorticity in a North Atlantic cyclone. *Quart. J. Roy. Meteor. Soc.*, **139**, 1270–1282.
- Chang, E. K. M., 1993: Downstream development of baroclinic waves as inferred from regression analysis. *J. Atmos. Sci.*, **50**, 2038–2053.
- Eckhardt, S., A. Stohl, H. Wernli, P. James, C. Forster, and N. Spichtinger, 2004: A 15-year climatology of warm conveyor belts. *J. Climate*, **17**, 218–237.
- Glatt, I., and V. Wirth, 2013: Identifying Rossby wave trains and quantifying their properties. *Quart. J. Roy. Meteor. Soc.* **140**, 384–396.
- Grams, C., H. Wernli, M. Bottcher, J. Campa, U. Corsmeier, S. Jones, J. Keller, C. Lenz, and L. Wiegand, 2011. The key role of diabatic processes in modifying the upper-tropospheric wave guide: A North Atlantic case-study. *Quart. J. Roy. Meteor. Soc.* **137**, 2174–2193.
- Hakim, G. J. and A. K. Canavan, 2005: Observed cyclone–anticyclone tropopause vortex asymmetries. *J. Atmos. Sci.*, **62**, 231–240.
- Jones, S. C., P. A. Harr, J. Abraham, L. F. Bosart, P. J. Bowyer, J. L. Evans, D. E. Hanley, B. N. Hanstrum, R. E. Hart, F. Lalaurette, M. R. Sinclair, R. K. Smith, and C. Thorncroft, 2003: The extratropical transition of tropical cyclones: Forecast challenges, current understand, and future directions. *Wea. Forecasting*, **18**, 1052–1092.

- Kew, S. F., M. Sprenger, and H. C. Davies, 2010: Potential vorticity anomalies of the lowermost stratosphere: A 10-yr winter climatology. *Mon. Wea. Rev.*, **138**, 1234–1249.
- Klein, P. M., P. A. Harr, and R. L. Elsberry, 2000: Extratropical transition of western North Pacific tropical cyclones: An overview and conceptual model of the transformation stage. *Wea. Forecasting*, **15**, 373–395.
- Lee, S., and I. Held, 1993: Baroclinic wave packets in models and observations. *J. Atmos. Sci.*, **50**, 1413–1428.
- Madonna, E., H. Wernli, and H. Joos, 2014: Warm conveyor belts in the ERA-Interim dataset (1979–2010). Part I: climatology and potential vorticity evolution. *J. Climate*, **27**, 3–26.
- Moore, R. W., and M. T. Montgomery, 2004: Reexamining the dynamics of short-scale, diabatic Rossby waves and their role in midlatitude moist cyclogenesis. *J. Atmos. Sci.*, **61**, 754–768.
- _____, and _____, and H. C. Davies, 2008: The integral role of a diabatic Rossby vortex in a heavy snowfall event. *Mon. Wea. Rev.*, **136**, 1878–1897.
- Nielsen-Gammon, J., 2001: A visualization of the global dynamic tropopause. *Bull. Amer. Meteor. Soc.*, **82**, 1151–1167.
- Parker, D. J., and A. J. Thorpe, 1995: Conditional convective heating in a baroclinic atmosphere: A model of convective frontogenesis. *J. Atmos. Sci.*, **52**, 1699–1711.
- Pasch, R. J. and T. B. Kimberlain, 2011: Tropical cyclone report hurricane Igor. NHC Rep. AL112010, 20 pp.
- Petterssen S. and S. J. Smebye, 1971: On the development of extratropical cyclones. *Quart. J. Roy. Meteor. Soc.*, **97**, 457–482.
- Raymond, D. J. and H. Jiang, 1990: A theory for long-lived mesoscale convective systems. *J. Atmos. Sci.*, **47**, 3067–3077.
- Riemer, M., S. C. Jones, and C. A. Davis, 2008: The impact of extratropical transition on the downstream flow: An idealized modeling study with a straight jet. *Quart. J. Roy. Meteor. Soc.*, **134**, 69–91.
- Sanders, F. and J. R. Gyakum, 1980: Synoptic-dynamic climatology of the “Bomb.” *Mon. Wea. Rev.*, **108**, 1589–1606.
- Schwierz, C., S. Dirren, and H. C. Davies, 2004: Forced waves on a zonally aligned jet stream. *J. Atmos. Sci.*, **61**, 73–87.

- Snyder, C. and R. S. Lindzen, 1991: Quasi-geostrophic wave-CISK in an unbounded baroclinic shear. *J. Atmos. Sci.*, **48**, 76–86.
- Wernli, H., S. Dirren, M. Liniger, and M. Zillig, 2002: Dynamical aspects of the life cycle of the winter storm “Lothar” (24–26 December 1999). *Quart. J. Roy. Meteor. Soc.*, **128**, 405–429.
- _____, and H. C. Davies, 1997: A lagrangian-based analysis of extratropical cyclones. I: The method and some applications. *Quart. J. Roy. Meteor. Soc.*, **123**, 467–489.

THIS PAGE INTENTIONALLY LEFT BLANK

INITIAL DISTRIBUTION LIST

1. Defense Technical Information Center
Ft. Belvoir, Virginia
2. Dudley Knox Library
Naval Postgraduate School
Monterey, California